Monthly Notices of the ROYAL ASTRONOMICAL SOCIETY

MNRAS **522,** 3831–3860 (2023) https://doi.org/10.1093/mnras/stad1205
Advance Access publication 2023 April 24

FIREbox: simulating galaxies at high dynamic range in a cosmological volume

Robert Feldmann [1★] Eliot Quataert [2] Claude-André Faucher-Giguère [3] Philip F. Hopkins [4] Onur Çatmabacak [1] Dušan Kereš [5†] Luigi Bassini [1] Mauro Bernardini [1] James S. Bullock [6] Elia Cenci [1] Jindra Gensior [1] Lichen Liang [7] Jorge Moreno [8] and Andrew Wetzel [9]

[1]*Institute for Computational Science, University of Zurich, Zurich, CH-8057, Switzerland*
[2]*Department of Astrophysical Sciences, Princeton University, Princeton, NJ 08544, USA*
[3]*CIERA and Department of Physics and Astronomy, Northwestern University, 1800 Sherman Ave, Evanston, IL 60201, USA*
[4]*California Institute of Technology, TAPIR, Mailcode 350-17, Pasadena, CA 91125, USA*
[5]*Center for Astrophysics and Space Sciences, University of California San Diego, San Diego, CA 92093, USA*
[6]*Department of Physics and Astronomy, University of California, Irvine, CA 92697, USA*
[7]*Canadian Institute for Theoretical Astrophysics, University of Toronto, Toronto, ON M5S 3H8, Canada*
[8]*Department of Physics and Astronomy, Pomona College, Claremont, CA 91711, USA*
[9]*Department of Physics and Astronomy, University of California, Davis, CA 95616, USA*

Accepted 2023 March 27. Received 2023 February 5; in original form 2022 May 23

ABSTRACT

We introduce a suite of cosmological volume simulations to study the evolution of galaxies as part of the *Feedback in Realistic Environments* project. FIREbox, the principal simulation of the present suite, provides a representative sample of galaxies ($\sim$1000 galaxies with $M_{\rm star} > 10^8\,M_\odot$ at $z = 0$) at a resolution ($\Delta x \sim 20\,{\rm pc}$, $m_{\rm b} \sim 6 \times 10^4\,M_\odot$) comparable to state-of-the-art galaxy zoom-in simulations. FIREbox captures the multiphase nature of the interstellar medium in a fully cosmological setting ($L = 22.1$ Mpc) thanks to its exceptionally high dynamic range ($\gtrsim 10^6$) and the inclusion of multichannel stellar feedback. Here, we focus on validating the simulation predictions by comparing to observational data. We find that star formation rates, gas masses, and metallicities of simulated galaxies with $M_{\rm star} < 10^{10.5-11}\,M_\odot$ broadly agree with observations. These galaxy scaling relations extend to low masses ($M_{\rm star} \sim 10^7\,M_\odot$) and follow a (broken) power-law relationship. Also reproduced are the evolution of the cosmic H_I density and the H_I column density distribution at $z \sim 0$–5. At low z , FIREbox predicts a peak in the stellar-mass–halo-mass relation but also a higher abundance of massive galaxies and a higher cosmic star formation rate density than observed, showing that stellar feedback alone is insufficient to reproduce the properties of massive galaxies at late times. Given its high resolution and sample size, FIREbox offers a baseline prediction of galaxy formation theory in a ΛCDM Universe while also highlighting modelling challenges to be addressed in next-generation galaxy simulations.

Key words: methods: numerical – galaxies: evolution – galaxies: ISM – galaxies: star formation – galaxies: stellar content.

1 INTRODUCTION

High-resolution galaxy surveys, e.g. with MUSE (Bacon et al. 2010; Emsellem et al. 2022), ALMA (Fomalont et al. 2015; Leroy et al. 2021a), and soon JWST (Gardner et al. 2006), ELT (Gilmozzi & Spyromilio 2007), and SKA (Dewdney et al. 2009) are promising to transform our understanding of how galaxies form and evolve. These observational advances will benefit from matched theoretical studies that quantify how the relevant (astro-)physical processes operating on sub-kpc scales shape the properties of galaxies and their interstellar medium (ISM; Somerville & Davé 2015; Naab & Ostriker 2017). This goal of galaxy theory is best approached with numerical simulations given the complexity, interconnectedness, and multiscale nature of the involved physics (e.g. Vogelsberger et al. 2020).

In the past, two main approaches have been employed to simulate the evolution of galaxies in a proper cosmological context. Cosmological volume simulations provide large samples of galaxies with a broad range in properties residing in a variety of cosmological environments (e.g. Dubois et al. 2014; Vogelsberger et al. 2014; Khandai et al. 2015; Schaye et al. 2015; Davé, Thompson & Hopkins 2016; Pillepich et al. 2018b; Davé et al. 2019). Here, physical processes are usually modelled in a simplified, parametrized manner and at a comparably low numerical resolution, e.g. the scale heights of disc galaxies ($\sim$100 pc) are typically unresolved. Furthermore, by modelling the relevant physics, especially the effects of stellar feedback (Mayer, Governato & Kaufmann 2008; Scannapieco et al. 2012; Crain et al. 2015) on a sub-grid scale, the predictions of the simulations are highly susceptible to model degeneracies. The alternative option are cosmological zoom-in simulations, which can

★ E-mail: robert.feldmann@uzh.ch
† Subsequent authors listed in alphabetical order.

© The Author(s) 2023.
Published by Oxford University Press on behalf of Royal Astronomical Society. This is an Open Access article distributed under the terms of the Creative Commons Attribution License (https://creativecommons.org/licenses/by/4.0/), which permits unrestricted reuse, distribution, and reproduction in any medium, provided the original work is properly cited.

Downloaded from https://academic.oup.com/mnras/article/522/3/3831/7140530 by Northwestern University School of Law user on 03 July 2023

reach higher numerical resolution, thus enabling them to model baryonic processes in the ISM on a more physical basis (e.g. Guedes et al. 2011; Ceverino et al. 2014; Hopkins et al. 2014; Agertz & Kravtsov 2015; Feldmann & Mayer 2015; Wang et al. 2015; Wetzel et al. 2016; Bellovary et al. 2019). Primary drawbacks of the zoom-in approach are the resulting much smaller sample sizes and/or higher computational costs.

Combining the strengths of both approaches offers the prospect of providing large samples of highly resolved, realistic galaxies that can then be compared with high-resolution observations to constrain galaxy theory. Recently, first efforts have been undertaken in this direction. These approaches differ in many aspects, e.g. in the implementation and calibration of the baryonic physics and in the numerical method of solving the underlying system of equations.

One general option is to run a large collection of high-resolution zoom-in simulations of individual galaxies (or small groups thereof) to increase samples sizes (e.g. Wang et al. 2015; Feldmann et al. 2016; Sawala et al. 2016; Grand et al. 2017; Hopkins et al. 2018; Kruijssen et al. 2019). While a powerful method, this approach also has a number of severe shortcomings, e.g. potential selection biases, limited large-scale correlations, and the contamination of the refinement region, that limit its applicability. Instead, the approach of the NEWHORIZON zoom-in simulation (Dubois et al. 2021) is to resolve an ensemble of galaxies in a large refined patch of $\sim (16\,\mathrm{cMpc})^3$. NEWHORIZON is run down to $z = 0.25$ with the adaptive mesh refinement (AMR) code RAMSES (Teyssier 2002) and makes use of a heavily modified version of the physical model of the HORIZON-AGN simulation (Dubois et al. 2014; Volonteri et al. 2016; Kaviraj et al. 2017). High numerical resolution and the modelling of low temperature cooling enable NEWHORIZON to partly resolve the multiphase nature of the ISM.

An alternative approach is to increase the resolution of cosmological volume simulations and improve the employed physical modelling. One advantage of using cosmological volumes over large zoom-ins is that the former can be analysed more straightforwardly given that the high-resolution region spans the entire cubic volume thus eliminating contamination artefacts.

The TNG50 simulation (Nelson et al. 2019b), run with the moving mesh code AREPO (Springel 2010), applies the IllustrisTNG physics model (Pillepich et al. 2018a) to a $(51.7\,\mathrm{cMpc})^3$ cosmological box, providing a sizable sample of galaxies at a mass resolution (baryonic particle mass $m_\mathrm{b} \sim 9 \times 10^4\,M_\odot$) similar to many zoom-ins. Originally calibrated for large volume simulations (Pillepich et al. 2018b; Nelson et al. 2019a), the physics model of TNG50 accounts for many baryonic processes in an idealized manner, e.g. the multiphase structure of the ISM is not directly resolved, star formation often takes place in low density gas ($n \geq 0.11\,\mathrm{cm}^{-3}$), and galactic outflows are put in by hand and temporarily decoupled from the hydrodynamics.

The ROMULUS25 simulation (Tremmel et al. 2017), run with the smoothed particle hydrodynamics (SPH) solver CHANGA (Menon et al. 2015), partly addresses some of these shortcomings by adopting a physics model used previously in a large number of high-resolution zoom-in simulations (e.g. Governato et al. 2007, 2010; Shen, Wadsley & Stinson 2010; Guedes et al. 2011) and by applying it, after re-tuning of some of the model parameters, to a $(25\,\mathrm{cMpc})^3$ cosmological box with a mass resolution of $m_\mathrm{b} \sim 2 \times 10^5\,M_\odot$. Specifically, ROMULUS25 includes lower temperature gas cooling and a more physical driving of galactic outflows via localized supernova explosions. However, in this model, the cooling time of gas heated by supernova feedback is artificially prolonged (Stinson et al. 2006). Furthermore, ROMULUS25 does not attempt to trace the dense, star-forming (usually molecular) component of the ISM and thus does not properly model the distribution of star formation and stellar feedback in galaxies.

While these recent simulations undoubtedly demonstrate significant progress, a potential concern is the existence of model degeneracies given that their underlying physical models both differ starkly and, in the case of TNG50 and ROMULUS25, are calibrated to observational data. One particularly promising, but challenging, path towards increasing the predictive power of galaxy simulations is to aim for a full accounting of well-understood physical processes with only a a minimal number of (ideally zero) tunable parameters. Implementing this research direction requires a sufficiently high dynamic range to model the relevant physical processes in a fully cosmological context. For instance, identifying the sites of star formation requires a resolution better than a few tens of pc while cosmological accretion and gravitational tides involve scales of tens of Mpc. Furthermore, the adopted physical model should be sufficiently realistic and comprehensive, e.g. the different ISM phases should be reproduced and stellar feedback modelled with as few assumptions as possible. Finally, a sufficiently large (and preferably unbiased) sample of highly resolved galaxies is needed to compare with observational data across cosmic history.

Fortunately, following this path has now become feasible given the increased computing capacity of supercomputers and algorithmic improvements in modelling galaxies numerically. Most critical, however, is the recent development of more accurate galaxy models that account for the relevant baryonic processes based on physical principles and that minimize the use of ad hoc parametrization (e.g. Hopkins, Quataert & Murray 2011; Agertz et al. 2013; Hopkins et al. 2014; Semenov, Kravtsov & Gnedin 2016; Kim & Ostriker 2017; Li, Bryan & Ostriker 2017; Hopkins et al. 2018; Marinacci et al. 2019; Kim et al. 2020; Hopkins et al. 2022). In particular, the detailed accounting of stellar feedback sources has shown to be paramount for producing galaxies in zoom-in simulations with more realistic properties, e.g. flatter rotation curves, lower stellar masses, and larger mass loading factors of galactic outflows (Guedes et al. 2011; Hopkins et al. 2014; Muratov et al. 2015; Applebaum et al. 2021).

As a first step on this challenging path, we have designed and run the FIREbox suite of cosmological volume simulations as part of the *Feedback in Realistic Environments* (FIRE) project[1] (Hopkins et al. 2014, 2018, 2022). The primary simulation (FIREbox) of this suite improves over current state of the art in two important aspects. First, FIREbox evolves a cosmological volume of $(22.1\,\mathrm{cMpc})^3$ down to $z = 0$ using a baryonic physics model without explicitly tuned subgrid parameters. This model (FIRE-2, Hopkins et al. 2018) has been used previously in cosmological zoom-in simulations (e.g. Anglés-Alcázar et al. 2017b; Chan et al. 2018; Ma et al. 2018, 2019; Pandya et al. 2021; Stern et al. 2021a), but it has not yet been applied to cosmological volumes. Secondly, FIREbox achieves a dynamic range of $\sim 10^6$, which is about an order of magnitude higher than TNG50, NEWHORIZON, and ROMULUS25, see section Section 2.4. The corresponding high spatial resolution ($\sim$20 pc) coupled with the more accurate physical modelling and representative sample size makes FIREbox a unique data set to explore the internal structure of galaxies across cosmic time. FIREbox is thus well suited to both studying the properties of typical galaxies, e.g. the link between galaxy size and dark matter (DM) halo properties (Rohr et al. 2022) or the atomic gas scale heights of Milky Way (MW) analogs (Gensior et al. 2022), to

[1] https://fire.northwestern.edu

Downloaded from https://academic.oup.com/mnras/article/522/3/3831/7140530 by Northwestern University School of Law user on 03 July 2023

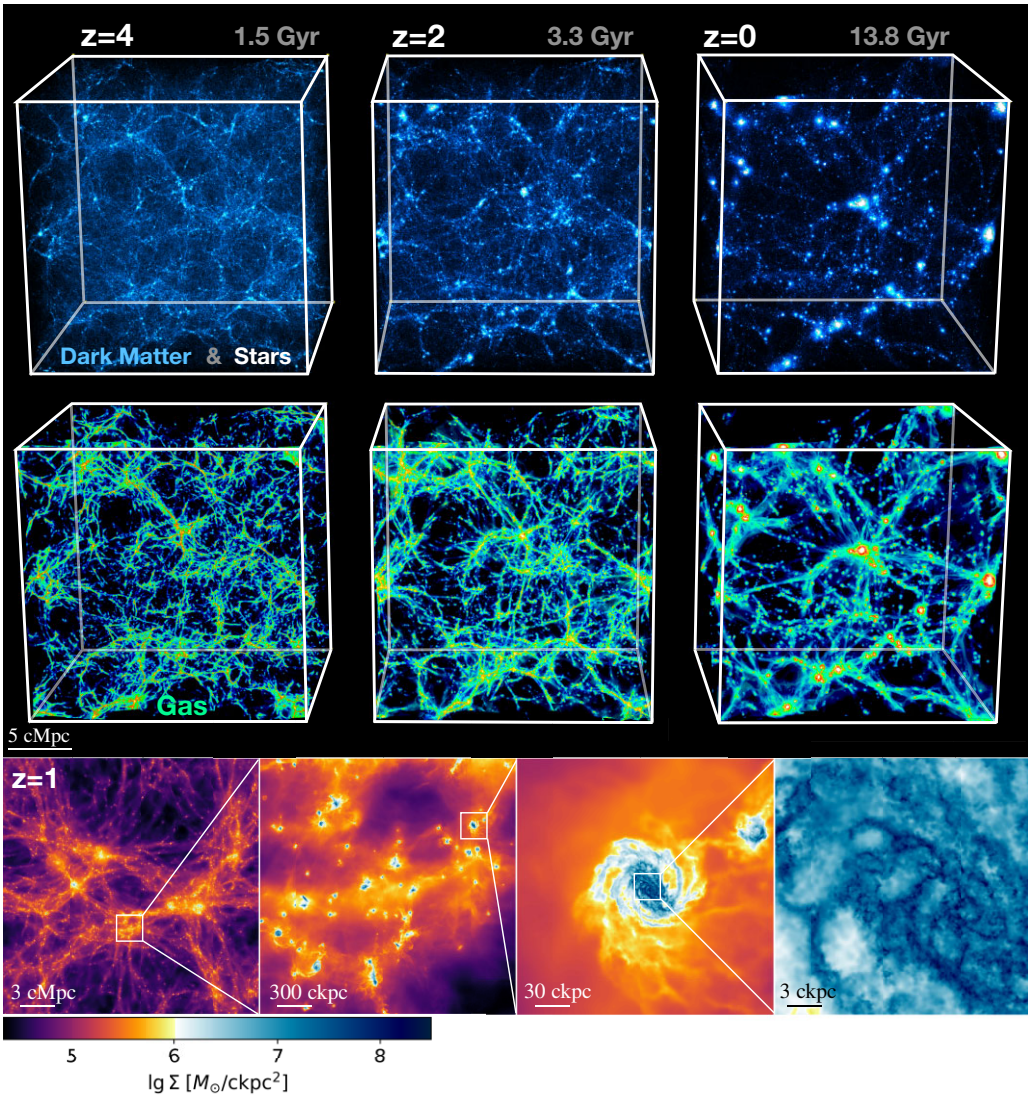

Figure 1. Visualization of the matter distribution in FIREbox. (Top row) 3D rendering of the DM (blue) and stars (white) in the simulation volume at $z = 4$, $z = 2$, and $z = 0$ (from left to right). DM forms a cosmic web of filamentary structures, overdensities, and voids, which evolves with redshift. Stars form at the centres of collapsed DM haloes. (Middle row) Visualization of the gas distribution that mirrors the cosmic network of DM. (Bottom row) Column density maps of the gas projected along the ∼22.1 cMpc depth of the box at $z = 1$. Starting from a view of the gas distribution on cosmological scales, the panels zoom into the ISM of one of many simulated galaxies, illustrating the high dynamic range of FIREbox.

exploring rare galaxy populations, such as low-mass, DM-deficient galaxies (Moreno et al. 2022) or starburst galaxies (Cenci et al. in preparation) and to quantifying the properties of the circumgalactic and intergalactic medium. Furthermore, it can be used as a training set for machine learning-based emulators, e.g. to predict the distribution of atomic hydrogen on large scales (Bernardini et al. 2022).

We highlight the high dynamic range of the simulation in the bottom row of Fig. 1. FIREbox can model both structures on cosmological scales as well as hydrodynamical processes within the dense ISM. Fig. 1 also visualizes the distribution of the various matter components in FIREbox. The top row shows the distribution of DM and star particles in the simulation volume at different redshifts, highlighting the formation and subsequent growth of large-scale structure. This cosmic web consists of overdense clusters of DM as well as filaments, sheets, and voids arranged in a complex pattern (e.g. Peebles 1980; Klypin & Shandarin 1983; Davis et al. 1985). Much of the DM in the cosmic web gravitationally collapses into virialized DM haloes, which then attract gas from their cosmic environments (middle row). Subsequently, stars and galaxies form at the halo centres (White & Rees 1978).

A particular feature of the physics-based approach that we follow in this paper is that we intentionally exclude feedback from active galactic nuclei (AGNs) given the large uncertainties involved in its physical modelling. The FIREbox simulation should thus be understood as providing baseline predictions in the absence of AGN feedback. A comparison between simulation predictions and observations can then be used to make inferences about the role of this feedback channel in galaxy theory. For instance, the low fraction of massive, quiescent galaxies in FIREbox, compared with observations, supports the notion that AGN feedback plays indeed a critical role in galaxy quenching (Springel, Di Matteo & Hernquist 2005; Croton et al. 2006; Hopkins et al. 2006; Cattaneo et al. 2009). In contrast, star-forming galaxies in FIREbox follow many of their observed global scaling relations, indicating that AGN feedback does

Downloaded from https://academic.oup.com/mnras/article/522/3/3831/7140530 by Northwestern University School of Law user on 03 July 2023

not strongly affect the latter. We note that understanding the role and impact of this feedback channel is a critical open challenge for galaxy formation, and there is increasing evidence that AGN feedback plays an important role not only in massive galaxies (e.g. Springel et al. 2005; Dubois et al. 2013; Tremmel et al. 2019) but also in galaxies of lower mass (e.g. Beckmann et al. 2017; Dashyan et al. 2018; Koudmani, Henden & Sijacki 2021). We leave a detailed and more direct analysis of the role of AGN feedback to future work (see Wellons et al. 2023 for a first exploration of the effects of AGN feedback in a large suite of FIRE-2 zoom-in simulations).

The outline of this paper is as follows. In Section 2, we introduce our suite of cosmological volume simulations, including its set-up, the numerical modelling, and various aspects of our post-processing analysis. Subsequently, we focus on the primary simulation (FIREbox). We discuss basic properties of FIREbox galaxies, including various galaxy-scaling relations, in Section 3. Subsequently, in Section 4, we analyse the evolution of the cosmic star formation rate (SFR) density, the cosmic gas density, and the column density distribution function (CDDF) of atomic and molecular hydrogen. We summarize our findings in Section 5.

2 METHODOLOGY

2.1 Initial conditions

In contrast to previous FIRE simulations, the FIREbox suite does not use the zoom-in approach to study galaxy evolution but rather it simulates gas, stars, and DM in a cubic cosmological volume of $V = (15\,\mathrm{cMpc}\,h^{-1})^3 \sim (22.1\,\mathrm{cMpc})^3$ with periodic boundary conditions. Initial conditions for all simulations in the FIREbox suite were created with the MUlti-Scale Initial Conditions tool (MUSIC;[2] Hahn & Abel 2011). Cosmological parameters were taken from Planck-2015 cosmic microwave background measurements combined with baryon acoustic oscillation data as well as supernova and cepheid observations (see Planck Collaboration 2015); $\Omega_\mathrm{m} = 0.3089$, $\Omega_\Lambda = 1 - \Omega_\mathrm{m} = 0.6911$, $\Omega_\mathrm{b} = 0.0486$, $h = 0.6774$, $\sigma_8 = 0.8159$, $n_\mathrm{s} = 0.9667$. Transfer functions for baryons, cold DM, and total matter were calculated for the same cosmology via the Code for Anisotropies in the Microwave Background (CAMB;[3] Lewis, Challinor & Lasenby 2000) with $z_\mathrm{init} = 120$ as starting redshift.

The specific initial conditions for the FIREbox suite were chosen by first running a suite of 27 low-resolution (128^3) collision-less N-body simulations of the chosen volume. Subsequently, one of the boxes was selected and corresponding higher-resolution initial conditions with and without baryonic matter were created. The objective of this manual selection was to obtain a realization of the halo mass function (HMF) that is close to average for most redshifts. In addition, the selection was weighted towards boxes that do not contain a halo of exceptionally high mass at $z = 0$ to avoid the associated higher computational cost and to reduce cosmic variance.

2.2 Gravity and baryonic physics

The selected cosmological volume was evolved down to $z = 0$ both with and without baryonic physics with the combined hydrodynamics and gravity solver GIZMO[4] (Hopkins 2015). GIZMO calculates gravitational forces ,between particles with a heavily modified version of the tree gravity solver of GADGET-3 (Springel 2005; Springel et al. 2008) and it models hydrodynamical processes with the meshless-finite-mass (MFM) method (Hopkins 2015).

Baryonic processes, such as gas cooling and heating, star formation, and stellar feedback, are accounted for via the FIRE-2 physics model (Hopkins et al. 2018). Supermassive black holes and AGN feedback are not included, see below. We now briefly review the most important details of the FIRE-2 model.

The temperature of the gas is calculated over the $T \sim 10$–^{10} K range by modelling free–free, Compton, photoelectric, photoionization, metal-line, molecular, fine-structure, dust collisional, and cosmic ray heating (but not cosmic ray transport) and/or cooling processes both from local sources and from a redshift-dependent, spatially uniform ultraviolet background (Faucher-Giguère et al. 2009). Ionization states and cooling rates of Hydrogen and Helium are calculated following Katz, Weinberg & Hernquist (1996) with the fitting functions by Verner & Ferland (1996). The simulations follows 15 species (H, He, C, N, O, Ne, Mg, Si, S, Ca, Fe, and four tracker species for r-process elements) and includes sub-grid metal diffusion from unresolved turbulence (Su et al. 2017; Escala et al. 2018). Each gas particle starts with a metallicity of 2×10^{-6}, i.e. about 10^{-4} solar. Metal cooling uses the rates by Wiersma, Schaye & Smith (2009a) for high temperature gas ($> 10^4$ K) and pre-tabulated rates calculated with CLOUDY (Ferland et al. 1998) at low temperatures ($\leq 10^4$ K). Self-shielding from both local sources and the cosmic UV background is accounted for via a Sobolev-length approximation based on the density gradient calibrated on radiative transfer experiments (Gnedin, Tassis & Kravtsov 2009; Faucher-Giguère et al. 2010; Rahmati et al. 2013).

Star formation takes place in self-gravitating, dense ($n \geq 300\,\mathrm{cm}^{-3}$ for FIREbox, see Table 1), Jeans unstable, molecular (self-shielding) gas with a 100 per cent efficiency per local free-fall time. The molecular-to-neutral gas ratio is calculated via an analytic model (Krumholz, McKee & Tumlinson 2008, 2009; McKee & Krumholz 2010), assuming photodissociation and two-phase equilibrium. This model requires as inputs the metallicity Z and the dust optical depth for Lyman-Werner photons τ, see Krumholz & Gnedin (2011). The metallicity is known for each particle and the dust optical depth is estimated via a local Sobolev-length approximation. Specifically, $\tau = 434.8\,\mathrm{cm}^2\,\mathrm{g}^{-1}\,\Sigma_\mathrm{gas}[0.1 + Z/0.02]$, where Z is the metallicity and $\Sigma_\mathrm{gas} = \rho[d + \rho/|\vec{\nabla}\rho|]$ is the gas mass surface density. Furthermore, d is the inter-particle separation, which is closely related to the kernel length of the given gas particle (Hopkins 2015; Hopkins et al. 2018).

Stellar feedback includes energy, momentum, mass, and metal injections from supernovae (type II and type Ia) and stellar winds (OB and AGB stars). The ejecta energy per supernova is 10^{51} erg. Most feedback quantities are taken from tabulated stellar population models (STARBURST99; Leitherer et al. 1999) for a Kroupa (2001) initial SMF (IMF). In addition, SN Ia rates are taken from Mannucci, Della Valle & Panagia (2006) and yields from Iwamoto et al. (1999). SN II yields are from Nomoto et al. (2006) and yields for OB/AGB stars follow Wiersma et al. (2009b). Radiative feedback in the form of photoionization and photoelectric heating, as well as radiation pressure, is also included. Radiative transfer effects are accounted for in the Locally Extincted Background Radiation in Optically thin Networks approximation (Hopkins, Quataert & Murray 2012; Hopkins et al. 2014, 2018; Hopkins & Grudić 2019).

None of the current FIREbox runs include a model for AGN feedback. We plan to add cosmic ray physics (Chan et al. 2019; Hopkins et al. 2020) and AGN feedback (Wellons et al. 2023) in future FIREbox simulations to explicitly study the differential impact of these additional physical processes.

[2] www-n.oca.eu/ohahn/MUSIC
[3] camb.info
[4] http://www.tapir.caltech.edu/~phopkins/Site/GIZMO.html

Downloaded from https://academic.oup.com/mnras/article/522/3/3831/7140530 by Northwestern University School of Law user on 03 July 2023

Table 1. The FIREbox simulation suite. A systematic name and a short description for each run are provided in the first two columns. Columns three to six list the number of particles at the start of each simulation, the redshift reached by each simulation, the box size, and density threshold for star formation. The final six columns provide the masses of baryonic (gas and star) particles, the masses of DM (DM) particles, the inter-particle spacing of gas particles at the star formation threshold, the minimum gravitational softening length of gas particles, and the gravitational softening lengths of star and DM particles. For comparison with the literature, the force resolution is stated in equivalent Plummer softening lengths. The corresponding spline softening lengths are larger by a factor of ∼1.4. For every hydrodynamical simulation, there is a corresponding collisionless *N*-body simulation with particle masses $m = m_{\rm b} + m_{\rm DM}$ and gravitational softening lengths $\epsilon = \epsilon_{\rm DM}$. This suite is complemented with a higher resolution collisionless simulation FB2048-DM, see Lazar et al. (2021). The main focus of the present work is the FB1024 hydrodynamical simulation (FIREbox) listed in the top row.

Name	Comment	N	$z_{\rm final}$	L (cMpc)	$n_{\rm SF}$ (cm^{-3})	$m_{\rm b}$ ($10^4\,M_\odot$)	$m_{\rm DM}$ ($10^5\,M_\odot$)	$d_{\rm gas,\,SF}$ (pc)	$\epsilon_{\rm gas,\,min}$ (pc)	$\epsilon_{\rm star}$ (pc)	$\epsilon_{\rm DM}$ (pc)
FB1024	**FIREbox**	**2×1024^3**	**0**	**22.1**	**300**	**6.26**	**3.35**	**20.4**	**1.5**	**12**	**80**
FB512	lower res. re-run	2×512^3	0	22.1	100	50.1	26.8	58.8	4	32	160
FB256	lower res. re-run	2×256^3	0	22.1	10	401	215	253	16	128	320
FB1024-DM	FIREbox$^{\rm DM}$	1024^3	0	22.1	–	–	3.98	–	–	–	80
FB512-DM	lower res. *N*-body	512^3	0	22.1	–	–	31.8	–	–	–	160
FB256-DM	lower res. *N*-body	256^3	0	22.1	–	–	255	–	–	–	320

2.3 Numerical resolution

In all runs, gravity is softened with a cubic spline kernel. The force resolution of gas particles is adaptive and set to the gas inter-particle spacing $h = (m_{\rm b}/\rho_{\rm b})^{1/3}$ subject to a lower limit ($\epsilon_{\rm gas,\,min}$). This lower limit is chosen such that the highest gravitationally resolved gas density $n^{\rm max} = m_{\rm b}/(\epsilon_{\rm gas,\,min})^3/m_{\rm H}$ exceeds the star formation threshold density $n_{\rm SF}$ by a factor of ∼1000, see Hopkins et al. (2018). The force softenings of star and DM (DM) particles are non-adaptive. The softening length of star particles was chosen to be similar to the softening length of gas particles at the star formation threshold. Newly formed star particles have thus a similar softening length as the gas particles that spawned them. The Plummer equivalent softening length of DM particles is set to $\sim 20\,{\rm pc}\,(m_{\rm DM}/5000 M_\odot)^{1/3}$ to avoid oversoftening of the central DM halo profile while also minimizing *N*-body relaxation due to particle scattering (Hopkins et al. 2018). The value of $\epsilon_{\rm gas,\,min}$ and the softening lengths of star and DM particles are kept fixed in physical (comoving) coordinates at $z \leq 9$ ($z \geq 9$).

FIREbox (FB1024), the primary simulation discussed in this paper, contains 1024^3 gas and 1024^3 DM particles at the starting redshift with masses $m_{\rm b} = 6.3 \times 10^4\,M_\odot$ and $m_{\rm DM} = 3.3 \times 10^5\,M_\odot$, respectively. A new star particle inherits the mass of the gas particle from which it was created. However, as a result of supernova explosions and stellar winds, star particles lower their mass over time to $\sim 0.7 m_{\rm b}$. The mass resolution in FIREbox is $\approx 8\times$ lower than FIRE zooms of MW analogs (e.g. Wetzel et al. 2016; Hopkins et al. 2018). The minimum gas softening length (Plummer equivalent) is $\epsilon_{\rm gas,\,min} = 1.5$ pc. A more representative measure of the spatial resolution of hydrodynamical processes in the ISM is the inter-particle spacing of gas particles eligible for star formation ($\lesssim$20 pc in FIREbox). Star particles (DM particles) have a Plummer equivalent softening length of $\epsilon_{\rm star} = 12$ pc ($\epsilon_{\rm DM} = 80$ pc). Mass and force resolution of the FB512 (FB256) runs are correspondingly lower, see Table 1. The completion of FIREbox required approximately 5 million compute core hours and a wall-clock time of about 3 months.

2.4 Comparison with state-of-the-art galaxy formation simulations

Fig. 2 compares the hydrodynamic mass and spatial resolution of FIREbox with a compilation of cosmological galaxy formation simulations of intermediate-to-high mass galaxies reaching $z < 2$. Zoom-in simulations that specifically target very low-mass galaxies (e.g. Fitts et al. 2017; Revaz & Jablonka 2018; Wheeler et al. 2019; Munshi et al. 2019) can reach a higher numerical resolution and are not included in this comparison. While not an exhaustive list, the compilation includes the state of the art in galaxy formation simulations, and it covers a range of hydrodynamics solvers, such as AMR, SPH, moving mesh hydrodynamics, and mesh-less hydrodynamics as well as both zoom-in runs and large-volume simulations. Specifically, the compilation includes cosmological volume simulations from the Illustris (Vogelsberger et al. 2014; Genel et al. 2014), IllustrisTNG (Pillepich et al. 2018b; Nelson et al. 2019b), EAGLE (Schaye et al. 2015), MUFASA (Davé et al. 2016), SIMBA (Davé et al. 2019), MassiveBlack-II (Khandai et al. 2015), Romulus (Tremmel et al. 2017), and Horizon-AGN (Dubois et al. 2014) projects, representative zoom-in simulations from the FIRE project (Hopkins et al. 2014, 2018), such as Latte (Wetzel et al. 2016) and MassiveFIRE (Feldmann et al. 2016, 2017; Anglés-Alcázar et al. 2017b), and zoom-in simulations by Agertz & Kravtsov (2015) as well as from the Apostle (Sawala et al. 2016), Argo (Feldmann & Mayer 2015), Auriga (Grand et al. 2017, 2021), DC Justice League (Bellovary et al. 2019; Applebaum et al. 2021), Eris (Guedes et al. 2011), Mochima (Nuñez-Castiñeyra et al. 2021), NewHorizon (Dubois et al. 2021), NIHAO (Wang et al. 2015), VELA (Ceverino et al. 2014), and Vintergatan (Agertz et al. 2021) projects.

Given the intrinsic ambiguity in defining mass and spatial resolution across such a variety of models, we adopt the following operational definitions. For particle-based hydrodynamics codes, the mass resolution is defined as the typical gas particle mass in the simulation. Adopting a more physics-based definition, e.g. using the minimal resolved Jeans mass, would favour even more simulations, such as FIREbox, which directly model the multiphase ISM (shown by filled symbols) compared with simulations that do not (empty symbols), i.e. those that prevent gas from cooling to low temperatures ($T < 1000$ K) and/or those that model the ISM with an effective equation of state resulting in highly pressurized and comparably smooth gas discs. The spatial resolution is set to the larger of the gas inter-particle spacing $d_{\rm SF}$ at the star formation threshold, $d_{\rm SF} = 74\,{\rm pc}(m_{\rm b,4}/n_{\rm SF,0})^{1/3}$ with $m_{\rm b,4} = m_{\rm b}/(10^4\,M_\odot)$ and $n_{\rm SF,\,0} = n_{\rm SF}/{\rm cm}^{-3}$, and the minimum spline gravitational softening length of gas particles. While dynamical processes may be resolved on scales smaller than $d_{\rm SF}$, those scales are affected by the physics of sink particle formation. For grid-based simulations with a quasi-Lagrangian refinement scheme, we adopt $m_{\rm b} = \Omega_{\rm b}/(\Omega_{\rm m} - \Omega_{\rm b}) m_{\rm DM}$ as hydrodynamic mass resolution, while the spatial resolution is

Downloaded from https://academic.oup.com/mnras/article/522/3/3831/7140530 by Northwestern University School of Law user on 03 July 2023

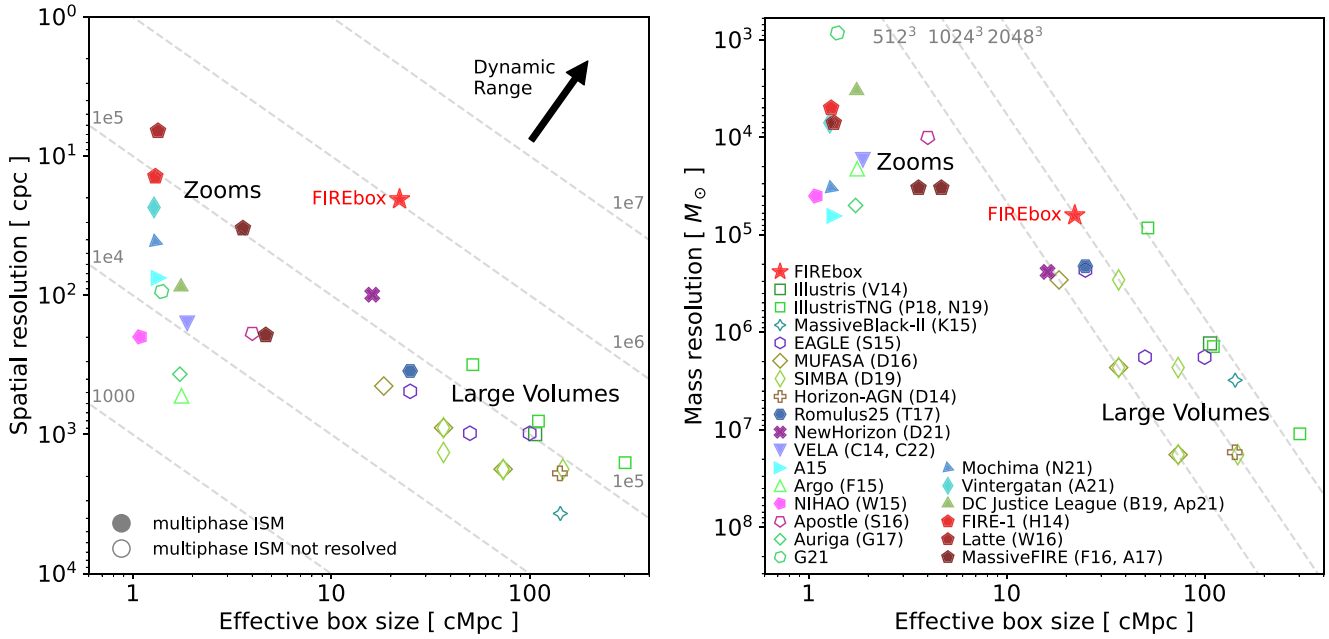

Figure 2. Hydrodynamic resolution and box size of FIREbox compared with a representative selection of contemporary cosmological galaxy formation simulations from Vogelsberger et al. (2014; V14), Pillepich et al. (2018b; P18), Nelson et al. (2019b; N19), Khandai et al. (2015; K15), Schaye et al. (2015; S15), Davé et al. (2016, 2019; D16, D19), Dubois et al. (2014; D14), Tremmel et al. (2017; T17), Dubois et al. (2021; D21), Ceverino et al. (2014, 2023; C14, C22), Agertz & Kravtsov (2015), Agertz et al. (2021; A17, A21), Feldmann & Mayer (2015; F15), Wang et al. (2015; W15), Sawala et al. (2016; S16), Grand et al. (2017, 2021; G17, G21), Nuñez-Castiñeyra et al. (2021; N21), Bellovary et al. (2019; B19), Applebaum et al. (2021; Ap21), Hopkins et al. (2014; H14), Wetzel et al. (2016; W16), Feldmann et al. (2016; F16), and Anglés-Alcázar et al. (2017b; A17). In each panel, FIREbox is shown by a red star. (Left) Spatial resolution versus effective box size. The former refers to the *typical* resolution in the star-forming gas of a given simulation. Specifically, for particle-based hydrodynamics codes, the spatial resolution is defined as the larger of the minimum gravitational softening length of gas particles and the inter-particle distance at the star formation threshold density. For grid-based codes with a Lagrangian refinement strategy, the spatial resolution is defined similarly based on the minimum cell size and the gas density at the star formation density threshold (see text). The effective box size equals the comoving box length for cosmological volume simulations. For zoom-in simulations, the effective box size is set to five times the comoving virial radius of the largest halo in the zoom-in region at the final snapshot. Not shown are zoom-in simulations that do not resolve at least one MW mass halo or that have a baryonic mass resolution worse than 10^5 $M_\odot$. Diagonal dashed lines show the resolved dynamic range of a simulation, i.e. the ratio between the effective box size and the spatial resolution (both in comoving units). FIREbox is the first cosmological galaxy formation simulation run to $z = 0$ with a dynamic range of more than one million. (Right) Baryonic mass resolution versus effective box size. Diagonal dashed lines show the approximate number of hydrodynamic resolution elements in the simulation volume. In each panel, filled (empty) symbols indicate simulations with (without) a resolved multiphase ISM, see text. FIREbox is able to capture the multiphase structure of gas in and around galaxies in a fully cosmological context and across cosmic history.

defined as the larger of $d_{\rm SF}$ and the minimum cell size. In each case, we calculate the spatial resolution in comoving pc at the redshift of the final simulation snapshot. The spatial resolution can substantially exceed the minimum cell size or the minimum gravitational softening length of gas particles, e.g. ∼20 versus 1.5 pc for FIREbox, ∼100 versus 34 pc for NewHorizon, and ∼300 versus 74 pc for TNG-50.

The figure also shows the effective box size of the simulations. The effective box size equals the comoving box length for cosmological volume simulations. For zoom-ins, it is set to five times the comoving virial radius of the most massive halo in the highest resolution region at the final simulation redshift to approximately reproduce the typical extent of the zoom-in region uncontaminated by low-resolution DM particles. Only the largest simulation is considered when calculating the effective box size for simulations suites consisting of multiple independent runs of similar resolution, such as Apostle, Auriga, or MassiveFIRE. Zoom-in simulations that do not resolve at least one MW mass halo or that have a baryonic mass resolution worse than 10^5 $M_\odot$ are not included in the figure. The ratio between the effective box size and the spatial resolution of a simulation defines its dynamic range.

FIREbox opens a new frontier in studying the evolution of galaxies with hydrodynamical simulations given its unique combination of high numerical resolution (comparable to state-of-the-art zoom-ins) and accurate physical modelling in a cosmological volume of $(22.1\,{\rm cMpc})^3$. Specifically, FIREbox is able to both directly resolve the thermodynamic state of the ISM (by enabling self-consistent cooling down to ∼10–20 K) and to accurately account for multiple stellar feedback channels tied to stellar population synthesis models (see Section 2.2). The underlying FIRE-2 physics model has been employed previously in zoom-in simulations to study the multiphase nature of the ISM, e.g. the overall properties of massive giant molecular clouds (Benincasa et al. 2020; Guszejnov et al. 2020) and the vertical pressure profiles and scale heights of galactic discs (Gurvich et al. 2020). With FIREbox, we can study galaxies and their ISM with larger, representative samples from a contiguous cosmological volume, enabling a proper statistical analysis and a study of cosmological environments. While the dynamic range of FIREbox ($\gtrsim 10^6$) already exceeds significantly those of contemporary galaxy formation simulations, higher-resolution follow-up simulations combined with dedicated zoom-ins promise to further extend this frontier towards larger samples of better resolved galaxies.

Downloaded from https://academic.oup.com/mnras/article/522/3/3831/7140530 by Northwestern University School of Law user on 03 July 2023

2.5 Simulation output

The properties of gas, star, and DM particles are saved as Gadget HDF5 files in (semi)regular intervals for subsequent analysis. All FIREbox runs, except FB2048-DM, use 1201 save-points that are approximately equally spread in cosmic time between $z_{\rm init} = 120$ and $z_{\rm final} = 0$, resulting in a close to 11 Myr average save-point intervals. For FB2048-DM, fewer save-points are used at $z < 2$ to mitigate its high storage footprint. Furthermore, three out of every four save-points are stored at reduced resolution ('snipshots') to reduce the overall storage cost of the simulation suite, see below. In addition, all save-points (both snipshots and regular snapshots) are stored in gzip compressed format.

A save-point is stored either as a level 0 snapshot, a level 1 snapshot, or a level 2 'snipshot'. Level 0 snapshots are compressed in a loss-less manner but are otherwise identical to the original HDF5 output files. The compression can reduce the file size by up to a factor of 2. Level 1 snapshots are identical to level 0 snapshots except that the abundances of individual elements (but not the total metallicity) are stored at reduced precision (1 byte) in hydrodynamical simulations. Level 2 snipshots differ significantly from snapshots. Densities, electron abundances, neutral hydrogen abundances, helium abundances, total metallicities, internal energies, softening lengths, and velocities of gas particles are stored at reduced resolution (typically as a half-precision float and after a log transform for non-negative fields). Additionally, the individual abundances of elements heavier than Helium are dropped. Gas particle masses and coordinates are kept at full resolution, however. In addition, star particles keep the same information as for level 1 snapshots. DM particles are downsampled randomly by a factor 8 with the help of a scrambled Xorshift generator (Marsaglia 2003; Vigna 2016) such that the same particles are removed (or kept) in all snipshots. The storage footprint of a level 0 snapshot (level 1 snapshot, level 2 snipshot) of FIREbox at $z \sim 0$ is 207 GB (97 GB, 42 GB).

2.6 Halo and galaxy catalogs

We identify DM haloes and catalog their various properties, including halo positions, masses, radii, and whether or not a given halo is a sub-halo or a main halo, with the help of the AMIGA Halo finder (AHF; Gill, Knebe & Gibson 2004; Knollmann & Knebe 2009). We include only haloes with at least 100 particles in the subsequent analysis. Halo masses ($M_{\rm halo}$) and radii ($R_{\rm vir}$) are calculated based on the virial overdensity definition (Bryan & Norman 1998) and include baryonic matter and halo sub-structures. Growth histories for individual haloes are constructed with the AHF MergerTree tool by linking haloes in subsequent snapshots via the identification numbers of their DM particles.

Intuitively, 'sub-haloes' are DM haloes that reside within other DM haloes. More quantitatively, AHF identifies a DM halo of radius R as a 'sub-halo' of another, more massive DM halo of radius R' if the distance between the two haloes is less than $R' + 0.5\,R$. Haloes that are not sub-haloes are 'main haloes'. Galaxies in sub-haloes are called satellite galaxies, while the primary galaxy of a main halo is called its central galaxy.

With the help of the AHF particle files, we identify both the direct host halo (which can be a sub-halo or a main halo) for each particle as well as the main halo containing the particle. Subsequently, we use this information to calculate a variety of particle-based properties, e.g. stellar masses, SFRs, and gas masses in various 3D spherical apertures, and store them in HDF5 files for subsequent analysis. Halo properties are measured within a sphere of radius $R_{\rm vir}$, while a smaller radius $R_{\rm g}$ (see below) is used to measure galaxy properties. For sub-haloes, $R_{\rm vir}$, as reported by AHF and used below, refers to the smaller of the virial and the tidal radius.

The total radius $R_{\rm g}$ and the stellar half mass radius $R_{\rm half}$ of galaxies are defined using two different approaches based on the cumulative spherical stellar mass profile $M_{\rm star}(< R)$ and the virial radius. The first approach follows Hopkins et al. (2018). Starting from an initial choice for $R_{\rm g}$ of 0.15 $R_{\rm vir}$, the half mass radius is computed as $M_{\rm star}(< R_{\rm half}) = 0.5 M_{\rm star}(< R_{\rm g})$, and the total radius is updated as $R_{\rm g} = 3 \times R_{\rm half}$. The latter steps are repeated until the relative change in $R_{\rm g}$ between one iteration and the next is less than 10^{-5}. The second approach sets $R_{\rm g} = 0.1\,R_{\rm vir}$ and subsequently calculates $R_{\rm half}$ from the stellar mass profile within $R_{\rm g}$. Unless stated otherwise, stellar masses, SFRs, and other properties of galaxies refer to integrated properties within $R_{\rm g}$ computed as in the first method.

2.7 Gas fractions and temperatures

The mass $m_{\rm gas}$ of each gas particle can be divided into the mass of ionized ($m_{\rm H_{II}}$), atomic ($m_{\rm H_I}$), and molecular hydrogen ($m_{\rm H_2}$) as well as the mass in Helium and in the various metals. The total hydrogen mass of a gas particle is $m_{\rm H} = m_{\rm H_I} + m_{\rm H_2} + m_{\rm H_{II}} = X m_{\rm gas}$, where the hydrogen mass fraction X can vary from particle to particle. The neutral hydrogen fraction $f_{\rm H_I+H_2} = (m_{\rm H_I} + m_{\rm H_2})/m_{\rm H}$ of each particle is calculated during the run-time of the simulation as described in Hopkins et al. (2018) and is provided in the simulation snapshots. At the level of individual gas particles, $f_{\rm H_I+H_2}$ is also the neutral gas fraction $(m_{\rm atm} + m_{\rm mol})/m_{\rm gas}$ provided we define atomic and molecular gas masses of particles as $m_{\rm atm} = m_{\rm H_I}/X$ and $m_{\rm mol} = m_{\rm H_2}/X$. The molecular gas fraction $f_{\rm H_2} = m_{\rm H_2}/m_{\rm H} = m_{\rm mol}/m_{\rm gas}$ of each particle, which is also calculated at run-time, is not part of the simulation output, however. We thus recalculate it based on the snapshot data. Specifically, we first calculate the molecular-to-neutral gas ratio $f_{\rm H_2}/f_{\rm H_I+H_2}$ based on its dust optical depth and metallicity following the same approach (Krumholz & Gnedin 2011) as for the run-time calculation described above, see Section 2.2. Given the various assumptions entering this approach, the resulting estimate of the molecular-to-neutral gas ratio should be understood as an approximation that may be highly inaccurate under certain conditions, e.g. at metallicities below $0.01\,Z_\odot$. We then convert the molecular-to-neutral gas ratio to the molecular gas fraction by multiplying the former with $f_{\rm H_I+H_2}$. The atomic gas fraction of a particle $f_{\rm H_I} = m_{\rm H_I}/m_{\rm H} = m_{\rm atm}/m_{\rm gas}$ is calculated as $f_{\rm H_I+H_2} - f_{\rm H_2}$.

Gas temperatures are re-calculated from the internal energy per unit mass ϵ, electron abundance $f_{\rm e} = n_{\rm e}/n_{\rm H}$, Helium abundance Y, metallicity Z, all of which are provided in the simulation output and from the molecular gas fraction $f_{\rm H_2}$ calculated as described above. The gas temperature is given as $T = \epsilon(\gamma - 1)\mu/k_{\rm B}$ with the mean molecular weight $\mu = m_{\rm H}/[X(1 - 0.5 f_{\rm H_2}) + Y/4 + f_{\rm e} X + Z/16]$ and with $X = 1 - Y - Z$. FIREbox employs a floor in specific internal energy that amounts to a temperature floor of $\sim$10 K in atomic gas and $\sim$18 K in molecular gas.

3 PROPERTIES OF FIREBOX GALAXIES

In this section, we analyse basic properties of FIREbox galaxies. Our main focus lies in comparing our simulation predictions to available observational data. We will demonstrate that many basic galaxy scaling relations predicted by the simulation, e.g. the relations between galaxy stellar mass and their SFRs, gas content, and metallicity, agree reasonably well with observations. Other properties, such as the stellar mass functions (SMF) and the galaxy stellar mass–halo mass

Downloaded from https://academic.oup.com/mnras/article/522/3/3831/7140530 by Northwestern University School of Law user on 03 July 2023

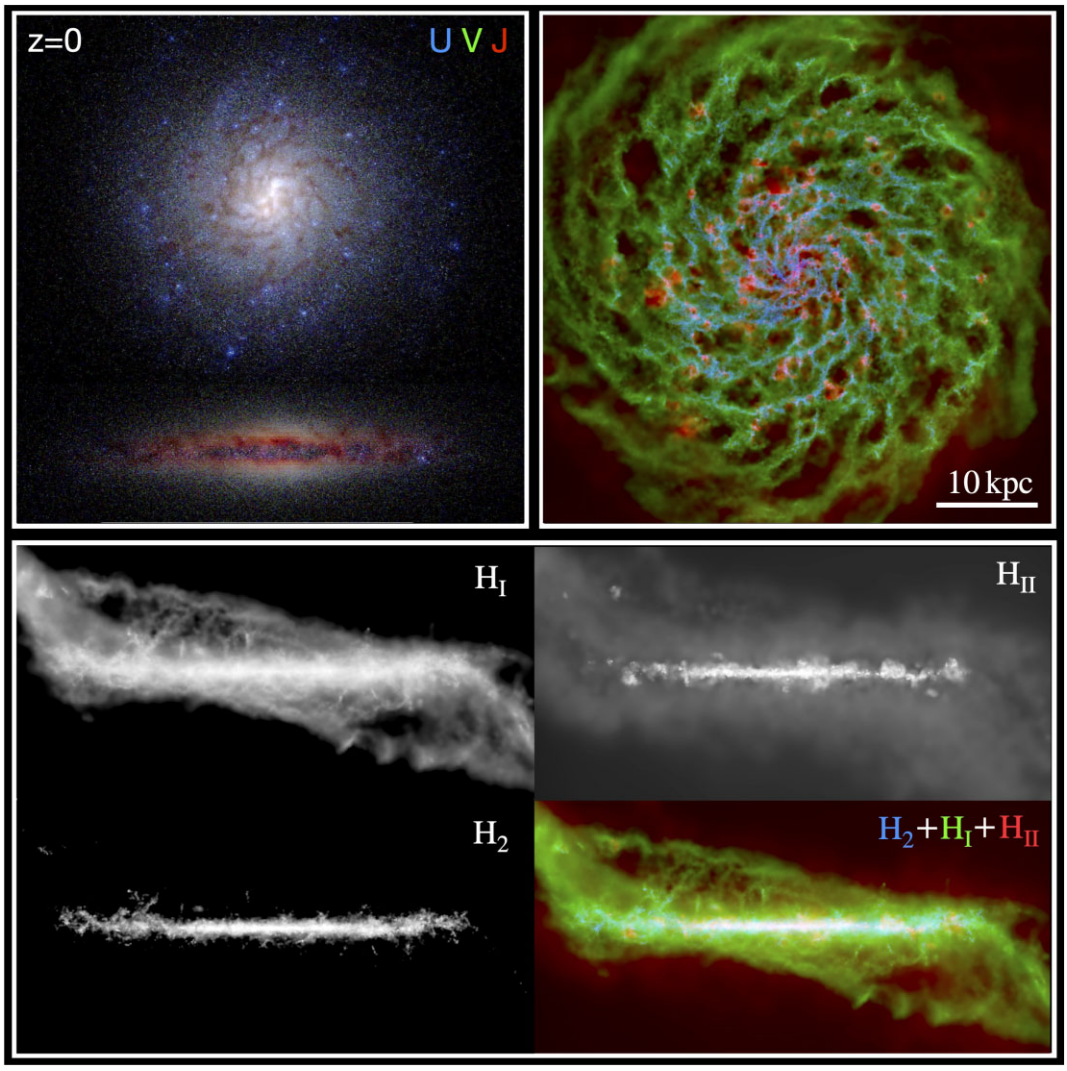

Figure 3. Visualization of the multiphase structure of baryons in a MW-like galaxy at $z = 0$ in FIREbox. (Top left) Colour composite image in U (blue), V (green), and J (red) broadbands, created with the radiative transfer code SKIRT (Baes et al. 2011; Camps & Baes 2015), showing the stellar and dust components of the depicted galaxy in a face-on and edge-on view. This galaxy has an overall discy morphology. (Top right) Face-on, colour composite image of the galaxy's molecular (H_2, blue), atomic (H_I, green), and ionized (H_{II}, red) hydrogen content. (Bottom) Edge-on view of the atomic, ionized, molecular, and combined hydrogen content (see legend). The neutral ISM resides in an extended but thin gas disc with a complex internal structure (see text). The neutral ISM is embedded in a thick but comparably smooth, disc of ionized gas. Ionized gas is also present in regions of various sizes within the plane of the ISM disc. The locations of these ionized regions often coincide with those of young stellar clusters shown in blue in the UVJ image. The H_I and H_{II} discs are strongly warped at large radii. All images have the same physical scale (50 kpc from left to right), see legend, and show quantities on a logarithmic stretch. The centre of the galaxy is shifted vertically in the top-left panel. Many of the shown features, e.g. some of the H_2 spiral arms and H_{II} bubbles, are less than 100 pc across.

relation (SHMR) are not reproduced as well. Here, the predictions of FIREbox are more in line with recent stellar mass estimates based on non-parametric panchromatic spectral energy distribution (SED) modelling.

Throughout this section, a Chabrier (2003) IMF is adopted for all observational data. Specifically, we lower stellar masses and SFRs by 0.25 dex when converting from Salpeter (1955) IMF to Chabrier (2003) IMF (see e.g. Lee et al. 2006; Gallazzi et al. 2008; Herrmann et al. 2016). We ignore the small shift between a Chabrier (2003) IMF and the Kroupa (2001) IMF adopted by FIREbox.

3.1 The multiphase interstellar medium

One of the main goals of the FIREbox project is to study the distribution of the various gas phases in and around galaxies at high spatial resolution. As such, it aims to provide a theoretical counterpart to the large number of observational efforts currently being undertaken to map the gas content of galaxies on sub-galactic (few hundreds of parsecs or better) scales, such as THINGS (Walter et al. 2008), LITTLE THINGS (Hunter et al. 2012), HI-MaNGA (Masters et al. 2019), ALMAQuest (Lin et al. 2020), PHANGS-ALMA (Leroy et al. 2021a), and PHANGS-MUSE (Emsellem et al. 2022).

We illustrate the ability of FIREbox to model and spatially resolve the multiphase ISM in Fig. 3. Here, we show gas maps as well as colour-composite images of stellar light for a FIREbox galaxy at $z = 0$. The halo mass of this chosen galaxy ($1.3 \times 10^{12}\ M_\odot$) matches the estimated halo mass of the MW (Bland-Hawthorn & Gerhard 2016). Overall, this galaxy is a fairly typical example of a MW analog in FIREbox. We will discuss the properties of MW analogs in FIREbox more generally in Section 3.4.

Downloaded from https://academic.oup.com/mnras/article/522/3/3831/7140530 by Northwestern University School of Law user on 03 July 2023

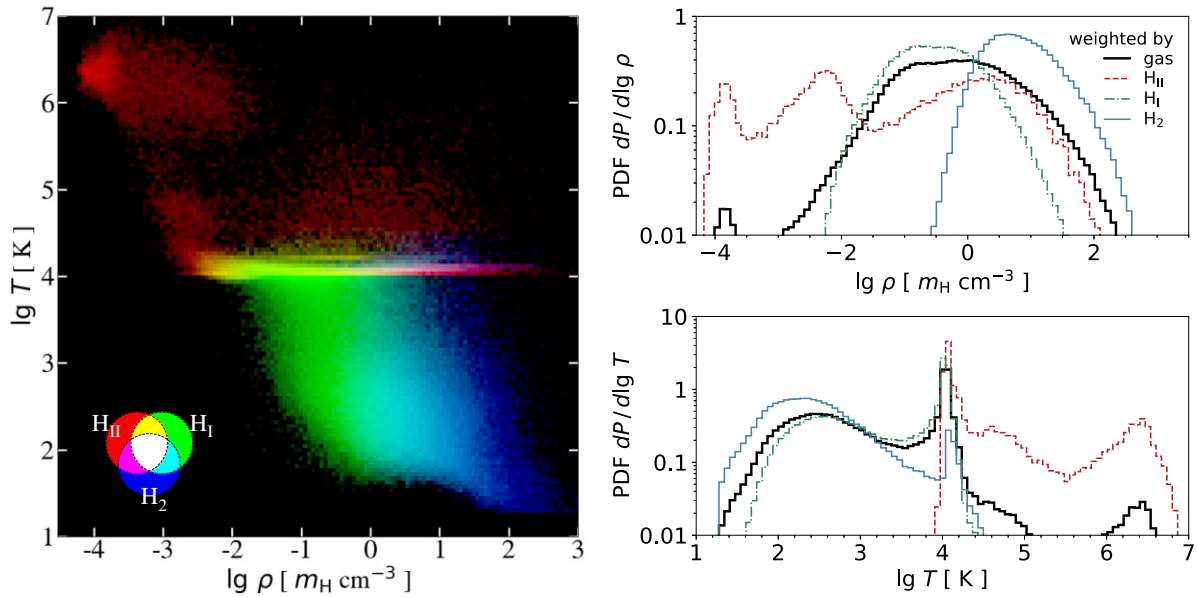

Figure 4. Thermal properties of the ISM of a MW-like galaxy at $z = 0$ in FIREbox. (Left) Phase diagram of hydrogen gas within a $0.1R_{\rm vir} \sim 29$ kpc radius of the centre of the galaxy. Densities (ρ) and temperatures (T) vary over many orders of magnitude ($\sim 10^{-4}$–10^{3} $\rm m_H\ cm^{-3}$ and 10–10^{7} K), highlighting the computational challenge for galaxy formation simulations. The phase diagram is colour-coded according to the hydrogen phase, see legend. The hydrogen phase is not uniquely determined by gas density and temperature alone. (Top right) Fraction of gas within $0.1R_{\rm vir}$ having density ρ per unit lg ρ. (Bottom right) Fraction of gas within $0.1R_{\rm vir}$ having temperature T per unit lg T. In both right-hand panels, particle number fractions are weighted by gas mass (thick black solid line), ionized hydrogen mass (red dashed line), atomic hydrogen mass (green dot–dashed line), and molecular hydrogen mass (blue solid line). The small fraction of molecular gas with temperatures near 10^4 K is an artifact of the approximate treatment of separating neutral gas into atomic and molecular components, see Section 2.2. Neutral hydrogen consists of a combination of cold ($\sim$100–1000 K) and warm ($\sim 10^4$ K) gas, while ionized gas consists of a hot, dilute ($\sim 10^{-4}$ $\rm m_H\ cm^{-3}$) phase filling most of the volume (the diffuse hot halo), a warm/hot, low density ($\sim 10^{-3}$–10^{-2} $\rm m_H\ cm^{-3}$) phase that forms a discy layer around the neutral ISM disc (see Fig. 3), and warm ionized, relatively dense gas located in the plane of the ISM disc.

According to Fig. 3, this galaxy has a well-defined disc morphology. Face-on and edge-on images in U, V, and J broadband filters, created with the help of the Monte Carlo radiative transfer code SKIRT[5] (Baes et al. 2011; Camps & Baes 2015), show young clusters of stars, patchy lanes of dust, and an underlying stellar disc that extends out to about 15–18 kpc. Face-on gas maps of the molecular, atomic, and ionized components of the ISM reveal a complex and intricate structure. Neutral hydrogen forms a relatively thin, but flocculent, disc with much of the molecular component residing in the inner, denser regions of the gas disc. Significant amounts of $\rm H_I$ gas can be found at large distances (>25 kpc) from the galaxy centre, i.e. far beyond the extent of the stellar disc, see also Trapp et al. (2022).

The vertical scale heights of the $\rm H_I$ and $\rm H_2$ discs at $R \sim 8$ kpc for this simulated galaxy are approximately 200 ± 50 and 130 ± 70 pc when measured by fitting the vertical density profile in annulus sectors with a Gaussian (Gensior et al. 2022). These scale heights are comparable (within a factor of 2–3) with estimates for the MW (Bacchini et al. 2019b), M33 (Combes et al. 2012), and nearby star-forming galaxies (Bacchini et al. 2019a). The $\rm H_I$ disc remains thin and regular out to about 20 kpc and shows warping at larger radii.

Most of the ionized gas surrounding this galaxy is part of a diffuse, hot circum-galactic medium filling much of the volume of the DM halo. However, ionized gas can also be found in a puffed-up discy layer surrounding the neutral ISM, possibly a rotating cooling flow that replenishes the disc with gas (Hafen et al. 2022), as well as in a thin disc within the plane of the neutral gas disc, often near the locations of young star clusters.

Fig. 4 explores further the thermal properties and phase structure of the gas in the selected MW analog. The gas within $0.1R_{\rm vir} \sim 29$ kpc varies broadly in density and temperature ($\sim 10^{-4}$–10^{3} $\rm m_H\ cm^{-3}$ and 10–10^{7} K) and consists of ionized, atomic, and molecular phases. In this example galaxy, most of the hydrogen gas within $0.1R_{\rm vir}$ is atomic (70 per cent). Molecular and ionized hydrogen contribute at the 22 per cent and 8 per cent level, respectively. When split by temperature, gas with $T < 6000$ K is pre-dominantly neutral, while gas with $T > 15\,000$ K is pre-dominantly ionized. The ionized gas is made up of three sub-components: a hot, dilute ($\sim 10^{-4}$ $\rm m_H\ cm^{-3}$) phase filling most of the volume (the diffuse hot halo), a warm/hot, low density ($\sim 10^{-3}$–10^{-2} $\rm m_H\ cm^{-3}$) phase that forms a smooth discy layer around the neutral ISM disc, and a warm ionized phase of relatively dense gas near the centre plane of the ISM disc.

3.2 The star-forming sequence

SFRs and stellar masses of star-forming galaxies are tightly correlated with a redshift-dependent normalization (Brinchmann et al. 2004; Elbaz et al. 2007; Noeske et al. 2007). This empirical relation, the star-forming 'main sequence', links the star formation history of a galaxy (via its stellar mass) to its current star formation activity, making it an important empirical constraint for theoretical models. The precise functional form of the star-forming sequence is still somewhat uncertain given that it has been measured with a variety of different observational techniques and for galaxy samples subject to different selection effects (Speagle et al. 2014; Davies et al.

[5] http://www.skirt.ugent.be.

Downloaded from https://academic.oup.com/mnras/article/522/3/3831/7140530 by Northwestern University School of Law user on 03 July 2023

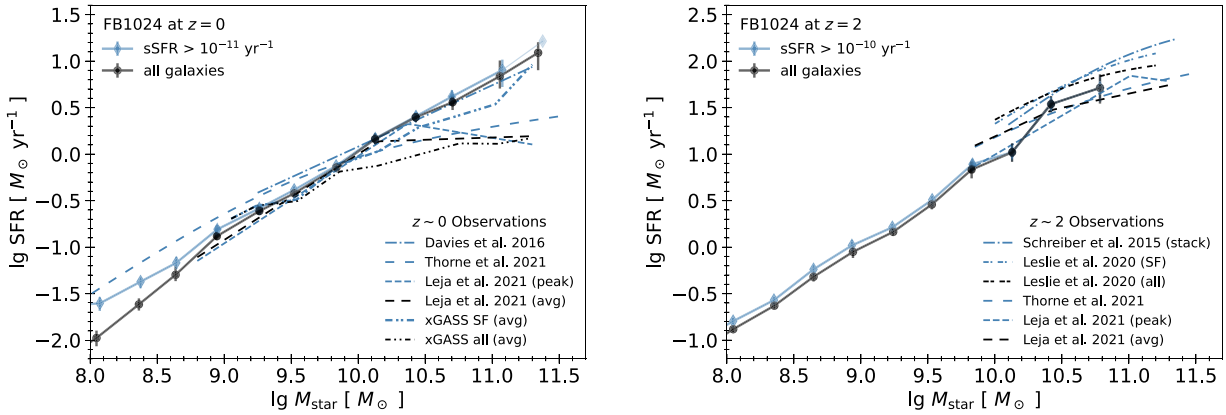

Figure 5. Star-forming sequence in FIREbox and in observations at $z = 0$ (left) and $z = 2$ (right). Symbols show the logarithm of the average SFR in bins of stellar mass for all galaxies (black circles) and for star-forming galaxies (blue diamonds) in FIREbox. The latter population of galaxies is defined as having sSFRs exceeding 10^{-11} yr^{-1} at $z = 0$ and 10^{-10} yr^{-1} at $z = 2$. SFRs are averaged over the past 20 Myr. Error bars refer to 16–84 per cent percentiles in each bin obtained via bootstrapping. Light shaded symbols without error bars indicate bins containing fewer than four galaxies. Double dot–dashed lines show the star-forming sequence for a representative sample of $z \sim 0$ galaxies from the xGASS survey (Catinella et al. 2018) with updated stellar masses as presented in Feldmann (2020). Dashed and dot–dashed lines show results of recent observational studies (Schreiber et al. 2015; Davies et al. 2016; Leslie et al. 2020; Thorne et al. 2020; Leja et al. 2022), see legend. Stellar masses by Leslie et al. (2020) are shifted by 0.2 dex to account for the known systematics of their stellar mass catalog. FIREbox predicts average SFRs of star-forming galaxies in good agreement with observations.

2016). However, advances in recent years, e.g. access to multiband (UV to FIR) photometry (e.g. Schreiber et al. 2015; Davies et al. 2016) and improved modelling techniques (Chevallard & Charlot 2016; Johnson et al. 2021; Leja et al. 2017), have resulted in more robust determinations of stellar masses and SFRs across cosmic history (e.g. Thorne et al. 2020; Leja et al. 2022). In principle, accurate measurements of different star formation tracers even allow constraints on the short-time-scale variability of SFRs (Sparre et al. 2017; Flores Velázquez et al. 2021).

Fig. 5 compares the star-forming sequence in FIREbox with the observed one in today's Universe ($z = 0$) and at Cosmic Noon ($z = 2$). Specifically, we plot the logarithm of the average SFR in bins of stellar mass both for galaxies in FIREbox ('all') as well as for those galaxies that are actually star forming ('SF'). The latter are defined to exceed a specific SFR (sSFR) of 10^{-11} yr^{-1} at $z = 0$ and 10^{-10} yr^{-1} at $z = 2$. These limits approximately remove 'quiescent' galaxies, i.e. galaxies with SFRs, that are an order of magnitude or more below the star-forming sequence at the considered redshifts. SFRs in FIREbox are averaged over the past 20 Myr. We find only minimal changes (<0.05 dex) for the slope and normalization of the star-forming sequence of $M_{\rm star} > 10^9\,M_\odot$ galaxies when we adopt a 5 or 100 Myr averaging time instead.

We compare these theoretical predictions with fits to observational data reported in recent studies (Schreiber et al. 2015; Davies et al. 2016; Leslie et al. 2020; Thorne et al. 2020; Leja et al. 2022). We also analyse a representative sample of low redshift galaxies from the xGASS survey (Catinella et al. 2018) with updated stellar masses, as presented in Feldmann (2020). SFRs smaller than their measurement uncertainties are set to their measurement uncertainty. We refer to Feldmann (2020) for a more systematic, parametric approach that simultaneously constrains the slope of the star-forming sequence and the corresponding atomic and molecular gas sequences.

When we look at the main sequence of star-forming galaxies in FIREbox, we find generally good agreement with observational data at both $z = 0$ and $z = 2$. Being able to reproduce the slope and normalization of the star-forming sequence is a significant achievement of the FIRE-2 model given that the simulation is not tuned to reproduce this (or any other) relation. Our finding also agrees qualitatively with a similar result for galaxies in FIRE-2 zoom-in simulations at $z = 0$ (Gandhi et al. 2022).

The star-forming sequence in FIREbox at $z = 0$ and $z = 2$ is well described by a linear function (in log-log space) over a broad range in stellar mass, i.e.

$$y = A + \alpha_1 (x - 10), \tag{1}$$

where $y = \lg \langle {\rm SFR}/(M_\odot\,{\rm yr}^{-1}) \rangle$ is the logarithm of the average SFR of galaxies and $x = \lg (M_{\rm star}/M_\odot)$ is the logarithm of the stellar mass. Fit results are listed in Table 2.

Focusing on $z = 0$ galaxies with sSFR $> 10^{-11}$ yr^{-1} and $M_{\rm star} = 10^9 - 10^{11}\,M_\odot$, we obtain a slope of $\alpha_1 = 0.85$ and a normalization of $A = 0.03$. Excluding satellite galaxies reduces the slope slightly to 0.80. Either slope is somewhat steeper than the analogously calculated slope of ∼0.68 for star-forming galaxies with $M_{\rm star} = 10^{9\text{–}11}\,M_\odot$ in the xGASS sample. The normalization of star-forming sequence in xGASS is very similar, however, differing by only about 0.1 at the $M_{\rm star} = 10^{10}\,M_\odot$ pivot mass.

Both the normalization and the slope of the star-forming sequence depend on redshift. The normalization of the star-forming sequence increases by about one order of magnitude when going from $z = 0$ to $z = 2$ while the slope steepens, becoming near linear (∼0.94) at $z = 2$ (or 0.95 if satellites are excluded). A linear slope would imply a mass-independent star formation time-scale $M_{\rm star}$/SFR (Schreiber et al. 2015) and could help explain the invariant shape of the SMF of star-forming galaxies (Peng et al. 2010). Furthermore, as discussed in Feldmann (2020), the slope of the star-forming sequence is naturally linked to the evolution of gas masses in galaxies, and it becomes linear if the gas mass histories of galaxies have all the same shape. A sufficient but not necessary condition for the latter scenario is that galaxies are close to 'equilibrium' (Bouché et al. 2010; Davé, Finlator & Oppenheimer 2012), i.e. the masses of their ISM evolve only mildly with redshift as frequently seen in models across broad redshift and mass ranges (Finlator & Davé 2008). A non-linear slope (as found at low z) may instead suggest 'downsizing' of the gas mass, i.e. more massive galaxies reach their maximum gas masses at earlier times and subsequently have faster declining gas masses at

Downloaded from https://academic.oup.com/mnras/article/522/3/3831/7140530 by Northwestern University School of Law user on 03 July 2023

Table 2. Parameters of galaxy scaling relations in FIREbox. The first column refers to the selected galaxy population or 3D aperture, see Sections 3.2, 3.3, and 3.5. The second column provides the stellar mass range over which the fit was performed. In each case, we fit lg $\langle Q \rangle$ as a function of lg $M_{\rm star}$, where $\langle Q \rangle$ is the average SFR, atomic hydrogen mass, molecular hydrogen mass, gas-phase oxygen abundance, or stellar iron abundance for all considered galaxies in the given stellar mass bin. The star-forming sequence is well fit by a linear function (equation 1) over the quoted mass regime with normalization A (column 3) and slope α_1 (column 4). Similarly, the gas and metallicity sequences are well fit by a broken linear function (equation 2) over the quoted mass regime with the parameters listed in columns 3–7.

Selection	Mass	A	α_1	$x_{\rm b}$	α_2	Δ
		Star-forming sequence at $z = 0$				
sSFR $> 10^{-11}$ yr^{-1}	9–11	0.03	0.85	–	–	–
all galaxies	9–11	0.01	0.84	–	–	–
		Star-forming sequence at $z = 2$				
sSFR $> 10^{-10}$ yr^{-1}	8–11	1.00	0.94	–	–	–
All galaxies	8–11	0.98	0.97	–	–	–
		Atomic hydrogen sequence at $z = 0$				
within 30 kpc	7–11.5	8.86	0.85	8.55	0.37	0.21
within $0.1R_{\rm vir}$	7–11.5	8.41	1.15	8.10	0.41	0.39
		Molecular hydrogen sequence at $z = 0$				
within 10 kpc	7–11.5	8.68	1.59	9.82	0.26	0.39
within $0.1R_{\rm vir}$	7–11.5	8.52	1.59	9.65	0.56	0.30
		Gas-phase oxygen abundance at $z = 0$				
within 3 kpc	6.5–11.5	9.29	0.58	10.28	0.19	0.07
within $0.1R_{\rm vir}$	6.5–11.5	9.15	0.57	10.21	−0.18	0.18
		Stellar iron abundance at $z = 0$				
within 3 kpc	6.5–11.5	7.39	0.53	10.05	0.13	0.23
within $0.1R_{\rm vir}$	6.5–11.5	7.37	0.51	10.28	0.01	0.37

late times. We plan to analyse the link between gas masses and SFRs in more detail in future work.

At $z = 2$, a single power-law describes the star-forming sequence well both for the 'all' and the 'SF' sample down to $M_{\rm star} = 10^8\ M_\odot$. In contrast, at $z = 0$, we observe a steepening of the slope for the 'all' sample below $M_{\rm star} = 10^9\ M_\odot$. The difference between the $z = 0$ 'all' and 'SF' samples at low masses is a consequence of a significant number of low mass, central galaxies with very low or vanishing sSFR in FIREbox.

An important difference with observational data is the low fraction of massive, quiescent galaxies in FIREbox, see Fig. 6. Consequently, the average SFR (at fixed stellar mass) of all galaxies in FIREbox is very similar to the average SFR of star-forming galaxies alone (except at the lowest masses). While the quiescent fraction is indeed low at early cosmic times, e.g. ~ 70 per cent $-$ 80 per cent of galaxies with $M_{\rm star} \sim 10^{11}\ M_\odot$ are star forming at $z = 2$ (Behroozi et al. 2019), massive galaxies ($M_{\rm star} \sim 10^{11}\ M_\odot$) are usually ($\sim 65$ per cent) quiescent in today's Universe (Moustakas et al. 2013; Muzzin et al. 2013; Behroozi et al. 2019; Leja et al. 2022).

Fig. 6 shows the quiescent fraction in FIREbox both for central galaxies, satellites, and the full sample. Here, a galaxy is defined as quiescent at $z = 0$ if its sSFR averaged over the last 100 Myr is below a threshold of either $10^{-10.5}$ yr^{-1} or 10^{-11} yr^{-1}. We also include the data from Leja et al. (2022) for the case of a 100 Myr SFR averaging time and a sSFR-based cut of $10^{-10.5}$ yr^{-1} to separate quiescent and star-forming galaxies. Additionally, we plot the predictions of an empirical model by Behroozi et al. (2019) based on low z observational data (Bauer et al. 2013; Muzzin et al. 2013).

In FIREbox, 10–20 per cent of moderately low-mass galaxies ($M_{\rm star} \sim 10^9\ M_\odot$) are quiescent in agreement with observational data. However, FIREbox significantly underpredicts the quiescent fraction in more massive galaxies. For instance, 30 per cent of $M_{\rm star} \sim 10^{11.2}$ $M_\odot$ galaxies are quiescent in FIREbox (for a $10^{-10.5}$ yr^{-1} sSFR cut), compared with 70–80 per cent in observations (Muzzin et al. 2013; Leja et al. 2022). Hence, stellar feedback alone (at least if modelled as in FIRE-2) is not sufficient to reproduce the observed fraction of massive, quiescent galaxies at $z \sim 0$. Evidently though, some massive, quiescent central galaxies can form even without additional feedback sources. However, these quiescent galaxies should be seen as an extension of the star-forming sequence towards low SFRs and not as truly passively evolving ('quenched') galaxies, given that the majority of them have sSFR between $10^{-10.5}$ yr^{-1} and 10^{-11} yr^{-1}. Perhaps they are related to the observed transition galaxies (Fang et al. 2018). We conclude that alternative forms of feedback, such as cosmic ray feedback (e.g. Booth et al. 2013; Salem & Bryan 2014; Chan et al. 2019; Hopkins et al. 2020) and AGN feedback (e.g. Springel, Di Matteo & Hernquist 2004; Croton et al. 2006; Vogelsberger et al. 2013; Wellons et al. 2023), are needed to reproduce observational data. Indeed, recent cosmological simulations with AGN feedback reproduce well the observed quiescent fraction at $z = 0$ (e.g.Furlong et al. 2015; Donnari et al. 2019).

At low stellar masses ($10^8\ M_\odot < M_{\rm star} < 10^9\ M_\odot$), the quiescent fraction increases with decreasing mass. For instance, FIREbox predicts that for our chosen 100 Myr averaging time of star formation, 40–50 per cent of all $M_{\rm star} \sim 10^8\ M_\odot$ galaxies are quiescent (the number reduces slightly to 35-45 per cent if only central galaxies are considered), see also Feldmann (2017). The quiescent fraction is higher among satellite galaxies than centrals (for $M_{\rm star} < 10^{10}\ M_\odot$), likely as a result of environmental quenching processes (e.g. Simha et al. 2009; Feldmann et al. 2011; Peng et al. 2012; Wetzel et al. 2013; Samuel et al. 2022). The high quiescent fraction at low stellar masses ($M_{\rm star} < 10^9\ M_\odot$), especially among centrals, may be in tensions with observations (Geha et al. 2012). We find that the averaging time of the SFR has a significant impact on the quiescent fraction at the low-mass end. For a 10^{-11} yr^{-1} sSFR threshold, increasing the averaging time to 500 Myr reduces the quiescent fraction of centrals

Downloaded from https://academic.oup.com/mnras/article/522/3/3831/7140530 by Northwestern University School of Law user on 03 July 2023

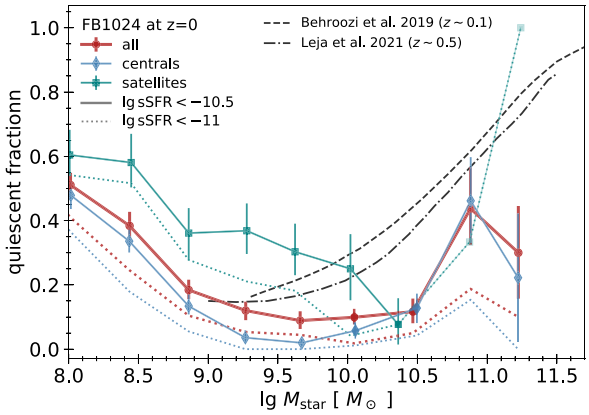

Figure 6. The fraction of quiescent galaxies in FIREbox at $z = 0$. Symbols and solid lines show the fraction of galaxies (red circles), central galaxies (blue diamonds), and satellite galaxies (green squares) with sSFRs below $10^{-10.5}$ yr^{-1}. Dotted lines are the corresponding results for a sSFR threshold of 10^{-11} yr^{-1}. Error bars refer to 16–84 per cent percentiles in each bin obtained via bootstrapping. Light shaded symbols without error bars indicate bins containing fewer than four galaxies. Dot–dashed and dashed lines are observational and empirical estimates of the quiescent fraction by Leja et al. (2022) and Behroozi et al. (2019). SFRs of FIREbox galaxies are averaged over the last 100 Myr as in Leja et al. (2022). At $M_{\rm star} \lesssim 10^{10}$ $M_\odot$, satellite galaxies have a higher quiescent fraction than central (or all) galaxies, presumably as a result of environmental effects (e.g. Simha et al. 2009; Feldmann, Carollo & Mayer 2011; Peng et al. 2012; Wetzel et al. 2013; Samuel et al. 2022). FIREbox generally underpredicts the quiescent fraction among massive galaxies when compared with observations. The difference is most severe at the highest masses $M_{\rm star} > 10^{11}$ $M_\odot$ but a significant difference is also seen in galaxies of intermediate mass $M_{\rm star} \sim 10^{9.5-10.5}$ $M_\odot$. Lowering the threshold from $10^{-10.5}$ yr^{-1} to 10^{-11} yr^{-1} reduces the quiescent fraction significantly, which shows that most quiescent, massive galaxies in FIREbox are not fully quenched.

with $M_{\rm star} = 10^{8.5}$ $M_\odot$ from 16 per cent to 4.8 per cent (and from 37 per cent to 12 per cent for $M_{\rm star} = 10^8$ $M_\odot$ centrals). In contrast, reducing the averaging time to 20 Myr increases the quiescent fraction to 26 per cent at $M_{\rm star} = 10^{8.5}$ $M_\odot$ and to 60 per cent at $M_{\rm star} = 10^8$ $M_\odot$. The dependence of the quiescent fraction on the averaging time is likely a consequence of the bursty nature of star formation in low-mass FIRE galaxies (Sparre et al. 2017; Flores Velázquez et al. 2021). Numerical resolution may also play a role here, resulting in excessive burstiness at low stellar masses (Hopkins et al. 2018; Samuel et al. 2022).

3.3 The gas content of galaxies

Atomic and molecular gas masses of galaxies are correlated with their stellar masses (e.g. Catinella et al. 2010; Saintonge et al. 2011). Inferring the shape of these gas sequences is challenging because of a variety of measurement systematics and selection effects. The availability of 'representative' (in terms of H_I and H_2 content), purely stellar mass-selected galaxy samples (Saintonge et al. 2017; Catinella et al. 2018), substantially simplifies this challenges, but biases may still arise from incorrect modelling assumptions and from the treatment of non-detections (e.g. Feldmann 2020).

We compare the gas content of FIREbox galaxies at $z = 0$ with observational data from xGASS (Catinella et al. 2018) and xCOLD GASS (Saintonge et al. 2017) in Fig. 7. Specifically, we compare the average atomic and molecular hydrogen masses ($M_{\rm H_I}$ and $M_{\rm H_2}$) in bins of stellar mass. We lowered the molecular gas masses reported in Saintonge et al. (2017) by a factor of 1.36 to exclude the contribution from Helium and metals. The gas masses of simulated galaxies are measured in 3D spheres of fixed physical radius[6] r: 10 kpc for H_2 and 30 kpc for H_I.

Gas masses ($M_{\rm H_I}$ or $M_{\rm H_2}$) are not detected in a significant fraction of the galaxies in xGASS and xCOLD GASS. This raises a subtle issue for the comparison with FIREbox. Instead of attempting a full forward modelling, we consider three basic possibilities of dealing with undetected sources. First, we include all galaxies in the observational catalog but assume that undetected sources have gas masses that correspond to their detection limit ('all-limit'). Our second analysis is similar to the first, but we assign undetected sources a gas mass of zero ('all-zero'). The average gas mass calculated via these two approaches brackets the true value. Finally, we also calculate average gas masses for only the detected sources ('detections').

According to Fig. 7, the atomic and molecular hydrogen masses of FIREbox galaxies agree well (to usually better than 0.2 dex over the $M_{\rm star} = 10^9$–10^{11} $M_\odot$ mass range) with those of galaxies ('all-limit' or 'all-zero') in xGASS and xCOLD GASS. The figure also shows the average atomic and molecular hydrogen masses of FIREbox galaxies within 10 per cent of the virial radius. The latter masses differ usually only by a small amount (0.2 dex) from the average gas masses calculated in the chosen fixed physical radii.

FIREbox offers a prediction of how the atomic and molecular gas sequences scale towards low stellar masses. We find that a broken-linear scaling (in log-log space) captures the general behavioUr quite well over a broad range in stellar masses ($M_{\rm star} = 10^7$–$10^{11.5}$ $M_\odot$). Specifically, we adopt the following fitting function:

$$y = A + \alpha_1 (x - x_{\rm b}) + (\alpha_2 - \alpha_1) \left[\ln \left(1 + e^{\frac{x - x_{\rm b}}{\Delta}} \right) - \ln 2 \right] \Delta, \qquad (2)$$

where $y = \lg\langle M_{\rm H_I}/M_\odot \rangle$ ($y = \lg\langle M_{\rm H_2}/M_\odot \rangle$) is the logarithm of the average atomic (molecular) hydrogen mass in galaxies of a given stellar mass with $x = \lg(M_{\rm star}/M_\odot)$. This function has five fit parameters: an overall amplitude (A), a break stellar mass ($x_{\rm b}$), a slope at low stellar masses (α_1), a slope at high stellar masses (α_2), and a parameter determining the smoothness of the transition from the low-mass to the high-mass regime (Δ). For $x \ll x_{\rm b}$, $y \propto \alpha_1 x$, while for $x \gg x_{\rm b}$, $y \propto \alpha_2 x$. The fit parameters are listed in Table 2.

[6]The precise values of these radii are somewhat arbitrary but we chose them for the following reasons. Low-mass galaxies ($M_{\rm star} < 10^{10}$ $M_\odot$) in xGASS and xCOLD GASS are at redshifts $z = 0.01 - 0.02$, while the redshift range of more massive galaxies is $z = 0.025 - 0.5$. The 3.1–3.5 arcmin half power beamwidth of the Arecibo telescope at the relevant frequencies translates into an aperture radius of 21–41 kpc at $z = 0.01$–0.02 and a radius of 51–100 kpc at $z = 0.025$–0.05. A 30 kpc fixed radius is thus a sensible choice for galaxies with $M_{\rm star} < 10^{10}$ $M_\odot$, while for more massive galaxies, we could adopt a larger radius. However, we find that even including all the atomic hydrogen in the virial radius of a $M_{\rm star} = 10^{11}$ $M_\odot$ galaxy ($R_{\rm vir} \sim 280$ kpc) would increase the average H_I mass by only 0.3 dex (and by significantly less in galaxies of lower stellar mass) compared to the 30 kpc fixed radius. The IRAM telescope has a beam width of 22 arcsec at the frequency of the CO (1-0) line, which corresponds to aperture radii of 2.3–4.6 kpc for $z = 0.01$–0.02 and 5.7–11.1 kpc for $z = 0.025$–0.05. Adopting a fixed radius of 3 kpc instead of 10 kpc has only a small impact on the inferred H_2 mass of low-mass FIREbox galaxies but misses a large fraction of the molecular gas mass in massive galaxies, e.g. $M_{\rm H_2}$ is lowered by 0.6 dex on average for a $M_{\rm star} = 10^{11}$ $M_\odot$ galaxy. Furthermore, the reported CO line luminosities in xCOLD GASS are aperture corrected to include contributions at larger radii belonging to the ISM.

Downloaded from https://academic.oup.com/mnras/article/522/3/3831/7140530 by Northwestern University School of Law user on 03 July 2023

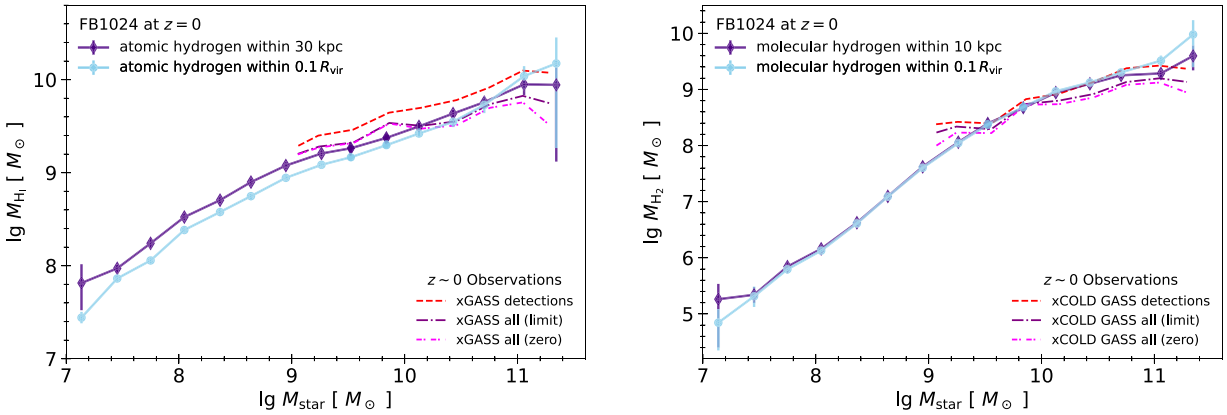

Figure 7. Relationship between the mass of atomic hydrogen (M_{H_I}, left) or molecular hydrogen (M_{H_2}, right) and galaxy stellar mass at $z = 0$ in FIREbox and in observations. Symbols and solid lines show the logarithm of the average H_I or H_2 mass in bins of stellar mass for FIREbox galaxies within a fixed physical radius (purple diamonds) and within 0.1 R_{vir} (light blue circles). Error bars refer to 16–84 per cent percentiles of the logarithm of the average gas mass obtained via bootstrapping. Red dashed lines show analogously computed results for galaxies with detected gas masses (5σ in H_I, 3σ in H_2) from xGASS (Catinella et al. 2018) and xCOLD GASS (Saintonge et al. 2017) with updated stellar masses as presented in Feldmann (2020). Purple (Magenta) dot–dashed lines show corresponding xGASS and xCOLD GASS results when including non-detections by setting the gas mass to the detection limit (to zero). FIREbox predicts average atomic and molecular gas masses in good agreement with these observations. A broken-linear dependence captures well the scaling of M_{H_I} and M_{H_2} with stellar mass, see Table 2.

Both gas sequences have a steeper slope at low stellar masses than at high stellar masses. For atomic hydrogen, we find a low-mass slope near 1 (0.85 for $r = 30$ kpc, 1.15 for $r = 0.1$ R_{vir}), while for molecular hydrogen, the slope is super-linear (1.6 for both $r = 10$ kpc and $r = 0.1$ R_{vir}). We speculate that the steeper slope in low-mass galaxies is a consequence of stellar feedback and the UV background more strongly regulating their gas content (see e.g. van de Voort et al. 2016; Fitts et al. 2017; Hafen et al. 2019; Pandya et al. 2020). Furthermore, since lower mass galaxies tend to have lower ISM metallicities (e.g. Tremonti et al. 2004; Finlator & Davé 2008) and lower dust-to-metal ratios (e.g. Rémy-Ruyer et al. 2014; Feldmann 2015), a smaller fraction of the neutral ISM is in molecular form (e.g. Krumholz et al. 2008; Gnedin & Kravtsov 2011), thus explaining the steeper slope of the molecular gas sequence compared with the atomic gas sequence. At the high mass end, slopes are sub-linear (0.4 for atomic hydrogen and 0.3–0.6 for molecular hydrogen) qualitatively consistent with the decline of the atomic and molecular gas to stellar mass ratios with increasing stellar mass found observationally (e.g. Saintonge et al. 2017; Catinella et al. 2018) and in models (e.g. Davé et al. 2020). The break stellar mass between the two regimes is $10^{8.1-8.6}$ $M_\odot$ for H_I and $10^{9.6-9.8}$ $M_\odot$ for H_2. We find that galaxies with a stellar mass near the break stellar mass of the atomic (molecular) hydrogen sequence have an atomic (molecular) hydrogen content of $M_{H_I} \sim 10^{8.4-8.9}$ $M_\odot$ ($M_{H_2} \sim 10^{8.5-8.7}$ $M_\odot$).

3.4 The gas content of Milky Way analogs – where are the 'missing' baryons?

A growing number of observational and theoretical studies attest that galaxies like the MW contain fewer baryons in their haloes than expected based on the cosmic average (e.g. Maller & Bullock 2004; Anderson & Bregman 2010; Crain et al. 2010; McGaugh et al. 2010; Feldmann, Hooper & Gnedin 2013; Schaller et al. 2015; van de Voort et al. 2016; Suresh et al. 2017; Tumlinson, Peeples & Werk 2017; Bregman et al. 2018). In this section, we provide a census of the baryons in MW-mass haloes from FIREbox and compare it, for illustrative purposes, with measurements of the various mass components in the Galaxy and its halo. To this end, we selected all 23 FIREbox main haloes with virial masses between 7.5×10^{11} $M_\odot$ and 2.5×10^{12} $M_\odot$ at $z = 0$. One system, a late stage, galaxy major merger, was excluded from the analysis below. The average halo mass of this sample is 1.3×10^{12} $M_\odot$ matching the current consensus estimate of the virial mass of the MW (Bland-Hawthorn & Gerhard 2016). The average virial radius of the sample is 279 kpc.

The MW contains about 8×10^9 $M_\odot$ of atomic hydrogen (Kalberla & Dedes 2008; McMillan 2017; Cautun et al. 2020) and $\sim(1 \pm 0.3) \times 10^9$ of molecular hydrogen (Heyer & Dame 2015; McMillan 2017). Both mass estimates are subject to large modelling uncertainties and are reported here without contributions from metals and Helium. While they only account for the gas in the MW disc and centre, the neutral hydrogen mass in MW satellites is relatively low. The Large Magellanic Cloud (LMC, Small Magellanic Cloud) contributes about 5×10^8 $M_\odot$ in atomic hydrogen (Kim et al. 1999; 4×10^8 $M_\odot$, Stanimirovic et al. 1999) and $\sim 5 \times 10^7$ $M_\odot$ in H_2 (Fukui et al. 1999) with some additional neutral gas in the Magellanic bridge, stream, and leading arm (e.g, Nidever et al. 2010; Besla et al. 2012). In comparison, FIREbox predicts an average atomic hydrogen mass of $6.37^{+1.27}_{-1.05} \times 10^9$ $M_\odot$ and a molecular hydrogen mass of $1.79^{+0.22}_{-0.27} \times 10^9$ $M_\odot$ within 10 per cent of R_{vir}, both in reasonable agreement with observations. Here, sub- and superscripts refer to 16th and 84th percentiles of the averages obtained via bootstrapping. For the mass of neutral hydrogen, FIREbox predicts $8.16^{+1.54}_{-1.36} \times 10^9$ $M_\odot$, which can be compared with the observed value of $\sim 9 \times 10^9$ $M_\odot$.

The mass of the warm-hot and hot gaseous halo (corona) around the MW has been constrained to $2.5 \pm 1 \times 10^{10}$ $M_\odot$ via a variety of independent observables (Bland-Hawthorn & Gerhard 2016), including X-ray emission (Miller & Bregman 2015), pulsar-based dispersion measures from the LMC (Anderson & Bregman 2010), H_α emission from the Magellanic H_I stream (Bland-Hawthorn & Gerhard 2016), and ram-pressure effects on the LMC gas disc (Salem et al. 2015). A more recent estimate by Bregman et al. (2018) based on a combined analysis of a variety of observational data is $2.8 \pm 0.5 \times 10^{10}$ $M_\odot$ of hot gas within 250 kpc of the MW. FIREbox predicts an average mass of gas with $T > 2 \times 10^5$ K of $3.24^{+0.64}_{-0.62} \times 10^{10}$ $M_\odot$ within the virial radii of MW-like haloes ($3.18^{+0.64}_{-0.60} \times 10^{10}$ $M_\odot$ within $0.1 - 1 \times R_{vir}$), in good agreement with

Downloaded from https://academic.oup.com/mnras/article/522/3/3831/7140530 by Northwestern University School of Law user on 03 July 2023

the observational estimates. These gas masses include contributions from Helium and metals. This warm-hot and hot gas amounts to 58 per cent of the total gas mass in such haloes, and it exceeds the 35 per cent fraction of cooler gas ($M_{\rm gas}(T < 2 \times 10^4 K) = 1.9 \times 10^{10}$ $M_\odot$). Gas at intermediate temperatures ($2 \times 10^4 \leq T/{\rm K} \leq 2 \times 10^5$) contributes only about 7 per cent, as expected from the high cooling rate in this temperature range.

Numerical models predict that hot haloes around galaxies are strongly affected by galactic winds driven by feedback (e.g. van de Voort et al. 2016; Hafen et al. 2019; Stern et al. 2021b; Vijayan & Li 2021). Observations with future X-ray telescopes may be able to measure the diffuse halo gas in L_* galaxies out to moderate redshifts (Kaastra et al. 2013; Simionescu et al. 2021), thus potentially providing a sensitive probe of the physics of feedback processes. We plan to study the formation and evolution of hot haloes in FIREbox galaxies in future work.

As mentioned above, the observed baryonic content of the MW halo falls short of the amount expected from the universal baryon fraction (McGaugh et al. 2010). Current observational estimates provide a baryon fraction ($M_{\rm b}/M_{\rm halo}$) of only 7 per cent (Bland-Hawthorn & Gerhard 2016), i.e. less than half of $\Omega_{\rm b}/\Omega_{\rm m} =$ 15.7 per cent. Whether significant amounts of halo baryons have evaded detection so far or whether they are truly 'missing' from the halo is still debated. In FIREbox, the baryon fraction of MW-like haloes at $z = 0$ is $11.6^{+0.5}_{-0.4}$ per cent, i.e. only about 25 per cent of the cosmic baryons are missing from MW haloes, i.e. reside outside the halo either because they were removed at some point or never accreted in the first place.

The remaining 'extra' baryons, compared with observations, are distributed among various matter components. First, a significant amount ($\sim 7 \times 10^9$ $M_\odot$) of ionized gas in MW-like haloes in FIREbox has temperatures below 2×10^5 K, i.e. it is not in a hot phase. Interestingly, estimates based on modelling of the $O_{\rm VI}$ absorption line of $L*$ galaxies predict an even larger average mass of warm ionized gas (Werk et al. 2014). Secondly, the hot gas mass (see discussion above) and the galaxy stellar mass in FIREbox are slightly higher than empirical estimates. The average stellar mass of the centrals in our sample of MW analogs is $5.73^{+0.57}_{-0.53} \times 10^{10}$ $M_\odot$ for $R_{\rm g} = 3\,R_{\rm half}$ ($7.64^{+0.81}_{-0.63} \times 10^{10}$ $M_\odot$ for $R_{\rm g} = 0.1\,R_{\rm vir}$) compared with empirically determined stellar mass of $\sim 5 \times 10^{10}$ $M_\odot$ (Flynn et al. 2006; Cautun et al. 2020) for the MW. Finally, haloes of MW analogs in FIREbox harbour a significant amount of stars in a smooth extra-galactic component ($2.4^{+0.3}_{-0.3} \times 10^{10}$ $M_\odot$ for a galaxy size of $R_{\rm g} = 3\,R_{\rm half}$, $5.6^{+0.8}_{-1.0} \times 10^9$ $M_\odot$ for $R_{\rm g} = 0.1\,R_{\rm vir}$) and in satellite galaxies ($\sim 9 \times 10^9$ $M_\odot$). This extra-galactic stellar component exceeds current observational estimates of the 'stellar halo' of the MW ($\sim 1.4 \times 10^9$ $M_\odot$ Deason, Belokurov & Sanders 2019; Mackereth & Bovy 2020). However, the latter estimates involve various modelling and selection steps that will need to be properly taken into account, e.g. via forward modelling of our simulated galaxies, to allow for a direct, quantitative comparison.

3.5 Mass–metallicity relation

The metallicity of the ISM is set by a complex network of processes including metal injections from supernovae (Woosley & Weaver 1995; Nomoto et al. 2006), star formation, galactic outflows that remove metals from galaxies, and inflows of comparably metal-poor gas from the cosmic environment (Sánchez Almeida et al. 2014; Muratov et al. 2015, 2017). The observation of a correlation between ISM metallicity and the stellar mass of galaxies, the mass–metallicity relation (MZR; Tremonti et al. 2004), may thus provide insights into the role these processes play in galaxy evolution. Various physical mechanisms have been proposed to explain the MZR, including the ejection of metal-rich gas from low-mass haloes by supernova feedback (Dekel & Silk 1986; Dekel & Woo 2003), inefficient star formation (due to feedback in the ISM) in low-mass galaxies (Brooks et al. 2006), and the potential under-abundance of massive stars in low-mass galaxies as a result of clustered star formation (Köppen, Weidner & Kroupa 2007).

In the equilibrium model of galaxy formation (Larson 1972; Finlator & Davé 2008; Davé et al. 2012; Feldmann 2013; Lilly et al. 2013; Dekel & Mandelker 2014), the ISM metallicity is set by the present balance of metal enrichment, removal, and dilution processes with any memory of the past enrichment level erased over a few gas depletion times. In this model, the star formation activity in a galaxy adjust such that stellar feedback driven outflows roughly balance any gas inflows, resulting in gas and metal masses in the ISM that are approximately constant in time. Low-mass galaxies tend to have large mass-loading factors (Muratov et al. 2015; Anglés-Alcázar et al. 2017a; Pandya et al. 2021), and thus require only small SFRs to achieve this balance, resulting in low equilibrium metallicities (Finlator & Davé 2008). The self-regulatory feature of this model also helps to explain why the MZR has such a small scatter. Furthermore, by allowing for evolving ISM masses, this model naturally introduces a dependence of the ISM metallicity on SFR at fixed stellar mass (Lilly et al. 2013) as potentially observed (Mannucci et al. 2010; Sanders et al. 2021).

While the metallicity of the ISM is expected to quickly reach equilibrium values under most circumstances, the metallicity in the photosphere of stars is determined to a large degree by the metallicity of the molecular clouds they formed from. The stellar metallicity of galaxies thus reflects both the past ISM metallicity, the star formation history, and the accretion of stars in galaxy mergers. In addition, it may hold clues to the nature and time-scale of galaxy quenching (Peng, Maiolino & Cochrane 2015). Similar to ISM metallicities, the stellar metallicities of observed galaxies are found to correlate with their stellar masses (Gallazzi et al. 2005).

We compare the gas phase and stellar metallicities of FIREbox with observational data in Fig. 8. Observed oxygen abundances are reproduced in the figure as originally reported (Tremonti et al. 2004; Lee et al. 2006; Sánchez et al. 2019). Kirby et al. (2013) assumed a Solar iron abundance of 7.52 (consistent with Asplund et al. 2009), and we use this value to convert their results from relative to absolute abundances. Gallazzi et al. (2005) measured stellar metallicities (relative to Solar) via stellar absorption indices based primarily on magnesium and iron lines. We equate their reported metallicities with iron abundances relative to Solar and convert to absolute values using again a Solar iron abundance of 7.52. To aid the comparison with observations, we measure metallicities in FIREbox in a 3D aperture radius of 3 kpc to match approximately the 1.5 arcsec radius of SDSS fibers at the median redshift ($z \sim 0.1$) of the samples of Tremonti et al. (2004) and Gallazzi et al. (2005). However, since this radius is too small to include gas in the outskirts of larger galaxies, we also provide a more scale-invariant aperture choice of $0.1R_{\rm vir}$. To account for oxygen depletion inside H II regions, we reduce the oxygen abundance predicted by the simulation by 0.12 dex (Peimbert & Peimbert 2010). This quantitative comparison likely suffers from additional systematic uncertainties related to, e.g. the observational metallicity calibration, as well as the metal yields and supernova rates adopted by the simulation (Hopkins et al. 2018), all of which are beyond the scope of this paper.

To highlight the general trend between metallicity and stellar mass, we aggregate the metallicities of FIREbox galaxies in 0.3

Downloaded from https://academic.oup.com/mnras/article/522/3/3831/7140530 by Northwestern University School of Law user on 03 July 2023

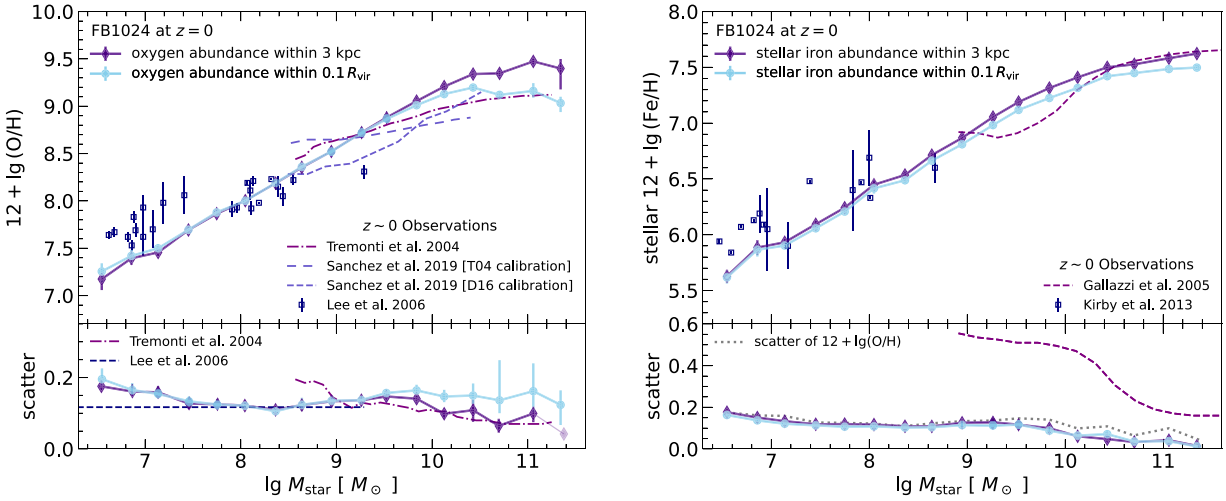

Figure 8. Relationship between the gas-phase oxygen abundance (left) or stellar iron abundance (right) and galaxy stellar mass at $z = 0$ in FIREbox and in observations. In the upper-left panel, solid lines show the logarithm of the average oxygen abundance plus 12 for FIREbox galaxies in bins of stellar mass for a 3 kpc fixed physical radius (purple diamonds) or within 0.1 R_{vir} (light blue circles). Error bars (16–84 percentiles) are obtained via bootstrapping. Light shaded symbols without error bars indicate bins containing fewer than four galaxies. Observational data (Tremonti et al. 2004; Lee et al. 2006; Sánchez et al. 2019) are included in the figure as dot–dashed lines, square symbols, and dashed lines. The scatter (one half of the 16–84 per cent percentile range) of the logarithmic oxygen abundance at a fixed stellar mass is shown in the lower-left panel. FIREbox predicts that the stellar mass–gas phase metallicity relation has low scatter (∼0.1–0.2) both in massive and low-mass galaxies. The panels on the right-hand side are analogous to the panels on the left but for the stellar iron abundance instead of the gas-phase oxygen abundance. Observational data are from Gallazzi et al. (2005) (dashed lines) and Kirby et al. (2013; square symbols). Broken-linear dependences capture well the scaling of the gas-phase oxygen abundance and stellar iron abundance with stellar mass in FIREbox, see Table 2. The scatter of the stellar mass–stellar metallicity relation in FIREbox increases towards lower stellar masses, but it is generally lower than the scatter of the stellar mass–gas phase metallicity relation (the dotted line in the bottom-right panel reproduces the scatter of the latter relation for a 3 kpc aperture radius as shown in the bottom-left panel).

dex wide bins of stellar mass. Specifically, we show in Fig. 8 the quantities $12 + \lg(\langle \mathrm{O/H} \rangle)$ (top-left panel) and $12 + \lg(\langle \mathrm{Fe/H} \rangle)$ (top-right panel), where $\langle \mathrm{O/H} \rangle$ ($\langle \mathrm{Fe/H} \rangle$) represents the average ratio between the number of oxygen and hydrogen nuclei in the gas phase (the average ratio between the number of stellar iron nuclei and stellar hydrogen nuclei) of FIREbox galaxies in 0.3 dex wide bins of stellar mass. In the bottom panels, we show the corresponding scatter defined as half the difference between the 84 and 16 percentile of $12 + \lg(\mathrm{O/H})$ or $12 + \lg(\mathrm{Fe/H})$ for the galaxies in the given stellar mass bin.

FIREbox broadly reproduces the observed MZR at $z = 0$ over ∼five orders of magnitude in stellar mass (Tremonti et al. 2004; Lee et al. 2006; Sánchez et al. 2019), similar to previous results of FIRE-1 zoom-in simulations (Ma et al. 2016). The match is not perfect, however, as FIREbox possibly slightly overpredicts (underpredicts) the oxygen abundance in galaxies with $M_{star} > 10^{10}\,M_\odot$ (with $M_{star} < 10^{7.5}\,M_\odot$). We caution that this comparison is plagued by calibration systematics, which can exceed 0.2 dex (Kewley & Dopita 2002; Kewley & Ellison 2008; Sánchez et al. 2019). As a specific example, we show the MZR reported by Sánchez et al. (2019) for two different metallicity calibrations; one based on [N II], [S II] and Hα emission lines (Dopita et al. 2016), the other one using [O II], [O III], and Hβ (Pagel et al. 1979; Tremonti et al. 2004).

Matching simultaneously both the observed MZR and the star-forming sequence of low-mass galaxies ($M_{star} \lesssim 10^9\,M_\odot$) has been pointed out as a major challenge for galaxy formation models (Somerville & Davé 2015). The reasonable match between FIREbox and the observational data shown in Figs 5 and 8 suggests that cosmological simulations with the FIRE-2 physics model are a significant step towards overcoming this challenge.

The MZR in FIREbox shows clear evidence of a flattening at the massive end. This flattening has been observed for many metallicity calibrators (e.g. Tremonti et al. 2004; Sánchez et al. 2019). Given its presence in FIREbox, we infer that the flattening of the MZR as reported by observations is likely not merely a consequence of aperture bias (Kirby et al. 2013). Instead, provided the equilibrium view of galaxy formation is correct, the flattening can be explained by the mass-loading factors approaching, and falling below, unity in massive galaxies (Finlator & Davé 2008; Muratov et al. 2015). The relation between mass-loading factor η and equilibrium metallicity is $Z_{eq} \propto y/(1 - R + \eta)$, see Finlator & Davé (2008) and Lilly et al. (2013), where y is the metal yield and $R \sim 0.5$ the mass return fraction (Krumholz & Dekel 2012). The equilibrium metallicity is approximately independent of the mass-loading factor for $\eta \ll 1$.

The MZR can be well fit with a broken linear relation given by equation (2) with $y = 12 + \lg(\langle \mathrm{O/H} \rangle)$ and $x = \lg M_{star}$. The fit parameters are provided in Table 2. For 3 kpc aperture radius, the MZR is sub-linear with a slope of ∼0.6 at low stellar masses and almost flat with a slope of ∼0.2 at high stellar masses. The transition between the two regimes occurs at a break stellar mass of $\sim 10^{10.3}\,M_\odot$.

Focusing on the scatter of the MZR, FIREbox predicts a value of ∼0.1–0.15 for much of the probed stellar mass range, in agreement with observations (Tremonti et al. 2004; Lee et al. 2006). Furthermore, the scatter is predicted to decrease slightly at the massive end if the 3 kpc aperture is used in line with results by Tremonti et al. (2004). However, as shown in the lower-left panel of Fig. 8, the scatter is almost independent of stellar mass if an $0.1R_{vir}$ aperture radius is adopted.

FIREbox predicts a relation between stellar iron abundance and stellar mass that is in approximate agreement with observational data

Downloaded from https://academic.oup.com/mnras/article/522/3/3831/7140530 by Northwestern University School of Law user on 03 July 2023

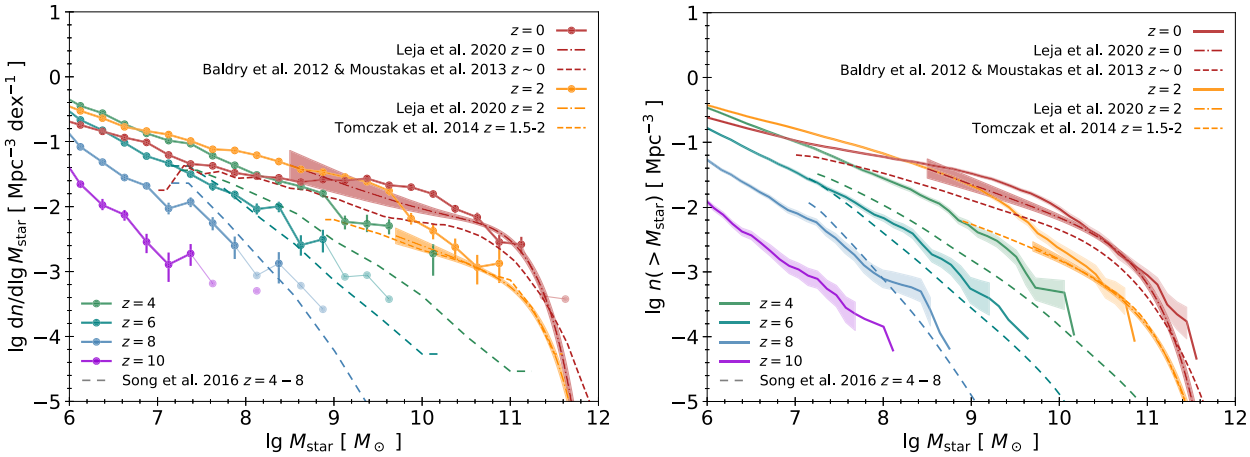

Figure 9. SMF predicted by FIREbox for $z = 0$–10 and a comparison with observational estimates. In the left-hand panel (right-hand panel), circles (solid lines) show the differential (cumulative) SMF of all galaxies with $M_{star} > 10^6\,M_\odot$ in the simulation volume. The abundance of galaxies is re-weighted to account for cosmic variance in the HMF, see Appendix A. Uncertainties (16–84 per cent) of the differential and cumulative SMFs are calculated via bootstrapping and shown by error bars (left-hand panel) or shaded regions (right-hand panel). Light shaded symbols without error bars indicate bins containing fewer than four galaxies. The panels also show observational estimates of the SMF at various redshifts (Baldry et al. 2012; Moustakas et al. 2013; Tomczak et al. 2014; Song et al. 2016; Leja et al. 2020). FIREbox predicts a SMF at $z = 0$ similar to recent estimates by Leja et al. (2020) based on non-parametric modelling except for a moderate excess at both low and high stellar masses. The $z = 0$ SMF is generally higher than those based on more traditional stellar mass estimates (e.g. Baldry et al. 2012; Moustakas et al. 2013). FIREbox struggles in reproducing the differential SMF in galaxies with $M_{star} \sim 10^{8.5} - 10^{10}\,M_\odot$ at $z \leq 4$ as a result of limited numerical convergence (see text). Interestingly, FIREbox predicts a drop in the SMF at high masses at low z, even though AGN feedback is not included.

(Gallazzi et al. 2005; Kirby et al. 2013), except perhaps at the lowest masses ($M_{star} < 10^8\,M_\odot$). This overall behaviour is consistent with the results of FIRE-2 zoom-in simulations (Gandhi et al. 2022). The relation between iron abundance and stellar mass follows the same general trend, as the MZR and can also be approximated well by a broken linear function (equation 2 with $y = 12 + \lg(\langle \mathrm{Fe/H} \rangle)$), see Table 2 for the best-fitting parameters. At low stellar masses, the slope is sub-linear and slightly smaller (0.53 for the 3 kpc aperture radius) than the slope of the MZR. The latter is expected given that the stellar metallicity relation is effectively a convolution of the MZR and the stellar growth history. The stellar metallicity relation significantly flattens (slope 0.13) in massive galaxies, similar to the MZR.

Interestingly, FIREbox predicts a much smaller scatter in stellar metallicities at given stellar mass than reported in the observational study by Gallazzi et al. (2005). The authors of the latter study point out that their high scatter may reflect, at least partly, the high observational uncertainties in measuring stellar metallicities. In fact, the stellar mass–stellar metallicity relation predicted by our simulation is even tighter than the MZR with a scatter of less than 0.05 in $M_{star} > 10^{10.5}\,M_\odot$ galaxies. We speculate that this lower scatter is a consequence of the stellar metallicity being a (SFR weighted) time-average of the gas phase metallicity.

3.6 Galaxy stellar mass functions

The SMF of galaxies provides an important point of comparison to observational data for galaxy formation simulations. Here, we use observational data spanning $z = 0$–8 (Baldry et al. 2012; Moustakas et al. 2013; Tomczak et al. 2014; Song et al. 2016), as provided by Behroozi et al. (2019). In addition, we compare with SMF estimates from the recent work by Leja et al. (2020). All data are converted (if necessary) to a Chabrier (2003) IMF.

The realized HMF in FIREbox differs from the true HMF because of the finite box size and limited numerical resolution. Similarly, the realized SMF in FIREbox differs from the SMF that would be obtained if the exact same physical model were applied to an infinitely large cosmological volume. This 'cosmic variance' can become large for small simulated volumes, e.g. the stellar mass density may vary by ∼0.2 dex for a random selection of initial conditions of a $L = 35.5$ Mpc box (Genel et al. 2014). The initial conditions for FIREbox were selected with the objective to reduce the difference between the realized and true HMF as a first mitigation measure, see Section 2.1. In addition, we calculate SMFs and other number-density-based quantities via a re-weighting approach (Appendix A). The latter increases (decreases) the contribution from galaxies in haloes that are underabundant (overabundant) relative to a reference HMF, here Behroozi, Wechsler & Conroy (2013). To reduce biases of the HMF arising from baryonic effects, we match halo masses in FIREbox with those of the corresponding collisionless simulation FIREbox^{DM} based on cumulative abundances. The main caveat of our re-weighting approach is its reliance on halo mass alone. In its present form, the re-weighting does not correct for secondary trends, e.g. with large-scale environment, halo concentration, or formation time, which have been shown to correlate non-trivially with galaxy properties (e.g. Matthee et al. 2017; Feldmann, Faucher-Giguère & Kereš 2019). Our approach differs from methods to constrain SMFs from observational data (e.g. Efstathiou, Ellis & Peterson 1988; Weigel, Schawinski & Bruderer 2016) in that it aims to correct for variations in halo abundance instead of limits in stellar mass or luminosity.

Fig. 9 shows both the differential and the cumulative SMF in FIREbox for $z = 0$–10. At $z \geq 6$, the shape and normalization of the SMF in FIREbox agrees reasonably well with observations. The low-mass slope of the simulated SMF decreases with decreasing redshift in qualitative agreement with Song et al. (2016). At $z \leq 4$, the SMF in FIREbox is higher than observed, especially for galaxies of $M_{star} \sim 10^9$–$10^{10}\,M_\odot$. A similar, but weaker, behaviour has been reported in previous semi-analytic models and hydrodynamical simulations (e.g. Vogelsberger et al. 2014; Somerville, Popping & Trager 2015). At low redshift, FIREbox overpredicts the abundance (or stellar masses) compared with traditional SMF estimates (Baldry et al. 2012; Moustakas et al. 2013) but is in much better agreement with recent studies in which stellar masses are inferred from a non-

Downloaded from https://academic.oup.com/mnras/article/522/3/3831/7140530 by Northwestern University School of Law user on 03 July 2023

parametric modelling of the star formation histories of galaxies (Leja et al. 2020), especially for MW analogs with $M_{\rm star} \sim 10^{10.5}\,M_\odot$. We note that FIREbox simulations are not tuned to reproduce any of the SMFs, in contrast with most other cosmological simulation suites (e.g. Vogelsberger et al. 2014; Schaye et al. 2015; Pillepich et al. 2018b), i.e. our results are predictions directly based on the FIRE-2 physics model.

We re-iterate two main areas of disagreement in Fig. 9. First, at low-to-intermediate stellar masses ($M_{\rm star} \sim 10^{8.5}$–$10^{10}\,M_\odot$), FIREbox overestimates the observed SMF at $z \leq 4$. A comparison with high resolution ($m_{\rm b} < 10^4\,M_\odot$) FIRE zoom-in simulations shows that galaxies in moderately low-mass ($M_{\rm halo} \sim 10^{11}\,M_\odot$) haloes have lower stellar masses at increased numerical resolution, see Appendix B. Unfortunately, this implies that the stellar masses of such galaxies are not converged at the resolution of FIREbox.

Secondly, at high stellar masses, FIREbox appears to overpredict galaxy abundances. Here, the stellar masses are converged, see Appendix B. Given that FIREbox does not include AGN feedback, a mismatch at the massive end is not unexpected. However, the shape of the simulated SMF at the massive end ($M_{\rm star} > 10^{10.5}$) may still be marginally consistent with the observations by Leja et al. (2020) if we account for the low numbers of massive galaxies in FIREbox and the associated large statistical errors. At low z, the SMF in FIREbox shows a turn-over, above which the SMF drops quickly with increasing mass. This behaviour is qualitatively similar to observations but the turn-over occurs at a lower stellar mass ($M_{\rm star} \sim 10^{10}\,M_\odot$) in FIREbox. Hence, while galaxy quenching by AGN feedback may be needed to reproduce the exact position and shape of the SMF at the high-mass end, it may not be the primary reason that the SMF shows a break. We discuss the physical origin of this turn-over in more detail in the next section.

Finally, FIREbox suggests that the SMF decreases by up to ∼0.3 dex with decreasing redshift at the lowest stellar masses ($M_{\rm star} < 10^9\,M_\odot$) between $z = 2$ and $z = 0$, which is qualitatively similar to the behaviour of the low-mass end of the HMF over this redshift range. Whether this trend is consistent with observations is currently not known given that $M_{\rm star} \sim 10^9\,M_\odot$ is close to the mass completeness limit of galaxy surveys exploring the SMF at $z = 1$–2 (Tomczak et al. 2014; Leja et al. 2020). Also, semi-empirical models do not necessarily predict this trend (Behroozi et al. 2019). Future, deeper observations may be required to test this prediction of our model.

3.7 Stellar mass–halo mass relation

The galaxy SHMR is closely related to the SMF. The latter can be obtained from the former (and vice versa) with the help of the HMF. We use this abundance matching (AM) approach (Kravtsov et al. 2004; Vale & Ostriker 2004; Behroozi, Conroy & Wechsler 2010) to calculate the SHMR from the SMFs provided by Leja et al. (2020). For simplicity of the calculation, we ignore the scatter (∼0.2 dex; Reddick et al. 2013; Zu & Mandelbaum 2015) of the SHMR. Given that FIREbox matches approximately the $z = 0$ SMF of Leja et al. (2020), we also expect a reasonable agreement with the derived SHMR. An alternative method of estimating the SHMR from observational data is empirical modelling (EM; Moster, Naab & White 2018; Behroozi et al. 2019). Here, we expect some level of disagreement, however, as these models are based on the SMFs derived from traditional SED-fitting, see discussion of Fig. 9.

The SHMR of central galaxies in FIREbox at $z = 0$ is given in Fig. 10. The ratio between galaxy stellar mass and halo mass rises quickly with increasing mass for $M_{\rm halo} < 10^{11}\,M_\odot$; it reaches a peak near $M_{\rm halo} \sim 10^{11.4}\,M_\odot$ with a maximum value ∼0.42 dex below the universal baryon fraction, and then decreases slowly towards larger masses. We obtain a qualitatively similar result if we define the galaxy radius as $R_{\rm g} = 0.1\,R_{\rm vir}$ instead of $3\,R_{\rm half}$ (not shown). However, in this case, the decline of the galaxy stellar fraction with increasing halo mass is shallower and the peak is shifted to $M_{\rm halo} \sim 10^{11.7}\,M_\odot$.

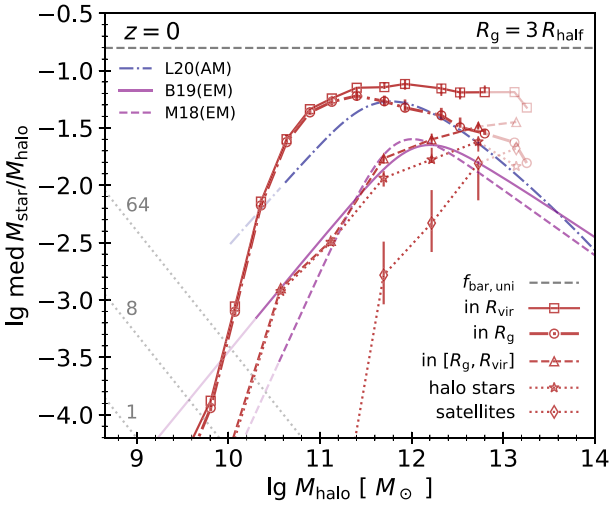

Figure 10. Median stellar mass fractions of central galaxies and their parent haloes in FIREbox at $z = 0$. Different symbols refer to different mass components in the simulation. The galaxy SHMR is shown by circles. The galaxy stellar mass is defined as the stellar mass within three times the stellar half-mass radius, see Section 2.6. Squares show the total SHMR. The galaxy and total stellar masses differ because of the stellar mass component outside the central galaxy but within the halo (triangles). The latter is further split into the stellar mass within identified sub-haloes (diamonds) and stellar mass outside identified sub-haloes (stars). Uncertainties (16–84 per cent) are calculated via bootstrapping and shown by error bars. Light shaded symbols without error bars indicate bins containing fewer than four galaxies. Grey dotted lines correspond to 1, 8, and 64 star particles of mass $m_{\rm b} = 6.3 \times 10^4\,M_\odot$ in haloes of a given mass (from bottom to top). Estimates of the galaxy SHMR via AM of the SMF by Leja et al. (2020; dot–dashed line) and via EM (Moster et al. 2018; Behroozi et al. 2019, dashed and solid lines) are also shown. Extrapolations beyond the stellar mass range of the observational data are shown by a light coloured line. The galaxy stellar fraction decreases with increasing halo mass for $M_{\rm halo} > 10^{11.5}\,M_\odot$, while the total stellar fraction scales only weakly with $M_{\rm halo}$ over the $10^{11.5–13}\,M_\odot$ mass range. The increase in the stellar mass outside massive galaxies is driven by an increasing halo star contribution and, for $M_{\rm halo} > 10^{12}\,M_\odot$, by a higher lock-up of stars in satellite galaxies.

Overall, the SHMR of FIREbox is in qualitative agreement with the AM prediction based on the Leja et al. (2020) SMF for $\sim 10^{11.5} - 10^{13}\,M_\odot$ haloes and for our fiducial choice $R_{\rm g} = 3\,R_{\rm half}$. The SHMR in FIREbox peaks at lower halo masses (by about 0.4 dex), however, and galaxies in simulated haloes with $M_{\rm halo} \sim 10^{10.5} - 10^{11.4}\,M_\odot$ have higher stellar masses (by about 0.3 dex). The latter result may partly explain the overestimate of the extra-galactic stellar component around simulated MW analogs discussed in Section 3.4 as their stellar haloes are largely built from tidally disrupted galaxies in $M_{\rm star} \sim 10^{8.5}\,M_\odot$ (i.e. $M_{\rm halo} \sim 10^{11}\,M_\odot$) haloes (Purcell, Bullock & Zentner 2007). As expected, empirical estimates (Moster et al. 2018; Behroozi et al. 2019) differ significantly from the simulation estimates with the former showing overall lower stellar masses in $M_{\rm halo} > 10^{10}\,M_\odot$ haloes.

We now further investigate the decrease of the galaxy stellar fraction in massive galaxies seen in FIREbox. A similar behaviour has been found empirically, and it is often attributed to the quenching

Downloaded from https://academic.oup.com/mnras/article/522/3/3831/7140530 by Northwestern University School of Law user on 03 July 2023

of star formation by AGN feedback (e.g. Croton et al. 2006; Martizzi, Teyssier & Moore 2012; Dubois et al. 2013; Wellons et al. 2023). Given the lack of the latter in FIREbox, there are several remaining possibilities that could explain this result. First, more massive haloes could lose a larger fraction of their gas, e.g. by stellar feedback-driven outflows, before they are converted to stars. We can discount this possibility since $10^{12}\ M_\odot$ haloes contain about 75 per cent of the universal baryon fraction, see Section 3.4. Furthermore, a more detailed study of the baryon content of FIREbox haloes (Feldmann et al. in preparation) shows that the baryon fraction of massive haloes does not strongly decrease with increasing halo mass. Secondly, more massive haloes could convert a smaller amount of the available baryons into stars potentially due to, e.g. the formation of a stable virial shock, which keeps much of baryons in a hot, dilute state (Birnboim & Dekel 2003; Kereš et al. 2005; Faucher-Giguère, Kereš & Ma 2011; Stern et al. 2020). Finally, a similar amount of baryons may be converted into stars, but the distribution of the stars could be more extended in more massive haloes, e.g. a larger fraction of the stellar mass could reside in satellite galaxies or in a stellar halo potentially build from minor and major mergers (e.g. Naab, Johansson & Ostriker 2009; Feldmann et al. 2010; Oser et al. 2010; Hilz, Naab & Ostriker 2013; Dubois et al. 2016; Rodriguez-Gomez et al. 2016).

To investigate these latter possibilities, we also show in Fig. 10, the total stellar mass in haloes, the stellar mass in satellite galaxies, and the stellar mass in halo stars (defined as stars within a halo but outside any galaxy). While the ratio between galaxy stellar mass and halo mass decreases with increasing halo mass for $M_{\rm halo} > 10^{11.5}\ M_\odot$, the stellar mass within the halo (total stellar mass) is an approximately constant fraction of the halo mass over the $M_{\rm halo} = 10^{11.5}$–$10^{12.5}\ M_\odot$ regime, with a potentially weak decline at the highest halo masses. Hence, we can largely exclude the second possibility mentioned above and conclude that a change in the spatial distribution of the stellar component, rather than a change in the baryonic conversion efficiency, drives the high-mass turn-over in the SMFs seen in Fig. 9 and the reduction of the galaxy stellar fraction in massive haloes seen in Fig. 10.

Taking a closer look, we see that stars that do not belong to identified sub-haloes ('halo stars') make up the majority of the stellar mass outside of centrals in $M_{\rm halo} \lesssim 10^{12}\ M_\odot$ haloes. In more massive haloes, stars locked up in satellite galaxies also contribute at a significant level. For MW-like systems ($M_{\rm halo} \sim 10^{12}\ M_\odot$), FIREbox predicts that the ratio between the stellar mass outside the central galaxy and the galaxy stellar mass is $\sim 0.45 \pm 0.05$ (if $R_{\rm g} = 3\ R_{\rm half}$) and $\sim 0.13 \pm 0.03$ (if $R_{\rm g} = 0.1\ R_{\rm vir}$), i.e. a sizable, but definition-dependent fraction of the total stellar mass resides outside central galaxies. A similar conclusion was reached by Pillepich et al. (2014), who analysed the stellar mass outside galaxies for a set of cosmological volume (Vogelsberger et al. 2014) and zoom-in (Guedes et al. 2011; Marinacci, Pakmor & Springel 2014) simulations using $R_{\rm g} = 2\ R_{\rm half}$. They reported ratios ranging from $\sim$0.1 to 0.6, depending on the simulation suite, for MW-like haloes, similar to our findings. We conclude that the decrease of the galaxy stellar fraction with increasing halo mass in FIREbox is driven primarily by an increasing contribution of a smooth halo star component and, at the highest masses, by a higher amount of stars in satellite galaxies.

3.8 Galaxy sizes

The sizes of FIREbox galaxies are presented in Rohr et al. (2022). At $z = 0$, the stellar half-mass radii of FIREbox galaxies with $M_{\rm star} \sim 10^{9.5-10.5}\ M_\odot$ are $\sim$3–5 kpc, in a broad agreement with effective radii of observed galaxies (e.g. Mowla et al. 2019; Nedkova et al. 2021). In contrast, massive galaxies ($M_{\rm star} > 10^{11}\ M_\odot$) in FIREbox are more compact (by $\sim$0.2–0.3 dex) possibly because of the lack of AGN feedback, while low-mass galaxies tend to have larger sizes (by $\sim$0.3 dex) than observed. The agreement with observations is better at $z = 2$, when low-mass galaxies ($< 10^{9.5}\ M_\odot$) have sizes similar to those of observed star-forming galaxies (Mowla et al. 2019; Nedkova et al. 2021), while more massive FIREbox galaxies ($> 10^{10}\ M_\odot$) have typical sizes falling between those of observed star-forming and quiescent galaxies. We caution that various systematics affect this preliminary comparison with observations (see e.g. Genel et al. 2018). A more robust analysis that calculates the sizes of FIREbox galaxies via mock observations, as well as a more systematic exploration of galaxy morphology, is left for future work.

4 COSMIC EVOLUTION OF GAS, STARS, AND STAR FORMATION

A major achievement of observational efforts with the Hubble and Spitzer Space Telescopes, as well as ground-based instruments, has been to map out the cosmic star formation history (CSFH) and stellar mass build-up from the Cosmic Dawn to the present time (Lilly et al. 1996; Madau et al. 1996; Hopkins & Beacom 2006; Madau & Dickinson 2014; Bouwens et al. 2015). In addition, observations of the neutral and molecular hydrogen content have made it possible to study how star formation in galaxies is fuelled (see e.g. Walter et al. 2020). Clearly, these observations provide an important point of comparison for galaxy models. In this section, we compare the evolution of the cosmic density of SFR, stellar mass, and atomic and molecular gas in FIREbox to observational data to further validate and explore the limitations of, the FIRE-2 physics model.

4.1 Cosmic star formation history and stellar mass

Fig. 11 analyses the CSFH and the cosmic stellar growth history (CSGH) in FIREbox. Specifically, it plots the volume-averaged SFR density and the stellar mass density as a function of redshift both for all identified galaxies in the simulation volume and for sub-sets of galaxies based on their stellar mass. Stellar masses and SFRs of galaxies are measured within $R_{\rm g} = 3\ R_{\rm half}$. SFRs are averaged over the past 20 Myr. The abundances of simulated galaxies are re-weighted based on their halo masses as described in Appendix A. We use a Locally Weighted Scatterplot Smoothing approach (Cleveland 1979) to reduce the noise in our predictions for the CSFH and CSGH.

When analysing the CSFH and CSGH for galaxies of different stellar masses, we find that cosmic star formation and stellar mass are dominated by low-mass galaxies at high z ($M_{\rm star} < 10^8\ M_\odot$ at $z > 7$). With decreasing z, more massive galaxies take over as main contributors. Since Cosmic Noon, galaxies with $10^{10}\ M_\odot < M_{\rm star} < 10^{11}\ M_\odot$ dominate both the CSFH and the CSGH.

We can compare the prediction of our simulation with the compilation of observational data by Madau & Dickinson (2014). We take the data as are except that we adjust stellar masses and SFRs for the assumption of a Chabrier (2003) IMF using the conversion factors provided by authors. The observational data only include sufficiently luminous galaxies ($L > 0.03 L_*$), which corresponds to a stellar mass threshold of approximately $M_{\rm star,\,lim} = 10^{9.3}\ M_\odot$ over $z = 0$–3 (Madau & Dickinson 2014).

Downloaded from https://academic.oup.com/mnras/article/522/3/3831/7140530 by Northwestern University School of Law user on 03 July 2023

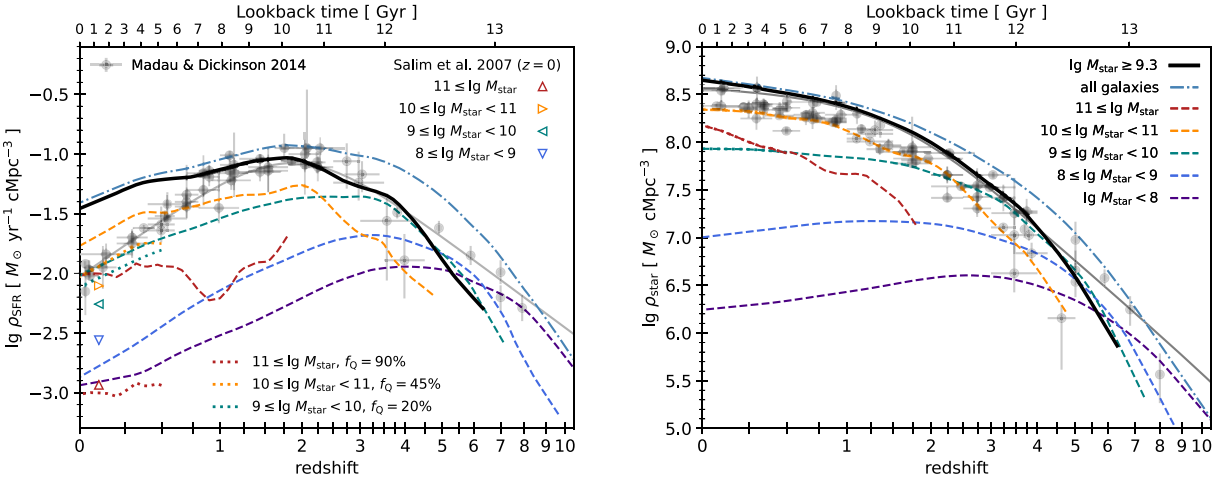

Figure 11. CSFH (left-hand panel) and CSGH (right-hand panel) in FIREbox. Blue dot–dashed lines show the CSFH and CSGH of all identified galaxies in the simulation volume, while black solid lines correspond to the case when low-mass galaxies with lg $M_{\rm star}/M_\odot < 9.3$ are excluded. SFRs of simulated galaxies are averaged over the past 20 Myr. The abundance of galaxies is re-weighted to account for cosmic variance in the HMF, see Appendix A. Dashed lines show the contributions of galaxies in various stellar mass ranges (see legend). Triangles are observational estimates of the cosmic SFR density at $z \sim 0.1$ for the same stellar mass ranges (Salim et al. 2007). Grey symbols and lines refer to an observational compilation by Madau & Dickinson (2014). The grey line on the right-hand panel is the integral of the CSFR reduced by an effective stellar mass loss of 27 per cent. The observational data are converted to a Chabrier IMF using the conversion factors of Madau & Dickinson (2014). The observational estimates of the CSFH and CSGH include galaxies above a luminosity threshold of $0.03L_*$, which corresponds approximately to a mass threshold of lg $M_{\rm star}/M_\odot \sim 9.3$ at $z = 0$–3. The CSFH in FIREbox is in good agreement with observations at $z \sim 1.5$–4.5. At $z < 1$, massive, low z galaxies often do not efficiently quench their star formation, resulting in an overestimation of the CSFH possibly as a result of the lack of AGN feedback in FIREbox. Excluding a fraction $f_{\rm Q}$ of quenched galaxies (Behroozi et al. 2019) by hand (dotted lines) results in much better agreement with the observational estimate (triangles). Intermediate mass galaxies ($9 \leq$ lg $M_{\rm star}/M_\odot < 10$, teal-colored dashed line) dominate the CSFH and CSGH at $z = 3$–5, and galaxies with $10 \leq$ lg $M_{\rm star}/M_\odot < 11$ (orange dashed line) at $z \lesssim 2$. In contrast, most of the star formation and stellar mass build-up during the EoR takes place in galaxies with low stellar masses (lg $M_{\rm star}/M_\odot < 8$, purple line) and low SFRs ($<0.03\ M_\odot\ {\rm yr}^{-1}$).

We integrate the fit to the CSFH reported by Madau & Dickinson (2014) to obtain the corresponding average CSGH as follows:

$$\rho_{\rm star}(t) = [1 - R_{\rm eff}(t)] \int_0^t \rho_{\rm SFR}(t'){\rm d}t', \quad (3)$$

where $R_{\rm eff} = 0.27$ is the effective mass return fraction,[7] which depends not only on the IMF but also on lg $M_{\rm star,lim}$.

Comparing the simulation predictions (thick black line) and observations (thin grey line) in Fig. 11, we find excellent agreement over $z \sim 1.5$–4.5. Measuring stellar masses and SFRs not within $R_{\rm g}$ but within virial radii increases the CSFH and CSGH by about 0.13 and 0.18 dex. At higher redshifts, the CSFH and CSGH of $M_{\rm star,\,lim} > 10^{9.3}\ M_\odot$ galaxies falls short of the observational data. Here, however, the assumed equivalence between $L = 0.03L_*$ and $M_{\rm star,\,lim} > 10^{9.3}$ likely does not hold given the younger stellar ages and lower metallicities of high z galaxies. Generally, the inferred CSFH (or CSGH) decreases much faster with increasing z when galaxies with low stellar masses (here lg $M_{\rm star} < 10^{9.3}\ M_\odot$) are excluded given their increased contribution to the total CSFH and CSGH at higher z. We defer a detailed analysis of the high redshift properties of FIREbox galaxies to future work. At $z \lesssim 0.7$, the CSFH in FIREbox differs noticeably from observational data. At $z = 0$, the predicted SFR density exceeds observations by ∼0.5 dex, while the stellar density is too high by ∼0.1–0.2 dex.

To understand the origin of this discrepancy at low z, we separate the FIREbox sample into various stellar mass bins and calculate their contribution to the cosmic SFR density. We compare the simulation data with observational estimates of the cosmic SFR density (Brinchmann et al. 2004; Juneau et al. 2005; Salim et al. 2007). In the following, we specifically compare with the work by Salim et al. (2007), but we found similar results when using the data by Brinchmann et al. (2004). The SFR density in low-mass galaxies is in approximate agreement with observations. Specifically, FIREbox predicts a contribution of $10^8\ M_\odot \leq M_{\rm star} < 10^9\ M_\odot$ galaxies that is about 0.25 dex lower than observed and a contribution from galaxies of intermediate mass ($10^9\ M_\odot \leq M_{\rm star} < 10^{10}\ M_\odot$) is about 0.3 dex higher than observed. In contrast, massive galaxies ($10^{10}\ M_\odot \leq M_{\rm star} < 10^{11}\ M_\odot$ and $10^{11}\ M_\odot \leq M_{\rm star}$) in FIREbox contribute at much higher levels to the cosmic SFR than found observationally (∼0.5 and ∼1 dex). Massive galaxies thus appear primarily responsible for the high cosmic SFR at low z, presumably because of the lack of AGN feedback in FIREbox.

To test whether the low quenched fraction in FIREbox can explain the high cosmic SFR, we reduce the cosmic SFR in each stellar mass bin by the expected fraction $f_{\rm Q}$ of quenched galaxies given by Behroozi et al. (2019). Specifically, we use $f_{\rm Q} = 20$ per cent, 45 per cent, and 90 per cent for the stellar mass bins of $10^9\ M_\odot \leq M_{\rm star} < 10^{10}\ M_\odot$, $10^{10}\ M_\odot \leq M_{\rm star} < 10^{11}\ M_\odot$, and $10^{11}\ M_\odot \leq M_{\rm star}$. As shown in Fig. 11, a reduction by $f_{\rm Q}$ brings the simulation predictions in much better agreement with observations.

Even though FIREbox underestimates the fraction of massive, quenched galaxies at low z, the properties of star-forming galaxies

[7]This value was adopted by Madau & Dickinson (2014) based on the asymptotic mass return fraction R of a Salpeter (1955) IMF. However, $R_{\rm eff}$ generally differs from R. In FIREbox, $R_{\rm eff}(z) \sim 0.35$–$0.11z$ holds for $z = 0$–6 if lg $M_{\rm star,lim} = 10^{9.3}\ M_\odot$ is adopted. Given that $R_{\rm eff}$ evolves with z in a mass threshold dependent manner, we adopt a constant value $R_{\rm eff} = 0.27$ for simplicity. For a non-zero mass threshold, $R_{\rm eff}$ can become smaller than zero (i.e. $1 - R_{\rm eff} > 1$) at high z. The reason being that galaxies with masses below the threshold never contribute to $\rho_{\rm SFR}$, but the stellar mass they form is included in $\rho_{\rm star}$ once the masses of their descendants exceed the threshold.

Downloaded from https://academic.oup.com/mnras/article/522/3/3831/7140530 by Northwestern University School of Law user on 03 July 2023

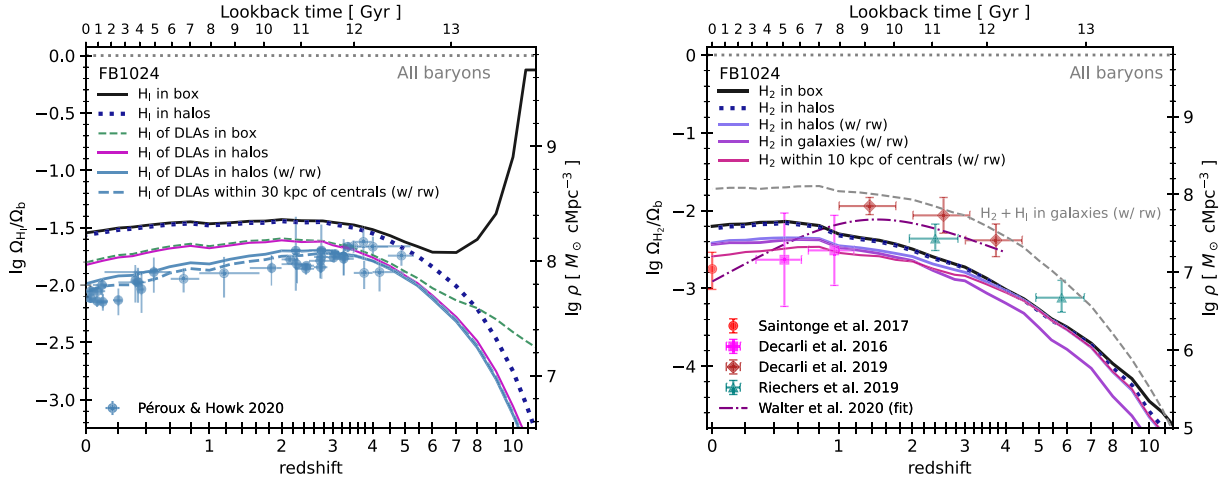

Figure 12. Cosmic evolution of the mass fractions of atomic and molecular hydrogen in FIREbox. (Left-hand panel) The mass fraction of atomic hydrogen (H_I) in the simulation volume is shown by a black solid line. This mass fraction decreases from the beginning of re-ionization ($z \sim 11$) until $z \sim 7$. Between $z \sim 4$ and $z = 0$ the fraction in H_I in FIREbox remains approximately constant. At those times, the vast majority of atomic gas resides in DM haloes (blue dotted line). A green dashed line shows the fraction of H_I with column densities above 2×10^{20} cm^{-2} (damped Lyman-α absorbers, DLAs). At high redshift ($z > 6$), DLAs can also be found outside the virial radii of DM haloes identified in FIREbox. The cosmic H_I density in DLAs peaks around $z \sim 2$–3. Blue and pink solid lines show the mass fraction of atomic hydrogen in DM haloes attributable to DLAs with and without re-weighting ('rw') by halo abundance, see Appendix A. The blue dashed line shows the H_I mass in DLAs within a 30 proper kpc radius around central galaxies. Also included in the panel are a compilation of observational data (Noterdaeme et al. 2009, 2012a; Delhaize et al. 2013; Rhee et al. 2013; Zafar et al. 2013; Crighton et al. 2015; Hoppmann et al. 2015; Rhee et al. 2016; Sánchez-Ramírez et al. 2016; Rao et al. 2017; Jones et al. 2018; Rhee et al. 2018; Bera et al. 2019; Hu et al. 2019) by Peroux & Howk (2020). Observational estimates for $z > 0.4$ were obtained via absorption spectroscopy and are thus typically limited to atomic hydrogen in DLAs. Simulations and observations agree well at those redshifts. (Right-hand panel) The mass fraction of molecular hydrogen (H_2) in the simulation volume is shown by a black solid line. Other lines show the H_2 mass fraction in haloes, in galaxies (here understood as the molecular hydrogen within a sphere of radius 0.1 R_{vir} located at the (sub-)halo centre), and within 10 kpc of central galaxies, with and without re-weighting, see legend. The figure further includes observational estimates (Decarli et al. 2016; Saintonge et al. 2017; Decarli et al. 2019; Riechers et al. 2019) based on carbon-monoxide (CO) line emission with a CO-to-H_2 conversion factor $\alpha_{CO} = 3.6\,M_\odot$ (K km s^{-1} pc^2)$^{-1}$. The cosmic H_2 mass fraction in FIREbox increases from early times until $z \sim 1$ in agreement with observations but does not decline steeply at later times as observations may imply. Mass fractions are reported in units of the cosmic baryonic density ($\rho_{bar,\,uni} \sim 6.2 \times 10^9\,M_\odot$ cMpc^{-3} for our adopted cosmology; left y-axis) or in solar masses per comoving Mpc^3 (right y-axis).

themselves appear well reproduced (see Section 3). Hence, we can infer that the physical mechanism(s) responsible for quenching of star formation should not affect the galaxy scaling relations (e.g. the molecular gas sequence or the MZRs) of the population of star-forming galaxies too severely. Furthermore, going back in time, we see that the stellar feedback model in FIREbox explains well the evolution of the average SFR and stellar mass density at $z \gtrsim 1$–5. In other words, FIREbox does not leave much room for AGN feedback to affect the CSFH and CSGH at early cosmic times. Instead, the role of AGN feedback at $z > 1$ may be to turn quiescent galaxies with low, but non-zero sSFRs into the truly passively evolving galaxies observed at those redshifts (Kriek et al. 2006; Straatman et al. 2016).

4.2 Cosmic gas density

The evolution of the cosmic gas density is connected to the evolution of the cosmic SFR and stellar mass density. On the one hand, a larger fraction of the overall baryonic mass gets locked up in stars with increasing cosmic time, thus reducing the total gas density in the Universe. On the other hand, stellar feedback, a natural by-product of star formation, strongly affects the properties of the cosmic gas, in particular the abundance of atomic and molecular hydrogen.

Several previous FIRE studies analysed the H_I content within the zoom-in regions around individual galaxies but did not fully sample the intergalactic medium (e.g. Faucher-Giguère et al. 2015, 2016; Hafen et al. 2017; Stern et al. 2021a). With FIREbox, we can more rigorously quantify the integrated neutral hydrogen mass and column density distribution across cosmic history. Caveats include the simplified modelling of local shielding of UV/ionizing photons in FIRE (Hopkins et al. 2018) and the dependence of our results on the chosen UV background, here Faucher-Giguère et al. (2009).

The left-hand panel of Fig. 12 compares the evolution of the cosmic H_I mass density in FIREbox with observational data compiled by Peroux & Howk (2020). Given the challenge in detecting the 21 cm hyperfine transition emission line of atomic hydrogen beyond $z \sim 0.4$, the evolution of the H_I mass fraction at higher z is primarily constrained by absorption spectroscopy of high column density systems, specifically Damped Lyman-α systems (DLAs). To ease the comparison, Fig. 12 thus reports the mass density of atomic hydrogen in FIREbox both restricted to DLAs (i.e. only counting H_I with column densities above 2×10^{20} cm^{-2}) as well as the overall amount. To this end, we estimate the column density of atomic hydrogen for each gas particle as $N_{H_I} = \Sigma_{gas} f_{H_I} X / m_H$, with Σ_{gas} calculated as described in Section 2.2.

As the figure shows, the cosmic H_I density in DLAs predicted by FIREbox is in good agreement with observational data once we re-weight the halo abundance to account for the finite box size. In particular, we find that the atomic hydrogen density of DLAs associated with haloes changes by a factor ~2 between $z \sim 3$ and 4 and today's Universe. About 2–4 per cent of the cosmic baryon density Ω_b is in atomic hydrogen at $z < 4$. A comparison with Fig. 11 reveals that the mass in stars exceeds the mass in atomic hydrogen at $z \lesssim 1.5$–2 in agreement with observational estimates (Driver et al. 2018).

Comparing the total amount of atomic hydrogen in FIREbox (solid black line) with the H_I contribution by DLAs (dashed green

Downloaded from https://academic.oup.com/mnras/article/522/3/3831/7140530 by Northwestern University School of Law user on 03 July 2023

line), we see that out to at least $z \sim 5$ the majority of the cosmic H_I mass (50–65 per cent) is associated with DLAs (Wolfe et al. 1986; Lanzetta et al. 1991). The remaining fraction of atomic hydrogen ($\sim 35 - 50$ per cent) is significantly higher than the 10–20 per cent contribution expected from sub-DLAs (10^{19} cm^{-2} < $N_{H_I} < 2 \times 10^{20}$ cm^{-2}) at those redshifts (Peroux et al. 2005; Zafar et al. 2013; Berg et al. 2019). This suggests that atomic hydrogen with low column densities ($N_{H_I} < 10^{19}$ cm^{-2}) contributes rather significantly to the cosmic H_I density.

The fraction of atomic hydrogen in DLAs decreases noticeably towards higher redshifts in qualitative agreement with observations (Storrie-Lombardi & Wolfe 2000). For instance, FIREbox predicts that only ~ 25 per cent of the cosmic H_I mass is hosted by DLAs at $z = 8$. While the H_I density in DLAs declines with increasing redshift at $z > 4$, an even stronger decline is seen for those DLAs that are associated with DM haloes (blue solid line) during the epoch of re-ionization (EoR; here $z \sim 6$–11). For instance, we predict that the H_I density in DLAs associated with haloes is lower by over an order of magnitude at $z = 9$ compared with $z \sim 3$. More generally, while almost all of the cosmic atomic hydrogen at $z < 5$ resides within haloes (blue dotted line), most of the atomic hydrogen at $z > 7$ can be found outside haloes, see also Villaescusa-Navarro et al. (2018). Fully accounting for atomic hydrogen, especially during the EoR, thus requires modelling the contribution outside haloes as well as from systems with column densities below those of DLAs.

The right-hand panel of Fig. 12 shows the evolution of the cosmic H_2 mass density in FIREbox. We compare our model predictions with compilations of observational data (Peroux & Howk 2020; Walter et al. 2020). Given the tight empirical correlation between molecular hydrogen and SFR (Bigiel et al. 2008; Genzel et al. 2010; Saintonge et al. 2017; Feldmann 2020), at least in the local Universe, one might expect that the evolution of the H_2 mass density mirrors the evolution of the CSFH (Decarli et al. 2019; Tacconi, Genzel & Sternberg 2020), i.e. with a peak near Cosmic Noon and a noticeably decline towards low redshift. However, this is not what we see in Fig. 12. Instead, we find that the cosmic H_2 density in FIREbox increases with cosmic time until $z \sim 1$, after which it remains approximately constant down to $z = 0$. The latter can be understood as follows. First, the typical molecular depletion time of FIREbox galaxies increases with increasing cosmic time, qualitatively similar to observations (Tacconi et al. 2020). The cosmic H_2 mass density thus increases relative to the CSFH with increasing cosmic time, i.e. more molecular gas is required at later times to sustain a given cosmic star formation activity. Secondly, the CSFH in FIREbox declines at late times somewhat less steeply than observations suggest (Fig. 11). As a consequence, the cosmic H_2 mass density in FIREbox evolves only weakly at low z.

The evolution predicted by FIREbox differs from the findings of recent observational studies (Decarli et al. 2019; Walter et al. 2020), even though it may be broadly in line with other observational measurements (Decarli et al. 2016; Saintonge et al. 2017; Riechers et al. 2019). While this difference may indicate a potential shortcoming of the FIRE physics model, we note that molecular gas plays a somewhat limited role in FIREbox given the high-density threshold of star formation (Hopkins et al. 2018). Furthermore, the neutral hydrogen density predicted by FIREbox exceeds the observed molecular density at all z, suggesting there is sufficient neutral gas in FIREbox galaxies. Therefore, another possibility is that our approximate approach of estimating molecular fractions, see Section 2.2, breaks down at higher z. However, Krumholz & Gnedin (2011) demonstrated that this approach predicts molecular fractions with an absolute error of better than 0.1 for more than 80 per cent of the ISM

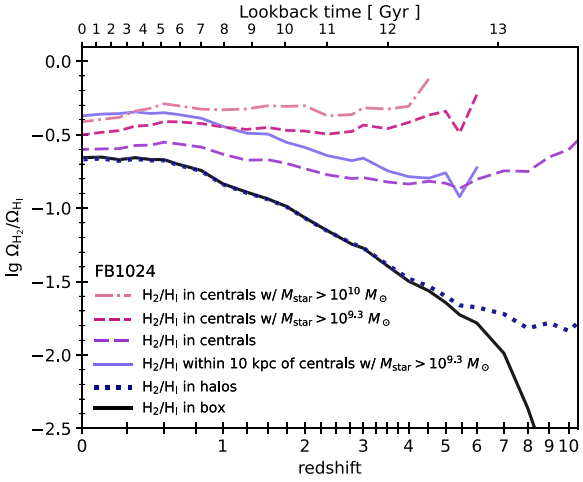

Figure 13. Evolution of the mass ratio between molecular and atomic hydrogen in FIREbox. The H_2-to-H_I ratio in the simulation volume (in DM haloes) is shown by a black solid line (a blue dotted line), while a purple solid line refers to the ratio between M_{H_2} and M_{H_I} within 10 physical kpc around central galaxies with stellar masses exceeding $10^{9.3}\ M_\odot$. The H_2-to-H_I ratio within 0.1 R_{vir} of central galaxies (central galaxies with $M_{star} > 10^{9.3}\ M_\odot$, central galaxies with $M_{star} > 10^{10}\ M_\odot$) is shown by a long-dashed purple line (short-dashed red line, dot–dashed pink line). Although the cosmic abundance of molecular hydrogen relative to atomic hydrogen decreases towards higher redshift, the H_2-to-H_I ratio in central galaxies of a given stellar mass is relatively constant across most of cosmic history when measured within 0.1 R_{vir}. In contrast, the H_2-to-H_I ratio measured in a fixed physical radius evolves more strongly with redshift. Atomic hydrogen dominates over molecular hydrogen in the ISM of all but the most massive galaxies both in the present-day Universe and at early cosmic times.

mass of galaxies with a range of stellar masses and ISM conditions when compared to a non-equilibrium radiative transfer solution.

Observational biases are yet another concern. The abundance of molecular hydrogen is typically inferred indirectly from the line luminosity of carbon-monoxide (CO) molecules or from the continuum emission of dust grains. The latter method suffers from uncertainties in the dust-to-gas ratios and dust temperatures (Scoville et al. 2014; Liang et al. 2018, 2019) and includes a contribution from atomic gas (e.g. Scoville et al. 2014), while the former approach requires knowledge of the conversion factor between CO luminosity and H_2 mass. While this conversion factor is well constrained for molecular gas in the MW (Solomon et al. 1987; Bolatto, Wolfire & Leroy 2013), it has been shown to vary significantly with galaxy properties such as metallicity and interstellar radiation field (Leroy et al. 2011; Feldmann, Gnedin & Kravtsov 2012; Bolatto et al. 2013). The conversion factor is thus a significant systematic for molecular gas estimates based on CO data, especially at higher z (Walter et al. 2020). Bringing the H_2 predicted by FIREbox at $z > 1$ in agreement with Decarli et al. (2019) and Walter et al. (2020) would require a conversion factor that is about 0.4 dex lower than the standard value for the MW. Such a reduction in the conversion factor would also help mitigating the tension between the theoretically predicted and observed molecular gas fractions in galaxies at the Cosmic Noon (Narayanan, Bothwell & Davé 2012), see also Lagos et al. (2015), Davé et al. (2017), Popping et al. (2019), and Dubois et al. (2021).

The conversion factor for high z galaxies has been empirically constrained by comparing CO emission and dynamical masses (Daddi et al. 2010). This approach tacitly assumes, however, that gas in high redshift galaxies is pre-dominantly molecular (e.g. Saintonge et al. 2013). To test this assumption, we plot in Fig. 13

Downloaded from https://academic.oup.com/mnras/article/522/3/3831/7140530 by Northwestern University School of Law user on 03 July 2023

the ratio between molecular and atomic hydrogen in FIREbox. The figure offers several insights.

First, it shows that with the possible exception of the most massive galaxies at high z, the cold gas in galaxies is never H_2 dominated. In fact, less than a third of neutral gas is in molecular form with the mass ratio between molecular and atomic hydrogen near or below 0.5. If taken at face value, this result suggests that the CO to H_2 conversion factor as inferred from dynamical masses could be significantly overestimated. Secondly, Fig. 13 shows that, when averaged over cosmic scales, the H_2-to-H_I mass ratio decreases strongly with increasing redshift. This result holds both for the gas phases in the box as well as the gas residing in DM haloes. The latter plateaus at a mass ratio of ~ 1.5 per cent at $z \gtrsim 8$, while the former continues to drop with increasing z during the EoR.

Finally, the H_2-to-H_I mass ratio within galaxies is almost independent of z. The normalization and redshift evolution of the latter depends on the mass of the selected galaxies (more massive galaxies tend to have a larger H_2-to-H_I mass ratio) as well as the radius enclosing the gas components. Calculating the mass ratio within $0.1 \times R_{\rm vir}$ results in a flatter evolution than using a radius of fixed physical size. Given that the molecular-to-neutral gas ratio depends sensitively on gas column density and metallicity, see Section 2.7; these trends in the H_2-to-H_I mass ratio are likely driven by both the spatial and the stellar mass dependence of gas densities and metallicities around galaxies.

4.3 Large-scale distribution of atomic and molecular hydrogen

The CDDF measures the number of intervening systems per unit column density N and absorption length X (Bahcall & Peebles 1969). The CDDF provides an excellent point of comparison for theoretical models given that it probes cosmic gas under a range of physical conditions and in a variety of cosmic environments (Altay et al. 2011; McQuinn, Peng Oh & Faucher-Giguère 2011; Rahmati et al. 2015; Crain et al. 2017; Balashev & Noterdaeme 2018; Szakacs et al. 2022).

At $z < 0.4$, the CDDF of atomic hydrogen is observationally accessible via its 21-cm line emission (Zwaan et al. 2005; Peroux & Howk 2020), while Lyα absorption spectroscopy of background quasars can probe the CDDF at higher redshift (e.g. Prochaska & Wolfe 2009; Noterdaeme et al. 2009, 2012b). Intervening systems include both Lyα forest absorbers with $N_{\rm H_I} < 10^{17.2}$ cm^{-2} (e.g. Rauch 1998), Lyman limit systems ($10^{17.2} \leq N_{\rm H_I}/{\rm cm}^{-2} < 10^{20.3}$, e.g. Péroux et al. 2003), and Damped Lyα systems ($N_{\rm H_I} \geq 10^{20.3}$ cm^{-2}, e.g. Wolfe, Gawiser & Prochaska 2005). Observationally, the H_I CDDF is approximately described by a single power-law over $N_{\rm H_I} \sim 10^{13} - 10^{21}$ cm^{-2} (Tytler 1987) with a break at higher column densities ($\sim 10^{20.5}$–10^{21} cm^{-2}; Péroux et al. 2003). The shape of the H_I CDDF is almost invariant with redshift and its normalization shows only a moderate change (factor 2 between $z = 4$ and $z = 2.2$) with redshift (Zwaan et al. 2005; Prochaska, Herbert-Fort & Wolfe 2005; Prochaska & Wolfe 2009).

To calculate the CDDF, we project the atomic or molecular hydrogen density in the simulation box, along a specified axis onto a 2D grid with resolution of 150 comoving pc, which is comparable to the ~100 pc resolution of the PHANGS-ALMA survey at $z = 0$ (Leroy et al. 2021b). In more detail, we use a combination of `smooth` and `tipgrid` for the deposition of the H_I and H_2 masses onto the grid.[8] First, `smooth` computes a smoothing length for every particle as half of the distance to the nth neighbour particle. We found that $n = 80$ provides a good balance between oversmoothing and too high particle noise for this application. Next, the simulation region is divided into $n_{\rm s}$ equally spaced slabs of depth $\Delta L = 15/n_{\rm s}$ cMpc h^{-1} for the chosen spatial direction. The advantage of using slices is that it reduces the chance of line-of-sight overlap between separate absorbing systems. However, we find practically little difference in the estimated CDDF over much of the column density and redshift range of interest when varying $n_{\rm s}$ between 1 and 10. In the following, we use $n_{\rm s} = 10$ but report the CDDF only if it differs by less than 5 per cent from the CDDF calculated with $n_{\rm s} = 1$. Next, `tipgrid` projects particles in the same slab onto a 2D grid by depositing the atomic or molecular hydrogen mass of each gas particle via the SPH scatter approach with a cubic spline kernel and the smoothing lengths calculated beforehand. The CDDF is then obtained from the column density distributions of the pixels of all slabs normalized to ΔX, where the absorption distance ΔX is related to the comoving slab depth ΔL via $\Delta X = \Delta L \frac{H_0}{c}(1+z)^2$.

The left-hand panel of Fig. 14 compares the CDDF of atomic hydrogen in FIREbox with a compilation of observational data over $z = 0$–5.5. Overall the agreement is good, especially at $N_{\rm H_I} < 10^{21}$ cm^{-2}. FIREbox predicts that the H_I CDDF does not strongly evolve with cosmic time in agreement with observations. FIREbox overestimates the incidence of low redshift systems with the highest column densities ($N_{\rm H_I} > 10^{21}$ cm^{-2}). However, the observational estimate for $z = 0$ assumes optical thin emission, which may result in an underestimate at the highest column densities (Zwaan et al. 2005).

The right-hand panel of Fig. 14 shows our prediction for the CDDF of molecular hydrogen (H_2) and compares it with observational data (Zwaan & Prochaska 2006; Balashev & Noterdaeme 2018; Leroy et al. 2021b; Szakacs et al. 2022). The H_2 CDDF is in broad agreement with the observations at $z = 3$ but shows some differences at low z, in particular a steeper decrease with increasing column density for large $N_{\rm H_2}$ and a higher normalization at low column densities. In contrast to the H_I CDDF, the normalization of the H_2 CDDF shows a noticeable dependence on redshift, increasing by over one order of magnitude from $z = 6$ to $z = 2$ at all column densities, reflecting the overall increase in the cosmic molecular gas density (Peroux & Howk 2020), see also Fig. 12. Between $z = 2$ and $z = 0$, the H_2 CDDF slightly decreases at the highest column densities ($N_{\rm H_2} \gtrsim 10^{22}$ cm^{-2}) and increases at lower column densities, leading to a change in its shape. While the H_2 CDDF is 'bottom-light' compared with the H_I CDDF, it increases monotonically with decreasing column densities down to at least $N_{\rm H_2} \sim 10^{16}$ cm^{-2}, i.e. there is no indication of a turn-over in the H_2 CDDF as seen in the observational study of Szakacs et al. (2022) presumably due to sensitivity and incompleteness limits.

5 SUMMARY AND CONCLUSIONS

We have introduced the FIREbox suite, a set of galaxy formation simulations in a cosmological volume ($L = 22.1$ cMpc) run down to $z = 0$ with the GIZMO gravity-hydrodynamics solver in mesh-less hydrodynamics mode (Hopkins 2015) and with the FIRE-2 physics model (Hopkins et al. 2018). The FIREbox volume contains about 20–30 MW analogs, as well as over a thousand lower mass galaxies, enabling the study of representative samples of highly resolved galaxies. The main simulation analysed in this paper (FIREbox) has a baryonic mass resolution of $m_{\rm b} \sim 6.3 \times 10^4\, M_\odot$ and a spatial resolution of ~20 pc in dense interstellar gas, comparable to state-of-the-art zoom-in simulations. The high numerical resolution combined with the fully cosmological setting results in an unprecedented dynamic range ($\gtrsim 10^6$) for a galaxy formation simulation. FIREbox is able

[8] https://github.com/N-BodyShop/smooth

Downloaded from https://academic.oup.com/mnras/article/522/3/3831/7140530 by Northwestern University School of Law user on 03 July 2023

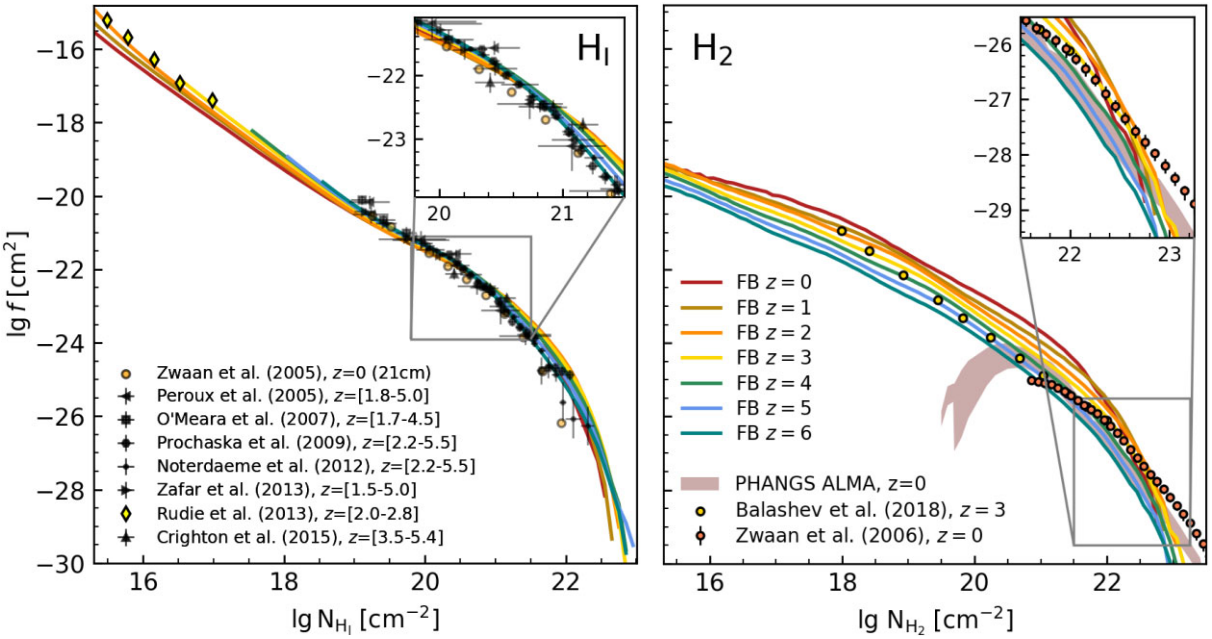

Figure 14. CDDFs (f) of atomic and molecular hydrogen in FIREbox. The CDDF $f(N, z)$ quantifies the number of intervening systems per unit path length $X(z)$ and unit column density N. (Left) The CDDF of atomic hydrogen in FIREbox reproduces well the observed H_I CDDF from quasar absorption line spectroscopy and 21-cm emission line surveys (Peroux et al. 2005; Zwaan et al. 2005; O'Meara et al. 2007; Prochaska & Wolfe 2009; Noterdaeme et al. 2012b; Rudie et al. 2013; Zafar et al. 2013; Crighton et al. 2015) but with some apparent deviations at $N_{H_I} > 10^{21}$ cm^{-2}. We note that the observational estimate for $z = 0$ assumes optical thin emission, which may not hold at high column densities (Zwaan et al. 2005). (Right) The CDDF of molecular hydrogen in FIREbox and observational estimates by PHANGS (Szakacs et al. 2022), Zwaan & Prochaska (2006), and Balashev & Noterdaeme (2018). In agreement with the literature, the H_I CDDF does not strongly evolve with cosmic time. In contrast, the H_2 CDDF at $N_{H_2} \leq 10^{22}$ cm^{-2} increases by more than one order of magnitude between $z = 6$ and $z = 0$.

to capture simultaneously the multiphase structure of the ISM in galaxies and the impact of baryonic physics on cosmological scales. Importantly, FIREbox is not tuned to specific observational data, such as the SMF, but rather it implements comparably well-understood physical processes in a self-consistent fashion without adjusting model parameters. As such it provides a true prediction of galaxy formation theory in a ΛCDM Universe. Modelled baryonic processes include gas cooling, star formation, stellar winds, supernova feedback, and radiative feedback (photoionization, photoelectric heating, and radiation pressure). Feedback from AGNs is currently not included.

In this work, we have focused on validating our methodology by comparing basic predictions of FIREbox with observational data across cosmic time. Specifically, we have analysed various fundamental galaxy scaling relations, as well as the cosmic evolution of gas masses, stellar masses, and SFRs, highlighting successes and failures of the FIRE-2 model. Future studies based on FIREbox will discuss, e.g. the morphologies of the simulated galaxies, their SFRs and depletion times, and the link between galaxy and halo formation. Our main findings are as follows:

(i) FIREbox predicts average SFRs of star-forming galaxies in good agreement with observations both at $z = 0$ and $z = 2$ (Fig. 5). The slope of the star-forming sequence is slightly sub-linear at $z = 0$ (∼0.85) and near linear at $z = 2$ (∼0.95).

(ii) FIREbox underestimates the presence of massive, quiescent galaxies at low z (Fig. 6). While FIREbox naturally accounts for a variety of environmental and stellar feedback-driven quenching channels, additional sources, such as AGN feedback, are thus necessary to fully suppress star formation in massive galaxies at low z.

(iii) Simulated galaxies have atomic and molecular gas masses (for a given stellar mass) in good agreement with observational data at $z = 0$, see Fig. 7. According to FIREbox, these gas sequences extend down to (at least) $M_{star} \sim 10^7\ M_\odot$, and they are well described by broken power-laws over four orders of magnitude in stellar mass.

(iv) FIREbox broadly reproduces the observed MZR at $z = 0$ over many orders of magnitude both for gas phase metallicities as well as stellar metallicities, see Fig. 8. In addition, the simulation predicts a low scatter (≲0.1 dex) for both relations. Both MZRs are well fit by broken power-laws.

(v) FIREbox predicts a SMF at $z = 0$ similar to recent estimates by Leja et al. (2020) based on non-parametric modelling except for a moderate excess at both low and high stellar masses (Fig. 9). Our predicted $z = 0$ SMF is generally higher than those based on more traditional stellar mass estimates (e.g. Baldry et al. 2012; Moustakas et al. 2013). At intermediate redshifts ($z \sim 2 - 4$), FIREbox overpredicts the SMF at low-to-intermediate galaxy masses ($M_{star} \sim 10^{8.5} - 10^{10}\ M_\odot$). A comparison with FIRE-2 zoom-in simulations reveals that reaching a mass resolution of $m_b < 10^4\ M_\odot$ may be needed to sufficiently lower stellar masses in haloes of $M_{halo} \sim 10^{11}\ M_\odot$. At high $z \geq 6$, the SMF in FIREbox agrees well with estimates by Song et al. (2016).

(vi) The galaxy stellar-to-halo mass ratio in FIREbox increases with increasing halo mass at $M_{halo} < 10^{11}\ M_\odot$, peaks near $M_{halo} < 10^{11.5}\ M_\odot$, and then declines towards the massive end in qualitative agreement with empirical estimates. The FIRE-2 physics models thus predicts a peak in the galaxy baryonic conversion efficiency even without the inclusion of AGN feedback. However, as our study of the SMF highlights, the stellar masses at the massive end tend to be too high if no additional feedback sources are included, i.e. the

Downloaded from https://academic.oup.com/mnras/article/522/3/3831/7140530 by Northwestern University School of Law user on 03 July 2023

decline in the stellar mass–halo mass ratio is too shallow. The galaxy baryonic conversion efficiency reaches a peak at intermediate halo masses because the fraction of stellar mass residing outside galaxies, i.e. in a stellar halo and in satellite galaxies, increases strongly with increasing halo mass at the massive end (Fig. 10). In contrast, the ratio between the stellar mass in the halo and the halo mass declines only weakly at the massive end after peaking near $M_{\rm halo} = 10^{12}\,M_\odot$.

(vii) The haloes of MW analogs have a baryon fraction of $11.6^{+0.5}_{-0.4}$ per cent, which is only about 25 per cent lower than the universal baryon fraction. This percentage is higher than the empirical estimate of 7 per cent of detected baryons. The observationally 'missing' baryons are located in various components, including ionized gas with temperatures below 2×10^5 K and an extra-galactic stellar component.

(viii) The CSFH and the stellar mass build-up in FIREbox broadly match observational estimates at $z > 1$. At low z, FIREbox overestimates the cosmic SFR density by a factor of ∼3. This mismatch is driven to a large degree by the underprediction of the quenched fraction in FIREbox, which results in too high a star formation activity in haloes hosting $M_{\rm star} > 10^{10}\,M_\odot$ galaxies.

(ix) The cosmic H_I density is in broad agreement with observations and shows little evolution with redshift. The cosmic H_2 density increases monotonically with increasing cosmic time until $z \sim 1$ after which it remains approximately constant, see Fig. 12. The near constancy of the cosmic H_2 density at $z < 1$ is in tension with some observational data (Walter et al. 2020). This tension could be reduced if higher z galaxies have a lower H_2 mass per CO luminosity compared with MW-like galaxies in the nearby Universe.

(x) Finally, we compare the CDDFs of atomic and molecular hydrogen in FIREbox with observations finding good agreement for H_I, see Fig. 14. In contrast to the H_I CDDF, the normalization of the H_2 CDDF shows a noticeable dependence on redshift, increasing by over one order of magnitude from $z = 6$ to $z = 2$ at all column densities reflecting the overall increase in the cosmic molecular gas density (Peroux & Howk 2020).

FIREbox makes it possible to explore the predictions of the FIRE-2 physics model statistically by providing a representative sample of highly resolved galaxies across cosmic history. However, the current iteration of FIREbox should be understood as a first step in this direction with much work yet to be done. While the model is broadly successful in reproducing a number of observational constraints, we also noted various areas of tension or disagreement. In particular, FIREbox is unable to produce massive, quenched galaxies in the appropriate numbers and also predicts a cosmic SFR density that is too high at late times. It is possible that the inclusion of feedback from super-massive black holes will remedy these shortcomings (Su et al. 2021; Wellons et al. 2023). However, adding AGN feedback also increases the uncertainty of the model predictions as it introduces significant modelling degeneracies.

Additional work is also needed in both completing the accounting of the relevant processes and modelling them at the required resolution level. For instance, magnetic fields and cosmic ray pressure may affect the cloud structure on small scales (Hennebelle & Inutsuka 2019), accelerate galactic winds (Booth et al. 2013; Salem & Bryan 2014; Girichidis et al. 2016; Dashyan & Dubois 2020), or quench star formation (e.g. Su et al. 2020). Recent progress on modelling these physical processes is encouraging (e.g. Chan et al. 2019; Hopkins et al. 2020; Farcy et al. 2022) and we hope to include them in the future. FIREbox, with its focus on comparably well-understood physics, provides a robust baseline prediction for such future model extensions.

ACKNOWLEDGEMENTS

The authors thank the referee for insightful comments that helped to improve the paper. RF thanks Oliver Hahn, Marcel van Daalen, and Jose Oñorbe for help with MUSIC and CAMB. RF acknowledges financial support from the Swiss National Science Foundation (grant no. PP00P2_157591, PP00P2_194814, and 200021_188552). EQ was supported in part by a Simons Investigator grant from the Simons Foundation and NSF AST grant 2107872. CAFG was supported by NSF through grants AST-1715216, AST-2108230, and CAREER award AST-1652522; by NASA through grants 17-ATP17-006 7 and 21-ATP21-0036; by STScI through grants HST-AR-16124.001-A and HST-GO-16730.016-A; by CXO through grant TM2-23005X; and by the Research Corporation for Science Advancement through a Cottrell Scholar Award. Support for PFH was provided by NSF Research Grants 1911233, 20009234, 2108318, NSF CAREER grant 1455342, NASA grants 80NSSC18K0562, HST-AR-15800. Numerical calculations were run on the allocations AST21010 and AST20016 supported by the NSF and TACC, and NASA HEC SMD-16-7592. DK was supported by the NSF Grant AST-2108314. LB, MB, and EC acknowledge financial support from the Swiss National Science Foundation (PP00P2_194814, 200021_188552). JSB was supported by NSF grant AST-1910346. JG gratefully acknowledges financial support from the Swiss National Science Foundation (grant no CRSII5_193826). JM is funded by the Hirsch foundation. Sabbatical leave support for JM was provided by Pomona College and the Harry and Grace Steele Foundation. AW received support from NSF via CAREER award AST-2045928 and grant AST-2107772; NASA ATP grant 80NSSC20K0513; HST grants AR-15809, GO-15902, GO-16273 from STScI. We acknowledge PRACE for awarding us access to MareNostrum at the Barcelona Supercomputing Center (BSC), Spain. This research was partly carried out via the Frontera computing project at the Texas Advanced Computing Center. Frontera is made possible by National Science Foundation award OAC-1818253. This work was supported in part by a grant from the Swiss National Supercomputing Centre (CSCS) under project IDs s697 and s698. We acknowledge access to Piz Daint at the Swiss National Supercomputing Centre, Switzerland, under the University of Zurich's share with the project ID uzh18. This work made use of infrastructure services provided by S3IT (www.s3it.uzh.ch), the Service and Support for Science IT team at the University of Zurich. All plots were created with the MATPLOTLIB library for visualization with PYTHON (Hunter 2007). This research has made use of NASA's Astrophysics Data System.

DATA AVAILABILITY

The data supporting the plots within this article are available on reasonable request to the corresponding author. A public version of the GIZMO code is available at http://www.tapir.caltech.edu/~phopkins/Site/GIZMO.html. FIRE data releases are publicly available at http://flathub.flatironinstitute.org/fire.

REFERENCES

Agertz O., Kravtsov A. V., 2015, ApJ, 804, 18
Agertz O., Kravtsov A. V., Leitner S. N., Gnedin N. Y., 2013, ApJ, 770, 25
Agertz O. et al., 2021, MNRAS, 503, 5826
Altay G., Theuns T., Schaye J., Crighton N. H. M., Dalla Vecchia C., 2011, ApJ, 737, L37
Anderson M. E., Bregman J. N., 2010, ApJ, 714, 320
Anglés-Alcázar D., Faucher-Giguère C.-A., Kereš D., Hopkins P. F., Quataert E., Murray N., 2017a, MNRAS, 470, 4698

Downloaded from https://academic.oup.com/mnras/article/522/3/3831/7140530 by Northwestern University School of Law user on 03 July 2023

Anglés-Alcázar D., Faucher-Giguère C.-A., Quataert E., Hopkins P. F., Feldmann R., Torrey P., Wetzel A., Kereš D., 2017b, MNRAS, 472, L109
Applebaum E., Brooks A. M., Christensen C. R., Munshi F., Quinn T. R., Shen S., Tremmel M., 2021, ApJ, 906, 96
Asplund M., Grevesse N., Sauval a. J., Scott P., 2009, ARA&A, 47, 481
Bacchini C., Fraternali F., Iorio G., Pezzulli G., 2019a, A&A., 622, A64
Bacchini C., Fraternali F., Pezzulli G., Marasco A., Iorio G., Nipoti C., 2019b, A&A, 632, A127
Bacon R. et al., 2010, in McLean I. S., Ramsay S. K., Takami H., eds, Proc. SPIE Conf. Ser. Vol. 7735, Ground-based Airborne Instrum. Astron. III. SPIE, Bellingham, p. 773508
Baes M., Verstappen J., De Looze I., Fritz J., Saftly W., Vidal Pérez E., Stalevski M., Valcke S., 2011, ApJS, 196, 22
Bahcall J. N., Peebles P. J. E., 1969, ApJ, 156, L7
Balashev S. A., Noterdaeme P., 2018, MNRAS, 478, L7
Baldry I. K. et al., 2012, MNRAS, 421, 621
Bauer A. E. et al., 2013, MNRAS, 434, 209
Beckmann R. S. et al., 2017, MNRAS, 472, 949
Behroozi P. S., Conroy C., Wechsler R. H., 2010, ApJ, 717, 379
Behroozi P. S., Wechsler R. H., Conroy C., 2013, ApJ, 770, 57
Behroozi P., Wechsler R. H., Hearin A. P., Conroy C., 2019, MNRAS, 488, 3143
Bellovary J. M., Cleary C. E., Munshi F., Tremmel M., Christensen C. R., Brooks A., Quinn T. R., 2019, MNRAS, 482, 2913
Benincasa S. M. et al., 2020, MNRAS, 497, 3993
Bera A., Kanekar N., Chengalur J. N., Bagla J. S., 2019, ApJ, 882, L7
Berg T. A. M. et al., 2019, MNRAS, 488, 4356
Bernardini M., Feldmann R., Anglés-Alcázar D., Boylan-Kolchin M., Bullock J., Mayer L., Stadel J., 2022, MNRAS, 509, 1323
Besla G., Kallivayalil N., Hernquist L., van der Marel R. P., Cox T. J., Kereš D., 2012, MNRAS, 421, 2109
Bigiel F., Leroy A., Walter F., Brinks E., de Blok W. J. G., Madore B., Thornley M. D., 2008, AJ, 136, 2846
Birnboim Y., Dekel A., 2003, MNRAS, 345, 349
Bland-Hawthorn J., Gerhard O., 2016, ARA&A., 54, 529
Bolatto A. D., Wolfire M., Leroy A. K., 2013, ARA&A, 51, 207
Booth C. M., Agertz O., Kravtsov A. V., Gnedin N. Y., 2013, ApJ, 777, L16
Bouché N. et al., 2010, ApJ, 718, 1001
Bouwens R. J. et al., 2015, ApJ, 803, 1
Bregman J. N., Anderson M. E., Miller M. J., Hodges-Kluck E., Dai X., Li J.-T., Li Y., Qu Z., 2018, ApJ, 862, 3
Brinchmann J., Charlot S., White S. D. M., Tremonti C., Kauffmann G., Heckman T., Brinkmann J., 2004, MNRAS, 351, 1151
Brooks A. M., Governato F., Booth C. M., Willman B., Gardner J. P., Wadsley J., Stinson G., Quinn T., 2006, ApJ, 655, L17
Bryan G. L., Norman M. L., 1998, ApJ, 495, 80
Camps P., Baes M., 2015, Astron. Comput., 9, 20
Catinella B. et al., 2010, MNRAS, 403, 683
Catinella B. et al., 2018, MNRAS, 476, 875
Cattaneo a. et al., 2009, Nature, 460, 213
Cautun M. et al., 2020, MNRAS, 494, 4291
Ceverino D., Klypin A., Klimek E. S., Trujillo-Gomez S., Churchill C. W., Primack J., Dekel A., 2014, MMRAS, 442, 1545
Ceverino D., Mandelker N., Snyder G. F., Lapiner S., Dekel A., Primack J., Ginzburg O., Larkin S., 2023, MNRAS, in press
Chabrier G., 2003, PASP, 115, 763
Chan T. K., Kereš D., Wetzel A., Hopkins P. F., Faucher-Giguère C.-A., El-Badry K., Garrison-Kimmel S., Boylan-Kolchin M., 2018, MNRAS, 478, 906
Chan T. K., Kereš D., Hopkins P. F., Quataert E., Su K.-Y., Hayward C. C., Faucher-Giguère C.-A., 2019, MNRAS, 488, 3716
Chevallard J., Charlot S., 2016, MNRAS, 462, 1415
Cleveland W. S., 1979, J. Am. Stat. Assoc., 74, 829
Combes F. et al., 2012, A&A, 539, 1
Crain R. A., McCarthy I. G., Frenk C. S., Theuns T., Schaye J., 2010, MNRAS, 407, 1403
Crain R. A. et al., 2015, MNRAS, 450, 1937
Crain R. A. et al., 2017, MNRAS, 464, 4204
Crighton N. H. et al., 2015, MNRAS, 452, 217
Croton D. J. et al., 2006, MNRAS, 365, 11
Daddi E. et al., 2010, ApJ, 713, 686
Dashyan G., Dubois Y., 2020, A&A, 638, A123
Dashyan G., Silk J., Mamon G. A., Dubois Y., Hartwig T., 2018, MNRAS, 473, 5698
Davé R., Finlator K., Oppenheimer B. D., 2012, MNRAS, 421, 98
Davé R., Thompson R., Hopkins P. F., 2016, MNRAS, 462, 3265
Davé R., Rafieferantsoa M. H., Thompson R. J., Hopkins P. F., 2017, MNRAS, 467, 115
Davé R., Anglés-Alcázar D., Narayanan D., Li Q., Rafieferantsoa M. H., Appleby S., 2019, MNRAS, 486, 2827
Davé R., Crain R. A., Stevens A. R. H., Narayanan D., Saintonge A., Catinella B., Cortese L., 2020, MNRAS, 497, 146
Davies L. J. et al., 2016, MNRAS, 461, 458
Davis M., Efstathiou G., Frenk C. S., White S. D. M., 1985, ApJ, 292, 371
Deason A. J., Belokurov V., Sanders J. L., 2019, MNRAS, 490, 3426
Decarli R. et al., 2016, ApJ, 833, 69
Decarli R. et al., 2019, ApJ, 882, 138
Dekel A., Mandelker N., 2014, MNRAS, 444, 2071
Dekel A., Silk J., 1986, ApJ, 303, 39
Dekel A., Woo J., 2003, MNRAS, 344, 1131
Delhaize J., Meyer M. J., Staveley-Smith L., Boyle B. J., 2013, MNRAS, 433, 1398
Dewdney P. E., Hall P. J., Schilizzi R. T., Lazio T. J. L. W., 2009, Proc. IEEE, 97, 1482
Donnari M. et al., 2019, MNRAS, 485, 4817
Dopita M. A., Kewley L. J., Sutherland R. S., Nicholls D. C., 2016, Ap&SS, 361, 61
Driver S. P. et al., 2018, MNRAS, 475, 2891
Dubois Y., Gavazzi R., Peirani S., Silk J., 2013, MNRAS, 433, 3297
Dubois Y. et al., 2014, MNRAS, 444, 1453
Dubois Y., Peirani S., Pichon C., Devriendt J., Gavazzi R., Welker C., Volonteri M., 2016, MNRAS, 463, 3948
Dubois Y. et al., 2021, A&A, 651, A109
Efstathiou G., Ellis R. S., Peterson B. A., 1988, MNRAS, 232, 431
El-Badry K. et al., 2018, MNRAS, 473, 1930
Elbaz D. et al., 2007, A&A, 468, 33
Emsellem E. et al., 2022, A&A, 659, A191
Escala I. et al., 2018, MNRAS, 474, 2194
Fang J. J. et al., 2018, ApJ, 858, 100
Farcy M., Rosdahl J., Dubois Y., Blaizot J., Martin-Alvarez S., 2022, MNRAS, 513, 5000
Faucher-Giguère C.-A., Lidz A., Zaldarriaga M., Hernquist L., 2009, ApJ, 703, 1416
Faucher-Giguère C.-A., Kereš D., Ma C.-P., 2011, MNRAS, 417, 2982
Faucher-Giguère C.-A., Hopkins P. F., Kereš D., Muratov A. L., Quataert E., Murray N., 2015, MNRAS, 449, 987
Faucher-Giguère C.-A., Feldmann R., Quataert E., Kereš D., Hopkins P. F., Murray N., 2016, MNRAS, 461, L32
Faucher-Giguère C. A., Kereš D., Dijkstra M., Hernquist L., Zaldarriaga M., 2010, ApJ, 725, 633
Feldmann R., 2013, MNRAS, 433, 1910
Feldmann R., 2015, MNRAS, 449, 3274
Feldmann R., 2017, MNRAS, 470, L59
Feldmann R., 2020, Commun. Phys., 3, 226
Feldmann R., Mayer L., 2015, MNRAS, 446, 1939
Feldmann R., Carollo C. M., Mayer L., Renzini A., Lake G., Quinn T., Stinson G. S., Yepes G., 2010, ApJ, 709, 218
Feldmann R., Carollo C. M., Mayer L., 2011, ApJ, 736, 88
Feldmann R., Gnedin N. Y., Kravtsov A. V., 2012, ApJ, 747, 124
Feldmann R., Hooper D., Gnedin N. Y., 2013, ApJ, 763, 21
Feldmann R., Hopkins P. F., Quataert E., Faucher-Giguère C.-A., Kereš D., 2016, MNRAS, 458, L14
Feldmann R., Quataert E., Hopkins P. F., Faucher-Giguère C.-A., Kereš D., 2017, MNRAS, 470, 1050
Feldmann R., Faucher-Giguère C.-A., Kereš D., 2019, ApJ, 871, L21
Ferland G. J., Korista K. T., Verner D. A., Ferguson J. W., Kingdon J. B., Verner E. M., 1998, PASP, 110, 761
Finlator K., Davé R., 2008, MNRAS, 385, 2181

Downloaded from https://academic.oup.com/mnras/article/522/3/3831/7140530 by Northwestern University School of Law user on 03 July 2023

Fitts A. et al., 2017, MNRAS, 471, 3547
Flores Velázquez J. A. et al., 2021, MNRAS, 501, 4812
Flynn C., Holmberg J., Portinari L., Fuchs B., Jahreiss H., 2006, MNRAS, 372, 1149
Fomalont E. B. et al., 2015, ApJ Lett., 808, 1
Fukui Y. et al., 1999, PASJ, 51, 745
Furlong M. et al., 2015, MNRAS, 450, 4486
Gallazzi A., Charlot S., Brinchmann J., White S. D. M., Tremonti C. A., 2005, MNRAS, 362, 41
Gallazzi A., Brinchmann J., Charlot S., White S. D., 2008, MNRAS, 383, 1439
Gandhi P. J., Wetzel A., Hopkins P. F., Shappee B. J., Wheeler C., Faucher-Giguère C.-A., 2022, MNRAS, 516, 1941
Gardner J. P. et al., 2006, Space Sci. Rev., 123, 96
Garrison-Kimmel S. et al., 2017, MNRAS, 471, 1709
Garrison-Kimmel S. et al., 2019, MNRAS, 487, 1380
Geha M., Blanton M. R., Yan R., Tinker J. L., 2012, ApJ, 757, 85
Genel S. et al., 2014, MNRAS, 445, 175
Genel S. et al., 2018, MNRAS, 474, 3976
Gensior J., Feldmann R., Mayer L., Wetzel A., Hopkins P. F., Faucher-Giguère C.-A., 2022, MNRAS, 518, L63
Genzel R. et al., 2010, MNRAS, 407, 2091
Gill S. P. D., Knebe A., Gibson B. K., 2004, MNRAS, 351, 399
Gilmozzi R., Spyromilio J., 2007, The Messenger, 127, 11
Girichidis P. et al., 2016, ApJ, 816, L19
Gnedin N. Y., Kravtsov A. V., 2011, ApJ, 728, 88
Gnedin N. Y., Tassis K., Kravtsov A. V., 2009, ApJ, 697, 55
Governato F., Willman B., Mayer L., Brooks A., Stinson G., Valenzuela O., Wadsley J., Quinn T., 2007, MNRAS, 374, 1479
Governato F. et al., 2010, Nature, 463, 203
Grand R. J. J. et al., 2017, MNRAS, 467, stx071
Grand R. J. et al., 2021, MNRAS, 507, 4953
Guedes J., Callegari S., Madau P., Mayer L., 2011, ApJ, 742, 76
Gurvich A. B. et al., 2020, MNRAS, 498, 3664
Guszejnov D., Grudíc M. Y., Offner S. S., Boylan-Kolchin M., Faucher-Gigère C. A., Wetzel A., Benincasa S. M., Loebman S., 2020, MNRAS, 492, 488
Hafen Z. et al., 2017, MNRAS, 469, 2292
Hafen Z. et al., 2019, MNRAS, 488, 1248
Hafen Z. et al., 2022, MNRAS, 514, 5056
Hahn O., Abel T., 2011, MNRAS, 415, 2101
Hearin A. P., Watson D. F., 2013, MNRAS, 435, 1313
Hennebelle P., Inutsuka S. I., 2019, Front. Astron. Space Sci., 6
Herrmann K. A., Hunter D. A., Zhang H.-X., Elmegreen B. G., 2016, AJ, 152, 177
Heyer M., Dame T., 2015, ARA&A, 53, 583
Hilz M., Naab T., Ostriker J. P., 2013, MNRAS, 429, 2924
Hopkins P. F., 2015, MNRAS, 450, 53
Hopkins P. F., Grudić M. Y., 2019, MNRAS, 483, 4187
Hopkins P. F., Hernquist L., Cox T. J., Di Matteo T., Robertson B., Springel V., 2006, ApJS, 163, 1
Hopkins P. F., Quataert E., Murray N., 2011, MNRAS, 417, 950
Hopkins P. F., Quataert E., Murray N., 2012, MNRAS, 421, 3488
Hopkins P. F., Keres D., Onorbe J., Faucher-Giguere C.-A., Quataert E., Murray N., Bullock J. S., 2014, MNRAS, 445, 581
Hopkins P. F. et al., 2018, MNRAS, 480, 800
Hopkins P. F. et al., 2020, MNRAS, 492, 3465
Hopkins P. F. et al., 2022, MMRAS, 519, 3154
Hopkins A. M., Beacom J. F., 2006, ApJ, 651, 142
Hoppmann L., Staveley-Smith L., Freudling W., Zwaan M. A., Minchin R. F., Calabretta M. R., 2015, MNRAS, 452, 3726
Hu W. et al., 2019, MNRAS, 489, 1619
Hunter D. A. et al., 2012, AJ, 144, 134
Hunter J. D., 2007, Comput. Sci. Eng., 9, 90
Iwamoto K., Brachwitz F., Nomoto K., Kishimoto N., Umeda H., Hix W. R., Thielemann F., 1999, ApJS, 125, 439
Johnson B. D., Leja J., Conroy C., Speagle J. S., 2021, ApJS, 254, 22
Jones M. G., Haynes M. P., Giovanelli R., Moorman C., 2018, MNRAS, 477, 2
Juneau S. et al., 2005, ApJ, 619, L135
Kaastra J. et al., 2013, preprint (arXiv:1306.2324)
Kalberla P. M. W., Dedes L., 2008, A&A, 487, 951
Katz N., Weinberg D. H., Hernquist L., 1996, ApJS, 105, 19
Kaviraj S. et al., 2017, MNRAS, 467, 4739
Kereš D., Katz N., Weinberg D. H., Dave R., 2005, MNRAS, 363, 2
Kewley L. J., Dopita M. a., 2002, ApJS, 142, 35
Kewley L. J., Ellison S. L., 2008, ApJ, 681, 1183
Khandai N., Di Matteo T., Croft R., Wilkins S., Feng Y., Tucker E., DeGraf C., Liu M.-s., 2015, MNRAS, 450, 1349
Kim S., Staveley-Smith L., Sault R. J., Dopita M. A., Freeman K. C., Kesteven M. J., McConnell D., 1999, Symp. IAU, 190, 101
Kim C.-G., Ostriker E. C., 2017, ApJ, 846, 133
Kim C.-G. et al., 2020, ApJ, 900, 61
Kirby E. N., Cohen J. G., Guhathakurta P., Cheng L., Bullock J. S., Gallazzi A., 2013, ApJ, 779, 102
Klypin A. A., Shandarin S. F., 1983, MNRAS, 204, 891
Knollmann S. R., Knebe A., 2009, ApJS, 182, 608
Köppen J., Weidner C., Kroupa P., 2007, MNRAS, 375, 673
Koudmani S., Henden N. A., Sijacki D., 2021, MNRAS, 503, 3568
Kravtsov A. V., Berlind A. A., Wechsler R. H., Klypin A. A., Gottlober S., Allgood B., Primack J. R., 2004, ApJ, 609, 35
Kriek M. et al., 2006, ApJ, 649, L71
Kroupa P., 2001, MNRAS, 322, 231
Kruijssen J. M., Pfeffer J. L., Crain R. A., Bastian N., 2019, MNRAS, 486, 3134
Krumholz M. R., Dekel A., 2012, ApJ, 753, 16
Krumholz M. R., Gnedin N. Y., 2011, ApJ, 729, 36
Krumholz M. R., McKee C. F., Tumlinson J., 2008, ApJ, 689, 865
Krumholz M. R., McKee C. F., Tumlinson J., 2009, ApJ, 693, 216
Lagos C. D. P. et al., 2015, MNRAS, 452, 3815
Lanzetta K. M., McMahon R. G., Wolfe A. M., Turnshek D. A., Hazard C., Lu L., 1991, ApJS, 77, 1
Larson R. B., 1972, Nature Phys. Sci., 236, 7
Lazar A., Bullock J. S., Boylan-Kolchin M., Feldmann R., Catmabacak O., Moustakas L., 2021, MNRAS, 502, 6064
Lee H., Skillman E. D., Cannon J. M., Jackson D. C., Gehrz R. D., Polomski E. F., Woodward C. E., 2006, ApJ, 647, 970
Leitherer C. et al., 1999, ApJS, 123, 3
Leja J., Johnson B. D., Conroy C., van Dokkum P. G., Byler N., 2017, ApJ, 837, 170
Leja J., Speagle J. S., Johnson B. D., Conroy C., van Dokkum P., Franx M., 2020, ApJ, 893, 111
Leja J. et al., 2022, ApJ, 936, 165
Leroy A. K. et al., 2011, ApJ, 737, 12
Leroy A. K. et al., 2021a, ApJS, 257, 43
Leroy A. K. et al., 2021b, ApJS, 257, 43
Leslie S. K. et al., 2020, ApJ, 899, 58
Lewis A., Challinor A., Lasenby A., 2000, ApJ, 538, 473
Li M., Bryan G. L., Ostriker J. P., 2017, ApJ, 841, 101
Liang L., Feldmann R., Faucher-Giguère C.-A., Kereš D., Hopkins P. F., Hayward C. C., Quataert E., Scoville N. Z., 2018, MNRAS, 478, L83
Liang L. et al., 2019, MNRAS, 489, 1397
Lilly S. J., Le Fèvre O., Hammer F., Crampton D., 1996, ApJ, 460, L1
Lilly S. J., Carollo C. M., Pipino A., Renzini A., Peng Y., 2013, ApJ, 772, 119
Lin L. et al., 2020, ApJ, 903, 145
Ma X., Hopkins P. F., Faucher-Giguère C.-A., Zolman N., Muratov A. L., Kereš D., Quataert E., 2016, MNRAS, 456, 2140
Ma X. et al., 2018, MNRAS, 478, 1694
Ma X. et al., 2019, MNRAS, 487, 1844
Mackereth J. T., Bovy J., 2020, MNRAS, 492, 3631
Madau P., Dickinson M., 2014, ARA&A, 52, 415
Madau P., Ferguson H. C., Dickinson M. E., Giavalisco M., Steidel C. C., Fruchter A., 1996, MNRAS, 283, 1388
Maller A. H., Bullock J. S., 2004, MNRAS, 355, 694
Mannucci F., Della Valle M., Panagia N., 2006, MNRAS, 370, 773
Mannucci F., Cresci G., Maiolino R., Marconi A., Gnerucci A., 2010, MNRAS, 408, 2115

Downloaded from https://academic.oup.com/mnras/article/522/3/3831/7140530 by Northwestern University School of Law user on 03 July 2023

Marinacci F., Pakmor R., Springel V., 2014, MNRAS, 437, 1750
Marinacci F., Sales L. V., Vogelsberger M., Torrey P., Springel V., 2019, MNRAS, 489, 4233
Marsaglia G., 2003, J. Stat. Softw., 8, 1
Martizzi D., Teyssier R., Moore B., 2012, MNRAS, 420, 2859
Masters K. L. et al., 2019, MNRAS, 488, 3396
Matthee J., Schaye J., Crain R. A., Schaller M., Bower R., Theuns T., 2017, MNRAS, 465, 2381
Mayer L., Governato F., Kaufmann T., 2008, Adv. Sci. Lett., 1, 7
McGaugh S. S., Schombert J. M., de Blok W. J. G., Zagursky M. J., 2010, ApJ, 708, L14
McKee C. F., Krumholz M. R., 2010, ApJ, 709, 308
McMillan P. J., 2017, MNRAS, 465, 76
McQuinn M., Peng Oh S., Faucher-Giguère C.-A., 2011, ApJ, 743, 82
Menon H., Wesolowski L., Zheng G., Jetley P., Kale L., Quinn T., Governato F., 2015, Comput. Astrophys. Cosmol., 2, 1
Miller M. J., Bregman J. N., 2015, ApJ, 800, 14
Moreno J. et al., 2022, Nature Astron., 6, 496
Moster B. P., Naab T., White S. D. M., 2018, MNRAS, 477, 1822
Moustakas J. et al., 2013, ApJ, 767, 50
Mowla L. A. et al., 2019, ApJ, 880, 57
Munshi F., Brooks A. M., Christensen C., Applebaum E., Holley-Bockelmann K., Quinn T. R., Wadsley J., 2019, ApJ, 874, 40
Muratov A. L., Kereš D., Faucher-Giguère C.-A., Hopkins P. F., Quataert E., Murray N., 2015, MNRAS, 454, 2691
Muratov A. L. et al., 2017, MNRAS, 468, 4170
Murray S. G., Power C., Robotham A. S. G., 2013, MNRAS, 434, L61
Muzzin A. et al., 2013, ApJ, 777, 18
Naab T., Ostriker J. P., 2017, ARA&A, 55, 59
Naab T., Johansson P. H., Ostriker J. P., 2009, ApJ, 699, L178
Narayanan D., Bothwell M., Davé R., 2012, MNRAS, 426, 1178
Nedkova K. V. et al., 2021, MNRAS, 506, 928
Nelson D. et al., 2019a, Comput. Astrophys. Cosmol., 6, 2
Nelson D. et al., 2019b, MNRAS, 490, 3234
Nidever D. L., Majewski S. R., Burton W. B., Nigra L., 2010, ApJ, 723, 1618
Noeske K. G. et al., 2007, ApJ, 660, L43
Nomoto K., Tominaga N., Umeda H., Kobayashi C., Maeda K., 2006, Nucl. Phys. A, 777, 424
Noterdaeme P., Petitjean P., Ledoux C., Srianand R., 2009, A&A, 505, 1087
Noterdaeme P. et al., 2012a, A&A, 540, 1
Noterdaeme P. et al., 2012b, A&A, 547, L1
Nuñez-Castiñeyra A., Nezri E., Devriendt J., Teyssier R., 2021, MNRAS, 501, 62
O'Meara J. M., Prochaska J. X., Burles S., Prochter G., Bernstein R. A., Burgess K. M., 2007, ApJ, 656, 666
Oser L., Ostriker J. P., Naab T., Johansson P. H., Burkert A., 2010, ApJ, 725, 2312
Pagel B. E. J., Edmunds M. G., Blackwell D. E., Chun M. S., Smith G., 1979, MNRAS, 189, 95
Pandya V. et al., 2020, ApJ, 905, 4
Pandya V. et al., 2021, MNRAS, 508, 2979
Peebles P. J. E., 1980, The Large-Scale Structure of the Universe. Princeton Univ. Press, Princeton, NJ
Peimbert A., Peimbert M., 2010, ApJ, 724, 791
Peng Y.-j. et al., 2010, ApJ, 721, 193
Peng Y., Lilly S. J., Renzini A., Carollo M., 2012, ApJ, 757, 4
Peng Y., Maiolino R., Cochrane R., 2015, Nature, 521, 192
Peroux C., Howk J. C., 2020, ARA&A, 58, 363
Péroux C., McMahon R. G., Storrie-Lombardi L. J., Irwin M. J., 2003, MNRAS, 346, 1103
Peroux C., Dessauges-Zavadsky M., D'Odorico S., Sun Kim T., McMahon R. G., 2005, MNRAS, 363, 479
Pillepich A. et al., 2014, MNRAS, 444, 237
Pillepich A. et al., 2018a, MNRAS, 473, 4077
Pillepich A. et al., 2018b, MNRAS, 475, 648
Planck Collaboration, 2015, A&A, 594, A13
Popping G. et al., 2019, ApJ, 882, 137
Prochaska J. X., Wolfe A. M., 2009, ApJ, 696, 1543
Prochaska J. X., Herbert-Fort S., Wolfe A. M., 2005, ApJ, 635, 123
Purcell C. W., Bullock J. S., Zentner A. R., 2007, ApJ, 666, 20
Rahmati A., Schaye J., Pawlik A. H., Raičevic M., 2013, MNRAS, 431, 2261
Rahmati A., Schaye J., Bower R. G., Crain R. A., Furlong M., Schaller M., Theuns T., 2015, MNRAS, 452, 2034
Rao S. M., Turnshek D. A., Sardane G. M., Monier E. M., 2017, MNRAS, 471, 3428
Rauch M., 1998, ARA&A, 36, 267
Reddick R. M., Wechsler R. H., Tinker J. L., Behroozi P. S., 2013, ApJ, 771, 30
Rémy-Ruyer A. et al., 2014, A&A, 563, A31
Revaz Y., Jablonka P., 2018, A&A, 616, 1
Rhee J., Zwaan M. A., Briggs F. H., Chengalur J. N., Lah P., Oosterloo T., van der Hulst T., 2013, MNRAS, 435, 2693
Rhee J., Lah P., Chengalur J. N., Briggs F. H., Colless M., 2016, MNRAS, 460, 2675
Rhee J., Lah P., Briggs F. H., Chengalur J. N., Colless M., Willner S. P., Ashby M. L. N., Le Fèvre O., 2018, MNRAS, 473, 1879
Riechers D. A. et al., 2019, ApJ, 872, 7
Rodriguez-Gomez V. et al., 2016, MNRAS, 458, 2371
Rohr E. et al., 2022, MNRAS, 510, 3967
Rudie G. C., Steidel C. C., Shapley A. E., Pettini M., 2013, ApJ, 769, 146
Saintonge A. et al., 2011, MNRAS, 415, 32
Saintonge A. et al., 2013, ApJ, 778, 2
Saintonge A. et al., 2017, ApJS, 233, 22
Salem M., Bryan G. L., 2014, MNRAS, 437, 3312
Salem M., Besla G., Bryan G., Putman M., van der Marel R. P., Tonnesen S., 2015, ApJ, 815, 77
Salim S. et al., 2007, ApJS, 173, 267
Salpeter E. E., 1955, ApJ, 121, 161
Samuel J. et al., 2020, MNRAS, 491, 1471
Samuel J., Wetzel A., Santistevan I., Tollerud E., Moreno J., Boylan-Kolchin M., Bailin J., Pardasani B., 2022, MNRAS, 514, 5276
Sánchez Almeida J., Elmegreen B. G., Muñoz-Tuñón C., Elmegreen D. M., 2014, A&AR, 22, 71
Sánchez-Ramírez R. et al., 2016, MNRAS, 456, 4488
Sánchez S. F. et al., 2019, MNRAS, 484, 3042
Sanders R. L. et al., 2021, ApJ, 914, 19
Sawala T. et al., 2016, MNRAS, 457, 1931
Scannapieco C. et al., 2012, MNRAS, 423, 1726
Schaller M. et al., 2015, MNRAS, 451, 1247
Schaye J. et al., 2015, MNRAS, 446, 521
Schreiber C. et al., 2015, A&A, 575, A74
Scoville N. et al., 2014, ApJ, 783, 84
Semenov V. A., Kravtsov A. V., Gnedin N. Y., 2016, ApJ, 826, 200
Shen S., Wadsley J., Stinson G., 2010, MNRAS, 407, 1581
Simha V., Weinberg D. H., Davé R., Gnedin O. Y., Katz N., Kereš D., 2009, MNRAS, 399, 650
Simionescu A. et al., 2021, Exp. Astron., 51, 1043
Solomon P. M., Rivolo A. R., Barrett J., Yahil A., 1987, ApJ, 319, 730
Somerville R. S., Davé R., 2015, ARA&A, 53, 51
Somerville R. S., Gilmore R. C., Primack J. R., Domínguez A., 2012, MNRAS, 423, 1992
Somerville R. S., Popping G., Trager S. C., 2015, MNRAS, 453, 4337
Song M. et al., 2016, ApJ, 825, 5
Sparre M., Hayward C. C., Feldmann R., Faucher-Giguère C.-A., Muratov A. L., Kereš D., Hopkins P. F., 2017, MNRAS, 466, 88
Speagle J. S., Steinhardt C. L., Capak P. L., Silverman J. D., 2014, ApJS, 214, 15
Springel V., 2005, MNRAS, 364, 1105
Springel V., 2010, MNRAS, 401, 791
Springel V., Di Matteo T., Hernquist L., 2004, MNRAS, 361, 776
Springel V., Di Matteo T., Hernquist L., 2005, MNRAS, 361, 776
Springel V. et al., 2008, MNRAS, 391, 1685
Stanimirovic S., Staveley-Smith L., Dickey J. M., Sault R. J., Snowden S. L., 1999, MNRAS, 302, 417

Downloaded from https://academic.oup.com/mnras/article/522/3/3831/7140530 by Northwestern University School of Law user on 03 July 2023

Stern J., Fielding D., Faucher-Giguère C.-A., Quataert E., 2020, MNRAS, 492, 6042
Stern J. et al., 2021a, MNRAS, 507, 2869
Stern J. et al., 2021b, ApJ, 911, 88
Stinson G., Seth A., Katz N., Wadsley J., Governato F., Quinn T., 2006, MNRAS, 1090, 1074
Storrie-Lombardi L. J., Wolfe A. M., 2000, ApJ, 543, 552
Straatman C. M. S. et al., 2016, ApJ, 830, 51
Su K.-Y., Hopkins P. F., Hayward C. C., Faucher-Giguère C.-A., Kereš D., Ma X., Robles V. H., 2017, MNRAS, 471, 144
Su K.-Y. et al., 2020, MNRAS, 491, 1190
Su K. Y. et al., 2021, MNRAS, 507, 175
Suresh J., Rubin K. H., Kannan R., Werk J. K., Hernquist L., Vogelsberger M., 2017, MNRAS, 465, 2966
Szakacs R., Péroux C., Zwaan M. A., Nelson D., Schinnerer E., Lahén N., Weng S., Fresco A. Y., 2022, MNRAS, 16, 1
Tacconi L. J., Genzel R., Sternberg A., 2020, ARA&A, 58, 157
Teyssier R., 2002, A&A, 385, 337
Thorne J. E. et al., 2020, MNRAS, 505, 540
Tomczak A. R. et al., 2014, ApJ, 783, 85
Trapp C. W. et al., 2022, MNRAS, 509, 4149
Tremmel M., Karcher M., Governato F., Volonteri M., Quinn T. R., Pontzen A., Anderson L., Bellovary J., 2017, MNRAS, 470, 1121
Tremmel M. et al., 2019, MNRAS, 483, 3336
Tremonti C. A. et al., 2004, ApJ, 613, 898
Tumlinson J., Peeples M. S., Werk J. K., 2017, ARA&A, 55, 389
Tytler D., 1987, ApJ, 321, 49
Vale A., Ostriker J. P., 2004, MNRAS, 353, 189
van de Voort F., Quataert E., Hopkins P. F., Faucher-Giguère C.-A., Feldmann R., Kereš D., Chan T. K., Hafen Z., 2016, MNRAS, 463, 4533
Verner D. A., Ferland G. J., 1996, ApJS, 103, 467
Vigna S., 2016, ACM Trans. Math. Softw., 42, 1
Vijayan A., Li M., 2021, MNRAS, 510, 568
Villaescusa-Navarro F. et al., 2018, Astrophys. J., 866, 135
Vogelsberger M., Genel S., Sijacki D., Torrey P., Springel V., Hernquist L., 2013, MNRAS, 436, 3031
Vogelsberger M. et al., 2014, MNRAS, 444, 1518
Vogelsberger M., Marinacci F., Torrey P., Puchwein E., 2020, Nature Rev. Phys., 2, 42
Volonteri M., Dubois Y., Pichon C., Devriendt J., 2016, MNRAS, 460, 2979
Walter F., Brinks E., de Blok W. J. G., Bigiel F., Kennicutt R. C., Thornley M. D., Leroy A., 2008, AJ, 136, 2563
Walter F. et al., 2020, ApJ, 902, 111
Wang L., Dutton A. A., Stinson G. S., Macciò A. V., Penzo C., Kang X., Keller B. W., Wadsley J., 2015, MNRAS, 454, 83
Wechsler R. H., Tinker J. L., 2018, ARA&A, 56, 435
Weigel A. K., Schawinski K., Bruderer C., 2016, MNRAS, 459, 2150
Wellons S. et al., 2023, MNRAS, 520, 5394
Werk J. K. et al., 2014, ApJ, 792, 8
Wetzel A. R., Tinker J. L., Conroy C., van den Bosch F. C., 2013, MNRAS, 432, 336
Wetzel A. R., Hopkins P. F., Kim J.-h., Faucher-Giguère C.-A., Kereš D., Quataert E., 2016, ApJ, 827, L23
Wheeler C. et al., 2019, MNRAS, 490, 4447
White S. D. M., Rees M. J., 1978, MNRAS, 183, 341
Wiersma R. P. C., Schaye J., Smith B. D., 2009a, MNRAS, 393, 99
Wiersma R. P., Schaye J., Theuns T., Dalla Vecchia C., Tornatore L., 2009b, MNRAS, 399, 574
Wolfe A. M., Turnshek D. A., Smith H. E., Cohen R. D., 1986, ApJS, 61, 249
Wolfe A. M., Gawiser E., Prochaska J. X., 2005, ARA&A, 43, 861
Woosley S. E., Weaver T. A., 1995, ApJS, 101, 181
Zafar T., Péroux C., Popping A., Milliard B., Deharveng J. M., Frank S., 2013, A&A, 556, 1
Zu Y., Mandelbaum R., 2015, MNRAS, 454, 1161
Zwaan M. A., Prochaska J. X., 2006, ApJ, 643, 675
Zwaan M. A., Van Der Hulst J. M., Briggs F. H., Verheijen M. A., Ryan-Weber E. V., 2005, MNRAS, 364, 1467

APPENDIX A: RE-WEIGHTING

We estimate the true (ensemble average) HMF for our adopted cosmology with the help of HMFcalc[9] (Murray, Power & Robotham 2013). Specifically, we select the 'Behroozi + 2013 (Tinker Extension to High-z)' fitting function (Behroozi et al. 2013) and a CAMB transfer function. We then calculate the HMF for the virial halo criterion (Bryan & Norman 1998) over a $\lg M_{\rm vir}/M_\odot = 7-15$ range in steps of $\Delta \lg M_{\rm vir} = 0.05$.

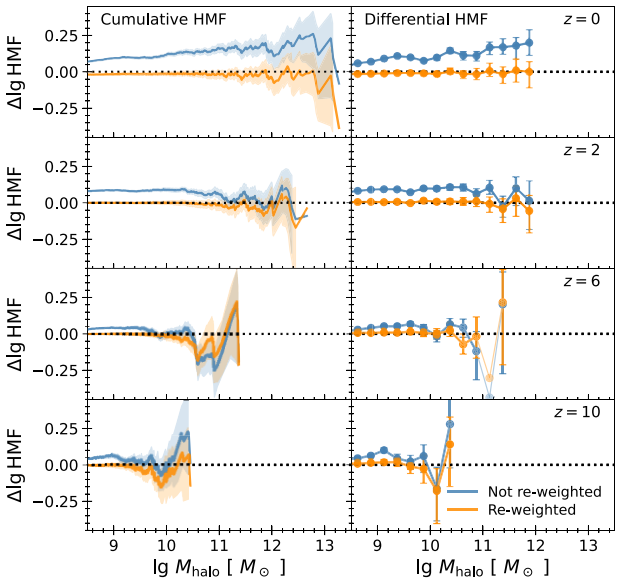

Figure A1. HMF in FIREbox relative to the reference HMF at $z = 0$–10 with and without re-weighting. Halo masses in the simulation are first converted to halo masses in a corresponding collisionless N-body simulation (shown on the x-axis) via halo AM. Subsequently, the empirical cumulative (left-hand panels) and differential (right-hand panels) HMF from the simulation are compared with the reference HMF (HMFcalc; Murray et al. 2013). Without re-weighting (blue lines), the HMF of FIREbox can overestimate the reference HMF by up to ∼0.2 dex. In contrast, the re-weighted cumulative and differential HMFs (orange lines and symbols) match their reference HMF nearly within statistical errors (shaded regions and error bars are the 16th to 84th percentiles calculated via bootstrapping).

The realized cumulative HMF in the simulation volume V can be estimated as the number of haloes above a certain mass $x = \lg M_{\rm h}$ divided by the simulation volume, i.e.

$$\hat{\Phi}(x) = \sum_{\{i:x_i \geq x\}} \frac{1}{V}. \tag{A1}$$

The idea of the re-weighting approach is to replace the equal weights of $1/V$ in the sum above with halo-dependent weights. Specifically, approximating the true cumulative HMF $\Phi(x) = \int_x^\infty \phi(x')\,{\rm d}x'$ with the following sum over the haloes in the simulation volume

$$\Phi(x) \approx \sum_{\{i:x_i \geq x\}} \phi(x_i)\,\Delta x_i\,, \tag{A2}$$

suggests that we can replace $1/V$ with weights $w_i = \phi(x_i)\,\Delta x_i$. Here, the line elements Δx_i represent the typical spacing in logarithmic halo mass between haloes with $\lg M_{\rm h}$ near x_i and $\phi(x)$ is the true differential HMF. We calculate the line elements Δx_i as d_i/N_i by

[9] https://hmf.icrar.org

Downloaded from https://academic.oup.com/mnras/article/522/3/3831/7140530 by Northwestern University School of Law user on 03 July 2023

counting the number of haloes (N_i) in a top hat kernel of diameter d_i and centred on x_i. The diameter is chosen such that the kernel includes a fixed number of haloes $N_i = 100$ subject to strict lower and upper bounds of $d_i \geq 0.05$ and $d_i \leq 0.5$. Before the weights are calculated, the masses of haloes in hydrodynamical simulations are converted to the masses expected for a corresponding collisionless N-body simulation by matching the cumulative abundances of haloes in FIREbox runs with and without baryonic physics.

The weights w_i exceed $1/V$ for underrepresented haloes in the simulation volume thus boosting their contribution and vice versa for overrepresented haloes. Once we assign weights w_i to all haloes, we can thus calculate re-weighted properties and mass functions in a straightforward manner. For instance, differential SMFs can be obtained via a weighted histogram, while cumulative SMFs sum all the weights of the host haloes of galaxies above a certain stellar mass.

In case re-weighting is used, only haloes containing more than 300 DM particles obtain updated weights. Haloes excluded from re-weighting obtain the standard weight $w_i = 1/V$. Sub-haloes are assigned the weights of their parent main haloes.

We show a test of the re-weighting approach in Fig. A1. Without re-weighting, the cumulative and differential HMFs in FIREbox can exceed the expectations from HMFcalc by up to ∼0.2 dex, especially at $z \leq 2$. After re-weighting, the HMFs typically match the reference HMFs close to statistical errors.

APPENDIX B: COMPARISON WITH FIRE-2 ZOOM-IN SIMULATIONS

The SMF in FIREbox shows a higher abundance of moderately low-mass galaxies ($M_{\rm star} \sim 10^9$–$10^{10}\ M_\odot$) than is seen in galaxy surveys. Here, we compare FIREbox to other FIRE-2 zoom-in simulations to explore whether this difference is caused by the numerical resolution or the different set-up of FIREbox as a cosmological volume simulation. Overall, we include 41 separate FIRE-2 zoom-in simulations that target haloes over a broad range of halo masses $M_{\rm halo} \sim 10^{11}$–$10^{13}\ M_\odot$ and are run to $z = 1$ or $z = 0$, see Table B1.

We derive cumulative SMFs for galaxies in zoom-in simulations in an approximate fashion via AM of the stellar masses of galaxies ($M_{\rm star}$) and the masses of their host haloes ($M_{\rm halo}$). Ignoring scatter, the cumulative SMF $\Phi_{\rm star}(\lg M_{\rm star})$ equals the cumulative HMF $\Phi(\lg M_{\rm halo})$, and we can thus plot $M_{\rm star}$ versus $\Phi_{\rm star}(\lg M_{\rm star})$ for each galaxy from a zoom-in simulations. Cumulative HMFs are obtained from HMFcalc as described in Appendix A.

The left-hand panel of Fig. B1 shows the SMF of central galaxies in FIREbox. We exclude satellite galaxies since the primary galaxies in zoom-in simulations are usually selected to be centrals or isolated galaxies. In each case, the abundances of the main (or isolated) haloes are re-weighted to match the expected HMF of all haloes (see Appendix A) to allow a more direct comparison with the SMF of zoom-in runs.

At high z, the SMF in FIREbox is in good agreement with the SMF predicted via AM from the zoom-in runs. At low z, however, FIREbox predicts a higher abundances for $M_{\rm star} \sim 10^9$–$10^{10}\ M_\odot$ galaxies compared both with the available FIRE-2 zooms (Fig. B1) and observations (Fig. 9). We now investigate the origin of difference in some detail.

First, we would like to test whether a selection bias towards more isolated galaxies in zoom-in simulations could be responsible. To this end, we plot in the right-hand panel of Fig. B1 the SMF of isolated galaxies in FIREbox. A galaxy is isolated if it does not lie within three times the virial radius of another main halo. A comparison with the left-hand panel of Fig. B1 and Fig. 9 reveals that the SMF in FIREbox in the stellar mass regime of interest does not strongly depend on the isolation criterion (all versus central versus isolated galaxies). Hence, differences in galaxy isolation do not appear to be responsible for the excess in moderately low-mass galaxies in FIREbox at low z.

Also, we can largely exclude a statistical effect related to the scatter in the SHMR relation. This scatter is empirically constrained to about 0.2 dex in massive haloes (see e.g. Reddick et al. 2013; Zu & Mandelbaum 2015), while numerical simulations (e.g. Schaye et al. 2015; Pillepich et al. 2018b; Feldmann et al. 2019), as well

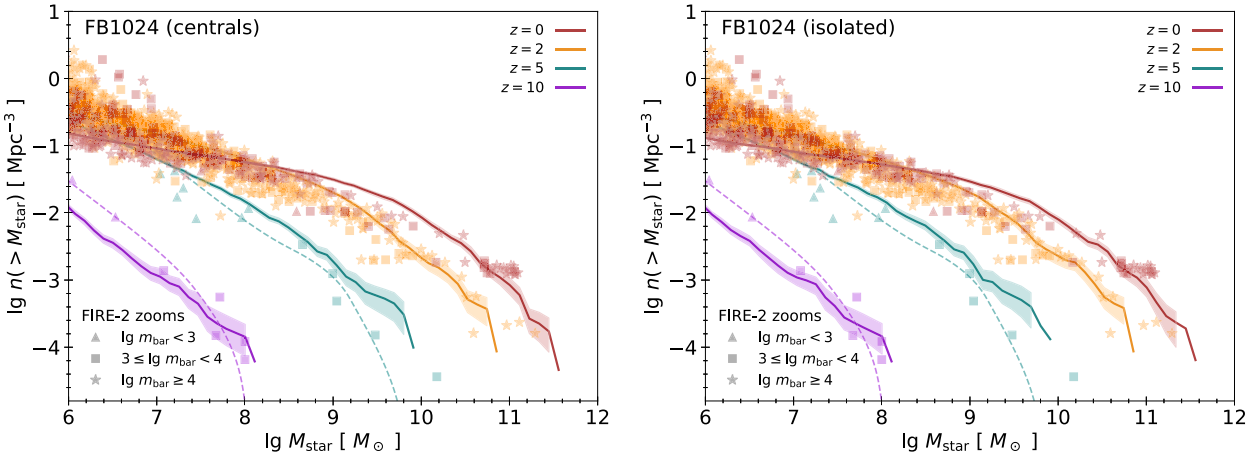

Figure B1. Comparison between FIRE-2 cosmological zoom-in simulations and FIREbox. Solid lines in the left-hand (right-hand) panel show the cumulative galaxy SMF of central (isolated) galaxies with $M_{\rm star} > 10^6\ M_\odot$ in FIREbox. A galaxy is isolated if it is the central galaxy of a main halo, and it does not lie within three times the virial radius of another main halo. The abundance of galaxies is re-weighted, see Appendix A. The various symbols correspond to SMF estimates for central galaxies in FIRE-2 cosmological zoom-in simulations at $z = 10$ and $z = 5$ (Ma et al. 2018), $z = 2$ (Anglés-Alcázar et al. 2017b), and $z = 0$ (Hopkins et al. 2018), see Table B1. Dashed lines are fits provided in Ma et al. (2018). For individual zoom-in simulations, the abundance of galaxies is derived from the expected abundance of their haloes. Circles, squares, and stars indicate zoom-in simulations with a baryonic mass resolution of $<10^3\ M_\odot$, $10^{3-4}\ M_\odot$, and $>10^4\ M_\odot$. FIREbox agrees with the results of previous zoom-in simulations for massive galaxies but appears to predict a larger abundance of intermediate mass galaxies ($M_{\rm star} \sim 10^9$–$10^{10}\ M_\odot$). This difference appears to be primarily related to the higher numerical resolution of zoom-in simulations of low-mass galaxies. Restricting the analysis to isolated galaxies, as opposed to central galaxies, does not significantly lower the abundance of intermediate mass galaxies.

Downloaded from https://academic.oup.com/mnras/article/522/3/3831/7140530 by Northwestern University School of Law user on 03 July 2023

Table B1. FIRE-2 zoom-in simulations used as a point of reference for FIREbox. The first three columns list the simulation identifier, baryonic mass resolution, and the final redshift reached by each simulation. The fourth column states the adopted cosmology of each run. All runs adopt a standard, flat ΛCDM cosmology with $h \sim 0.7$, $\Omega_m = 0.27 - 0.31$, and $\Omega_b \sim 0.0455$–0.048 broadly consistent with current observational constraints (Planck Collaboration 2015). Specifically, cosmology *a* corresponds to $h = 0.702$, $\Omega_m = 0.272$, $\Omega_b = 0.0455$, cosmology *b* to $h = 0.68$, $\Omega_m = 0.31$, $\Omega_b = 0.048$, and cosmology *c* to $h = 0.697$, $\Omega_m = 0.2821$, $\Omega_b = 0.0461$. The final column lists the work that first describes the respective simulation with A: Chan et al. (2018), B: Hopkins et al. (2018), C: Garrison-Kimmel et al. (2017), D: Anglés-Alcázar et al. (2017b), E: El-Badry et al. (2018), F: Garrison-Kimmel et al. (2019), G: Wetzel et al. (2016), and H: Samuel et al. (2020). The first 15 lines (the last 12 lines) list runs without (with) metal diffusion due to sub-grid turbulence (Hopkins et al. 2018).

Label	m_b ($10^3\ M_\odot$)	z_{final}	Cosmo	Source
		w/o Metal diffusion		
m11a	2.1	0	*a*	A
m11b	2.1	0	*a*	A
m11c	2.1	0	*a*	A
m11q	0.9, 7.1	0	*a*	B
m11v	7.1	0	*a*	B
m12b	57	0	*a*	B
m12c	57	0	*a*	B
m12f	7.1, 57	0	*a*	C
m12i	7.1, 57	0	*a*	B
m12m	7.1, 57	0	*a*	B
m12q	57	0	*a*	B
A1	33	1	*c*	D
A2	33	1	*c*	D
A4	33	1	*c*	D
A8	33	1	*c*	D
		w/ Metal diffusion		
m11d	7.1	0	*b*	E
m11e	7.1	0	*b*	E
m11h	7.1	0	*b*	E
m11i	7.1	0	*b*	E
m11q	7.1	0	*a*	B
m12b	7.1, 57	0	*a*	F
m12c	7.1, 57	0	*a*	F
m12f	7.1, 57, 450	0	*a*	C
m12i	7.1, 57, 450	0	*a*	G
m12m	7.1, 57, 450	0	*a*	B
m12r	7.1, 57	0	*b*	H
m12w	7.1, 57	0	*b*	H

as semi-analytic (e.g. Somerville et al. 2012) and empirical models (e.g. Hearin & Watson 2013), suggest that the scatter increases with decreasing halo mass to potentially ∼0.3 dex at $M_{halo} \sim 10^{11}\ M_\odot$ (Wechsler & Tinker 2018). However, Fig. B1 highlights that all FIRE-2 zoom-in simulations (out of a dozen) with $M_{star} \sim 10^9$–$10^{10}\ M_\odot$ at $z = 0$ have lower abundances, i.e. lower stellar masses for a given halo mass.

In Fig. B2, we show the SHMR for central galaxies in both FIREbox and in the FIRE-2 zoom-ins. The figure highlights that

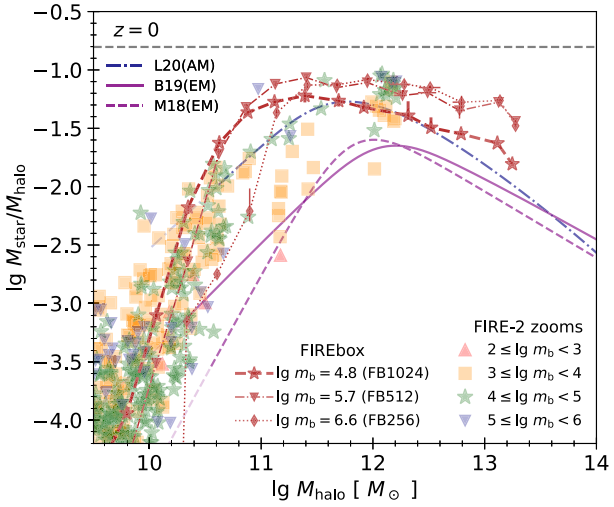

Figure B2. Ratio between the stellar mass of central galaxies and their parent haloes in FIREbox, its lower resolution re-runs, and in FIRE-2 zoom-in simulations at $z = 0$. The red dashed line (red dot–dashed and dotted lines) show the median stellar-mass-to-halo-mass ratio in bins of halo mass for FIREbox galaxies (for galaxies from the lower resolution re-runs), while all other symbols report the mass ratios of individual galaxies in FIRE-2 zoom-ins of different mass resolution (see legend). Stellar masses are measured within $R_g = 3\ R_{half}$, see Section 2.6. The figure includes estimates of the galaxy SHMR via AM (Leja et al. 2020, dot–dashed line) and EM (Moster et al. 2018; Behroozi et al. 2019, dashed and solid lines), see also Fig. 10. Various resolution trends are apparent. At the mass resolution of FIREbox ($m_b \sim 10^5\ M_\odot$), galaxy stellar mass depends only weakly on resolution in haloes of low ($<10^{10.5}\ M_\odot$) and high ($\gtrsim 10^{12}\ M_\odot$) mass. However, the stellar mass appears quite resolution-dependent for haloes of intermediate mass ($M_{halo} \sim 10^{11}\ M_\odot$). At low resolution ($m_b \gg 10^5\ M_\odot$), galaxy stellar masses are generally overestimated (underestimated) in haloes above (below) $\sim 10^{11}\ M_\odot$ relative to the primary FIREbox run.

stellar masses of galaxies in haloes of intermediate mass ($M_{halo} \sim 10^{11}\ M_\odot$) are noticeably resolution dependent, varying by an order of magnitude (with large scatter) when increasing the mass resolution by three orders of magnitude. In addition, it appears that central galaxies residing in such haloes are more massive (by ∼0.2 dex) in FIREbox compared with zoom-ins of a similar resolution. The latter result may indicate that the Lagrangian patches of the zoom-ins (or perhaps the box-size of FIREbox) are too small to adequately capture the cosmological environment at $z = 0$. Given the resolution dependence, we caution that our predictions for central galaxies residing in $M_{halo} \sim 10^{11}\ M_\odot$ haloes (and thus the SMF of galaxies with $M_{star} \sim 10^9 - 10^{10}\ M_\odot$) are uncertain. In contrast, stellar masses in low mass ($<10^{10.5}\ M_\odot$) and massive ($\sim 10^{12}\ M_\odot$) haloes appear close to converged.

This paper has been typeset from a TEX/LATEX file prepared by the author.

Downloaded from https://academic.oup.com/mnras/article/522/3/3831/7140530 by Northwestern University School of Law user on 03 July 2023

© The Author(s) 2023.
Published by Oxford University Press on behalf of Royal Astronomical Society. This is an Open Access article distributed under the terms of the Creative Commons Attribution License (https://creativecommons.org/licenses/by/4.0/), which permits unrestricted reuse, distribution, and reproduction in any medium, provided the original work is properly cited.